

7.0 ANALYSIS OF ESTIMATED GROUND MOTIONS

The simulated ground motions for the “rock” (~ 1 km/s surface shear-velocity) portion of Jackson Lake Dam (site JLDW) are larger than predicted by the empirical ground motion model developed for transtensional faulting environments by Spudich et al. (1999). The most unusual characteristic of the simulated “rock” ground motions is that they substantially exceed predicted soil accelerations from Spudich et al. (1999) at periods longer than 2 s. Somerville (2003) suggested two potential causes, near-fault rupture directivity and basin effects. One concern is that the simulation procedure, specifically the kinematic rupture model used in Section 6, may systematically overpredict near-fault ground motions, especially at long periods. While validation of any simulation procedure is not possible (Oreskes et al., 1994) a necessary credible condition is that a model reproduce past experience. Modeling of near-fault strong ground motions from the 1994 **M** 6.7 Northridge earthquake is used in Section 7.1 to evaluate the performance and credibility of the kinematic source model. The Northridge data represent the densest near-fault recordings of a dip-slip earthquake and are the best data available in the absence of a well-recorded normal-faulting earthquake. Ground motions are also synthesized in Section 7.4 using a simplified source model to provide an alternative approach to test the sensitivity of estimated ground motions to source model specification.

There are several possible tactics to evaluate the influence of the 3D basin velocity model on estimated ground motions. These could include performing ground motion simulations with alternative velocity models or completely removing the low-velocity-basin from the velocity model to provide a frame of reference for comparison with other strong motion data. Such approaches require considerable effort. There are recent recordings of larger magnitude (**M** > 4.5) earthquakes within 150 km of Jackson Lake Dam. These ground motion recordings have sufficient signal-to-noise (S/N) to evaluate ground motion characteristics for periods extending to 5-10 s, much longer periods than was possible with the high-frequency empirical Green’s functions in Section 6 and Appendix D (see Table 6-1). These larger magnitude earthquake recordings directly incorporate propagation effects associated with 3D low-velocity-basin structure. There are also two **M** ~ 3 earthquakes located in the vicinity of the northern Teton fault segment that provide empirical Green’s functions that allow simulation of ground motions to periods of ~ 3 s, although the long-period signal-to-noise is lower than the recordings of the **M** > 4.5 regional earthquakes.

The availability of broadband empirical Green's functions affords an opportunity to construct a second test of the kinematic source model and the ground motion simulation approach used in Section 6 by using an entirely different simulation method to estimate ground motions at Jackson Lake Dam using the previously tested approach of Frankel (1995). Frankel's (1995) approach is appealing because it uses very simple assumptions that only require specifying a small number of parameters, it produces source properties and ground motions consistent with known constraints (Andrews, 1980; Frankel, 1991), and it reproduced near-fault acceleration responses from the 1989 **M** 7.0 Loma Prieta earthquake (Frankel, 1995).

Before moving on to kinematic source model and ground motion simulation presentations, it is reasonable to ask: Is there a precedent for the large long-period ground motions estimated in Section 6 in strong motion observations? The 1979 **M** 6.5 Imperial Valley earthquake was recorded by an array of strong motion instruments located in the vicinity of the fault rupture. The Imperial fault and several near-fault strong motion stations are located in a sedimentary basin (Fuis et al., 1982). In the next section, the three strong motion records from this earthquake closest to the Imperial fault which contain large > 2 s acceleration responses are compared to predicted ground motions at Jackson Lake Dam.

7.1 Strong Ground Motions From the 1979 **M 6.5 Imperial Valley Earthquake**

On 15 October 1979 a **M** 6.5 earthquake occurred on the Imperial fault near the United States-Mexico border. The epicenter was located in northern Mexico and rupture proceeded north along the Imperial and Brawley faults producing particularly strong ground shaking in the El Centro array of accelerometers located along the northern portion of the Imperial fault (Figure 7-1). Since the Imperial fault is located in a sedimentary trough (Fuis et al., 1982) with a low-velocity basin structure similar to the low-velocity basin adjacent to the Teton fault, the strong motion recordings from sites close to the Imperial fault provide a qualitative indication of near-fault ground motion characteristics in a basin.

Fuis et al. (1982) showed that the Imperial fault is embedded in a 4-5 km deep low-velocity sedimentary basin with P-wave velocities and velocity gradients vary similar to velocity structure inferred for the low-velocity basin adjacent to the Teton fault in Section 4. Specifically, P-wave

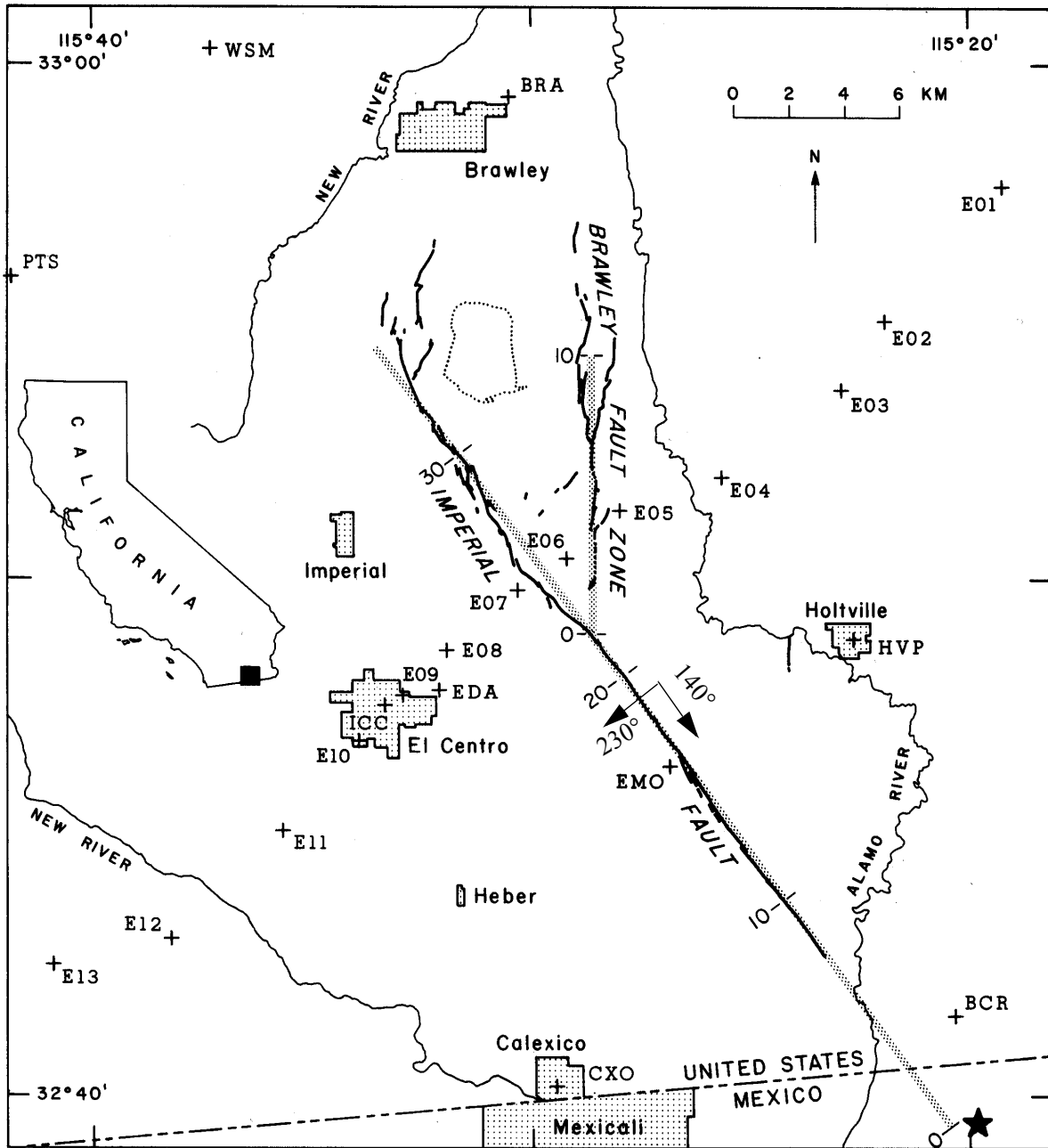


Figure 7-1: Map view of the Imperial Valley area from Archuleta (1984). Strong motion stations are labeled plus symbols. The portions of the Imperial and Brawley faults with measured surface offsets are shown by the dark line segments. Linear stippled regions show the idealized fault geometries used in Archuleta (1984) to model strong motions. The inset of California shows the approximate location of this map. Stations E06, E07, and EMO show strong long period responses as indicated in Figure 7-2 to 7-10. The labeled arrows indicate the orientation of the horizontal components in strike parallel (140°) and strike normal (230°) directions.

velocities in Imperial Valley near the surface along the refraction profile closest to the Imperial fault (SP-6 to SP-13) are ~ 2 km/s and are ~ 4.5 km/s at the bottom of the basin (Fuis et al., 1982). Basement P-wave velocities are > 5.5 km/s at both Jackson Lake and Imperial Valley. The biggest difference in the velocity structures are near the bottoms of the basins where P-wave velocities in the low-velocity-basin adjacent to the Teton fault are about 1 km/s slower at the bottom of the basin relative to Imperial Valley. In Imperial Valley the refraction data suggest a ~ 0.5 -km-thick transition zone below the sediments that increase P-wave velocities to ~ 5.5 km/s at the contact with the ~ 6 km/s basement. The refraction data and waveform modeling of velocity structure at Jackson Lake Dam suggest a very-large velocity discontinuity between the deepest sediments (~ 3.5 -4 km/s) and basement (~ 5.5 km/s) (see Figure 4-13). This results in a much stronger impedance contrast at the bottom of the low-velocity basin near the Teton fault relative to Imperial Valley. The larger impedance contrast at the base of the low-velocity basin beneath Jackson Lake Dam suggest that > 1 s period acceleration responses are likely to be larger than those observed from 1979 Imperial Valley earthquake due to stronger amplification and more efficient trapping of body and surface waves. Also, long-period responses at Jackson Lake Dam will likely have much longer durations. These differences in basin structure suggest that the strong motion records from Imperial Valley provide a rough lower bound on expected long-period accelerations at Jackson Lake Dam.

Stations E06, E07, and EMO are located within 2 km of the Imperial fault (Figure 7-1) and exhibit influences of directivity in the form of peak fault-normal velocities on the order of 100 cm/s. These sites are also located near the axis of the deepest portion of low-velocity sedimentary basin. While peak horizontal accelerations are not remarkable at station E06 (Figure 7-2), the peak vertical acceleration exceeds 1.6 g. The vertical peak accelerations's high-frequency content and arrival time suggest that it is an *S-P* conversion from inside the low-velocity basin. Strong *S-P* conversions are not a typical characteristic of Jackson Lake Dam JLDW ground motions. This suggests there may be stronger interval velocity discontinuities within the Imperial Valley low-velocity basin relative to the low-velocity basin at Jackson Lake Dam. Strong interval velocity discontinuities in trial velocity models of the Jackson Lake Dam low-velocity basin strongly reduced ground motion durations relative to smooth vertical-velocity-gradient models of basin structure, as discussed in Section 4. This may explain the relatively short-duration of station E06

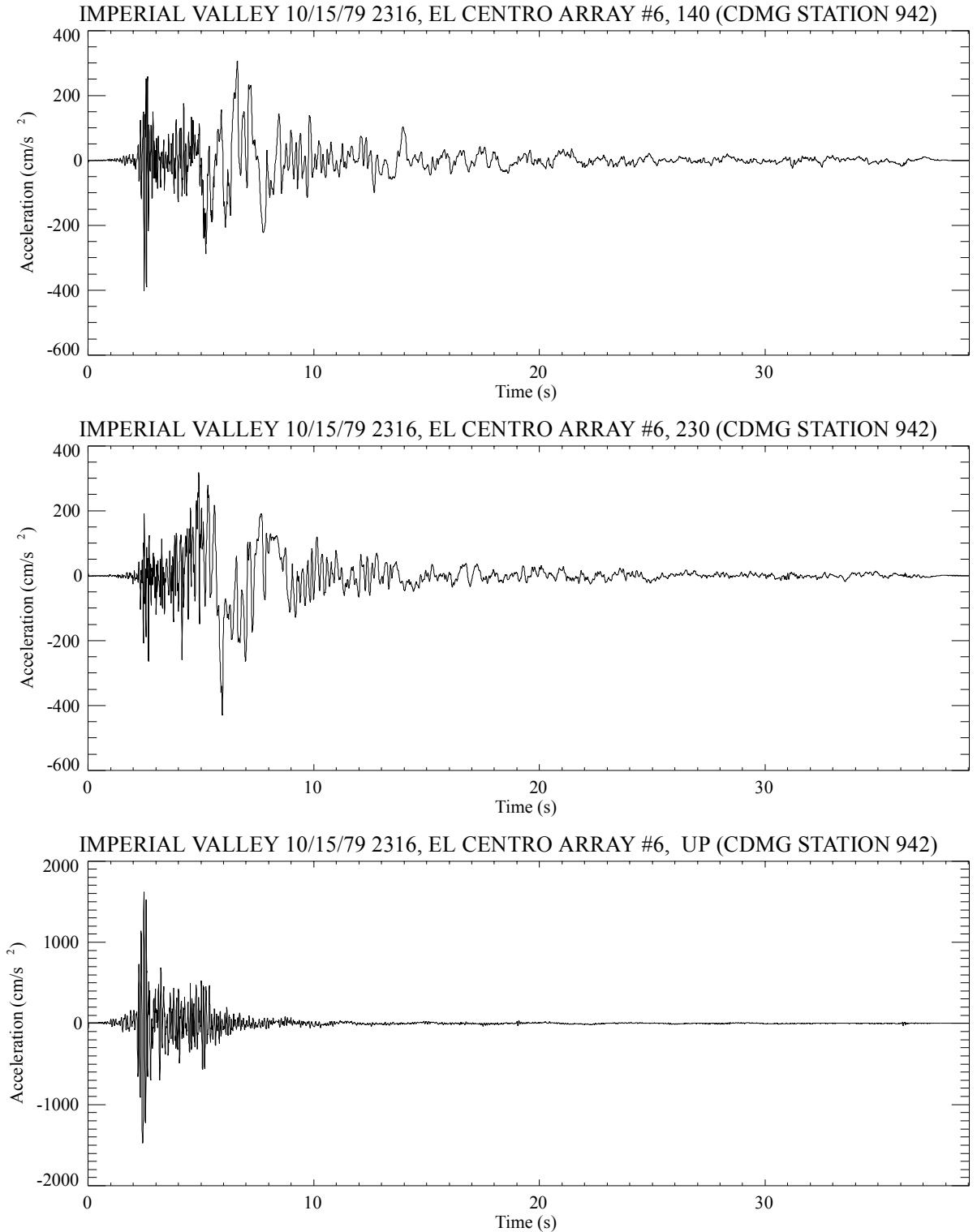


Figure 7-2: El Centro Array station E06 acceleration seismograms. Vertical is labeled UP. Horizontal components are labeled by their orientation in degrees east of north (e.g., 140° and 230°). See Figure 7-1 for station position relative to fault rupture.

motions (Figures 7-2 to 7-3) relative to ground motions observed at Jackson Lake Dam. Acceleration responses for periods larger than 2 s are remarkably large ($> \sim 0.4$ g) for the fault-normal component of station E06 (Figure 7-4) and are also quite large for periods of 2 s to 3 s for the fault-parallel component. In contrast, the vertical acceleration responses much lower at periods larger than 2 s.

Peak horizontal accelerations at Station E07 (Figure 7-5) are somewhat lower than for Station E06 (Figure 7-2), but broadband frequency content of the peak fault-normal accelerations and velocities (Figure 7-6) associated with rupture directivity are clearly evident in the 0-1 s period band in the spectral accelerations (Figure 7-7). However, strong accelerations > 0.4 g persist between periods of 2 s and 3 s and > 0.3 g for periods > 3 s on the fault-normal component (Figure 7-7). In contrast, the > 2 s period responses on the vertical and fault-parallel horizontal components are much lower (Figure 7-7).

Station EMO is located at about the halfway point along the rupture of the Imperial fault. Consequently, rupture directivity was not as strong as at station E06 and E07 and peak accelerations are lower (Figure 7-8) and peak velocities are also lower (< 100 cm/s) (Figure 7-9). However, fault-normal accelerations for periods between 2 s and 3 s are > 0.4 g (Figure 7-10), exceeding comparable accelerations at station E07 (Figure 7-7) even though rupture directivity is weaker at station EMO. While peak accelerations and velocities vary considerably between stations E06, E07, and EMO because of the variability of fault slip and station positions (Archuleta, 1984), the consistently elevated > 2 s acceleration fault-normal responses at all these stations is consistent with elevated long-period responses expected for low-velocity basins (Somerville et al., 2003).

Strike-slip faulting is likely to produce less complex ground motions in a basin because P - SV excitation is minimal compared to dip-slip faulting. Consequently, the Imperial Valley ground motions do not provide a direct analog for motions in the low-velocity basin adjacent to the Teton fault. However, the > 0.4 g > 2 s period acceleration responses observed in Imperial Valley indicate that the large (> 0.5 g) > 2 s period acceleration responses predicted for Jackson Lake Dam are not without precedent. Considering the more extreme impedance contrast between the

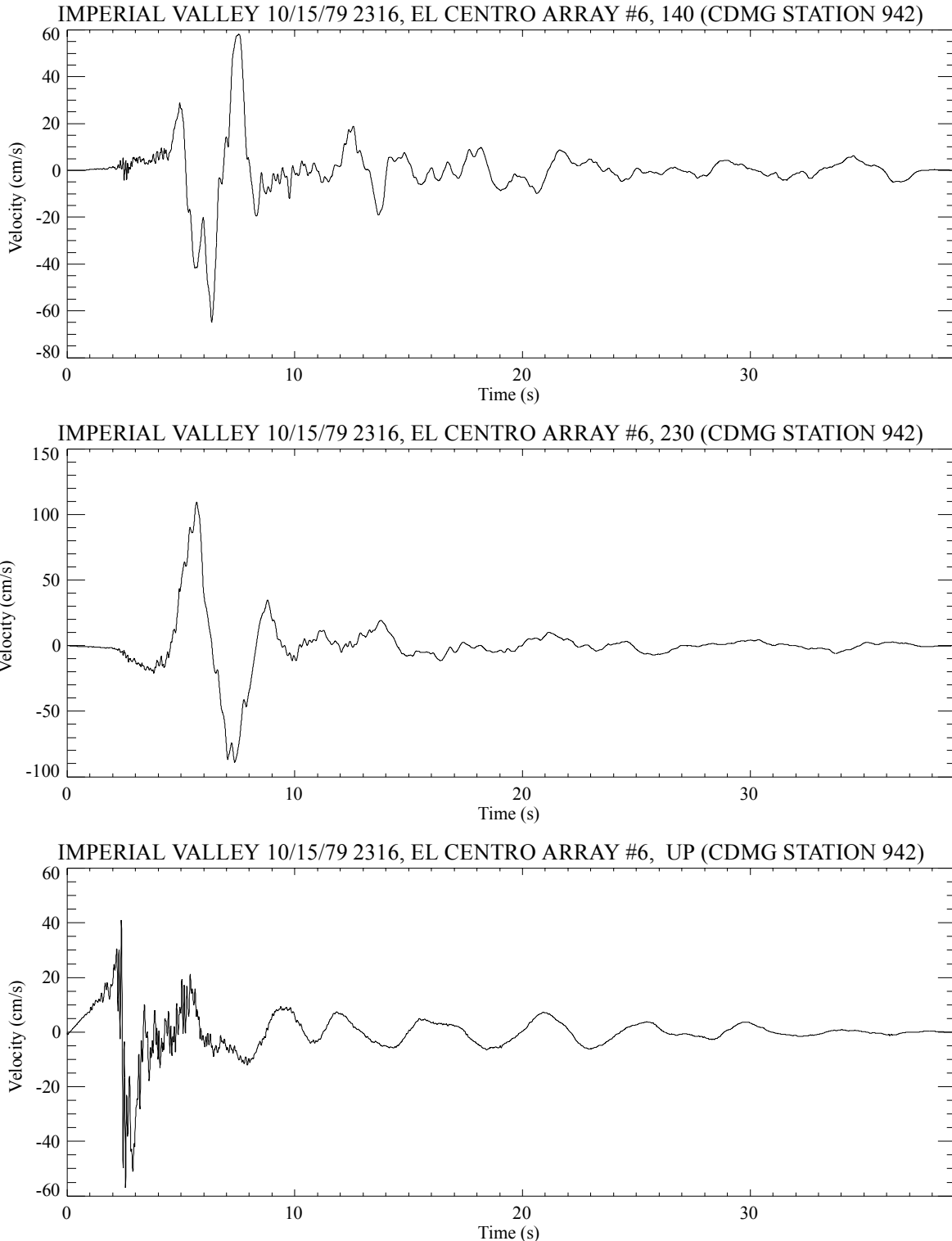


Figure 7-3: El Centro Array station E06 velocity seismograms. Vertical is labeled UP. Horizontal components are labeled by their orientation in degrees east of north (e.g., 140° and 230°). See Figure 7-1 for station position relative to fault rupture. The horizontal components are oriented in approximately strike-normal (230°) and strike-parallel (140°) directions relative to the strike of the Imperial fault.

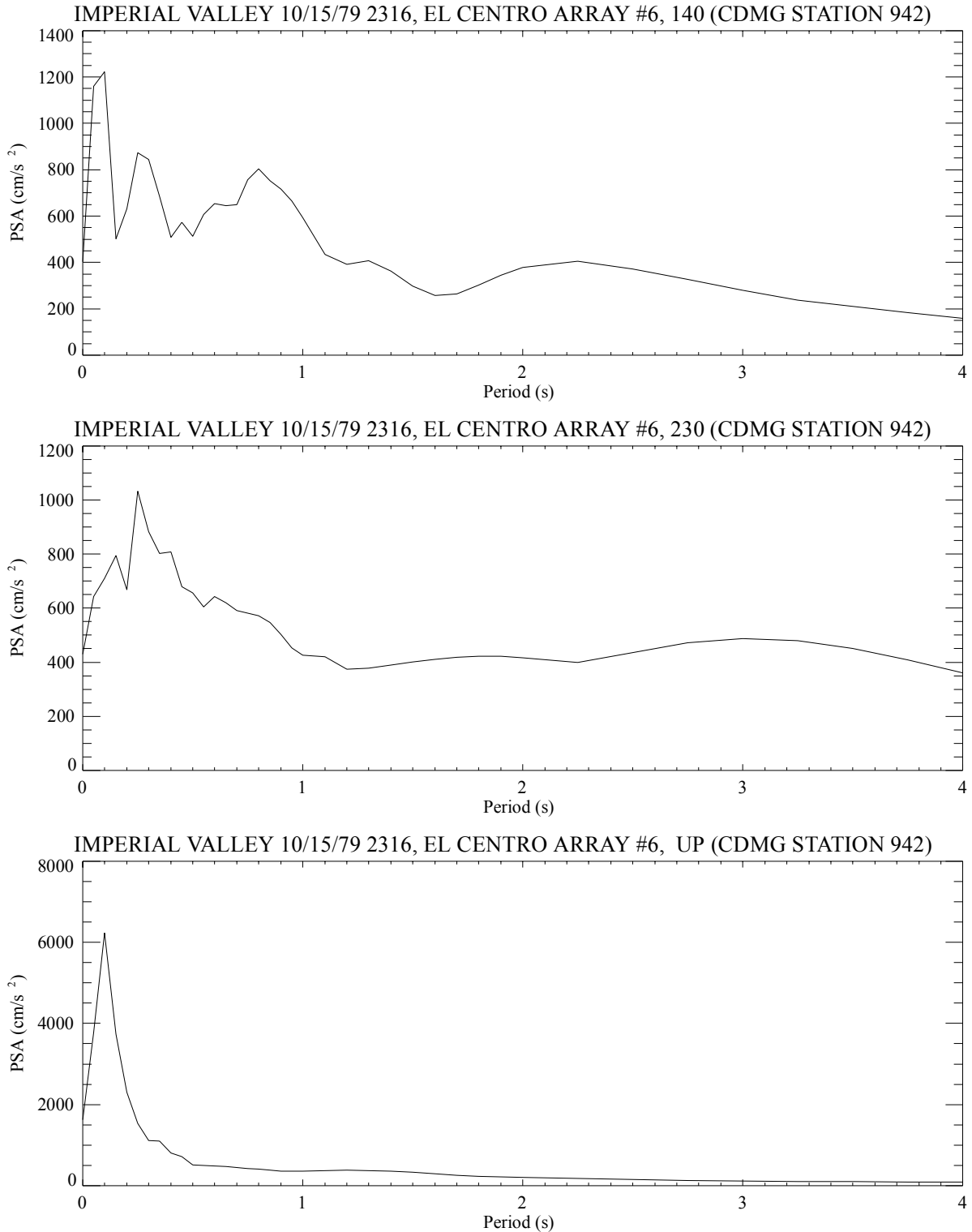


Figure 7-4: El Centro Array station E06 pseudo-acceleration response spectra. Vertical is labeled UP. Horizontal components are labeled by their orientation in degrees east of north (e.g., 140° and 230°). See Figure 7-1 for station position relative to fault rupture. The horizontal components are oriented in approximately strike-normal (230°) and strike-parallel (140°) directions relative to the strike of the Imperial fault.

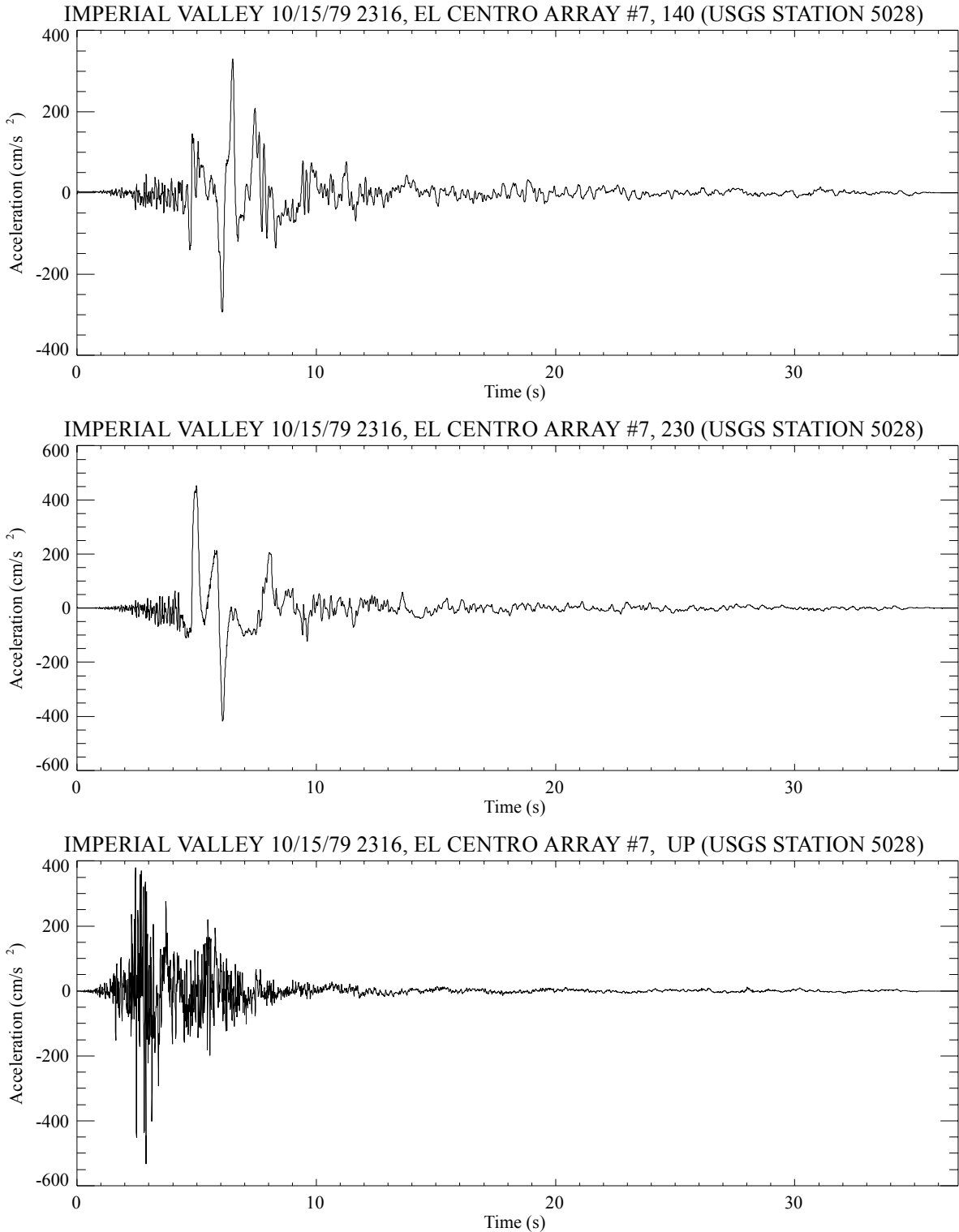


Figure 7-5: El Centro Array station E07 acceleration seismograms. Vertical is labeled UP. Horizontal components are labeled by their orientation in degrees east of north (e.g., 140° and 230°). See Figure 7-1 for station position relative to fault rupture. The horizontal components are oriented in approximately strike-normal (230°) and strike-parallel (140°) directions relative to the strike of the Imperial fault.

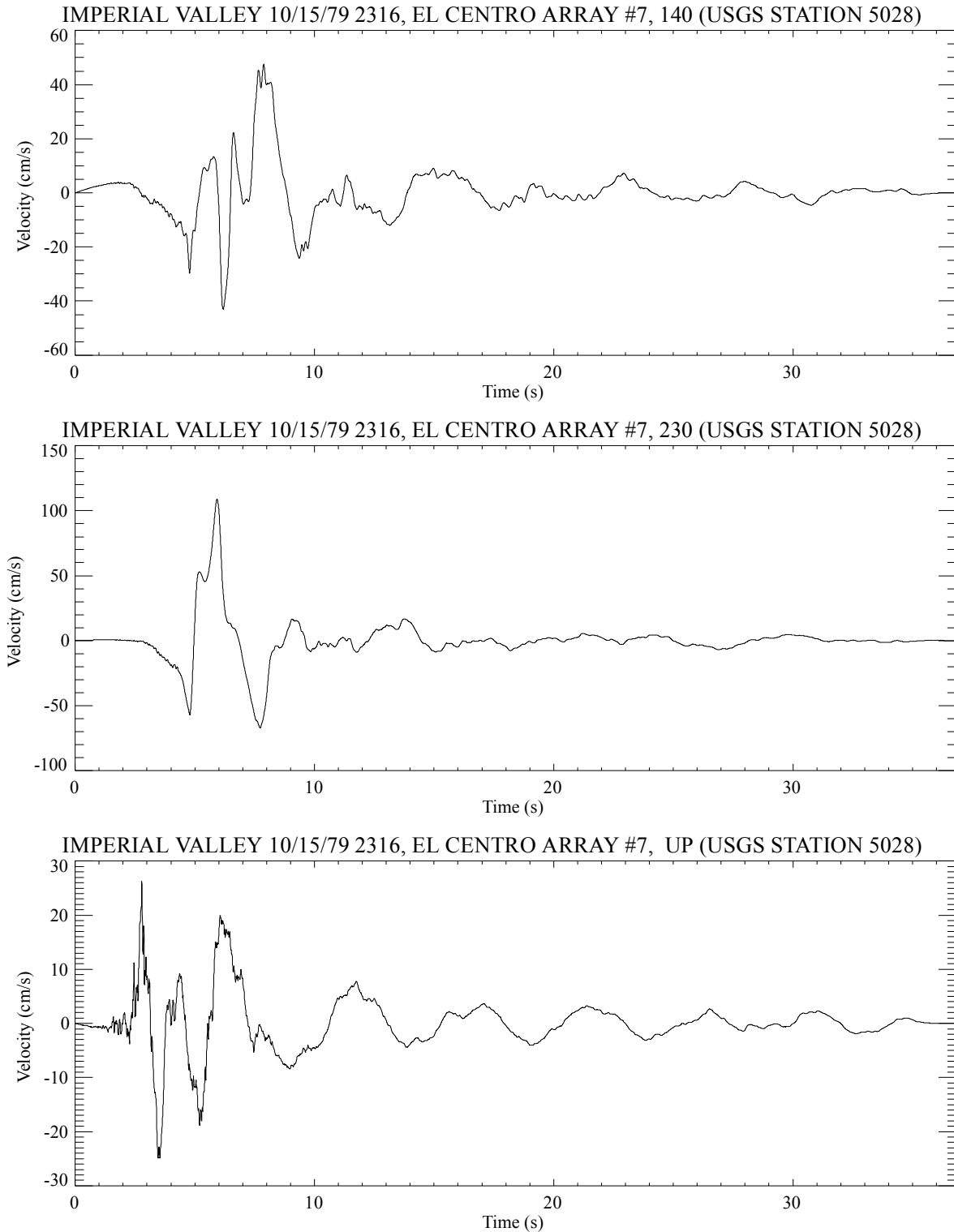


Figure 7-6: El Centro Array station E07 velocity seismograms. Vertical is labeled UP. Horizontal components are labeled by their orientation in degrees east of north (e.g., 140° and 230°). See Figure 7-1 for station position relative to fault rupture. The horizontal components are oriented in approximately strike-normal (230°) and strike-parallel (140°) directions relative to the strike of the Imperial fault.

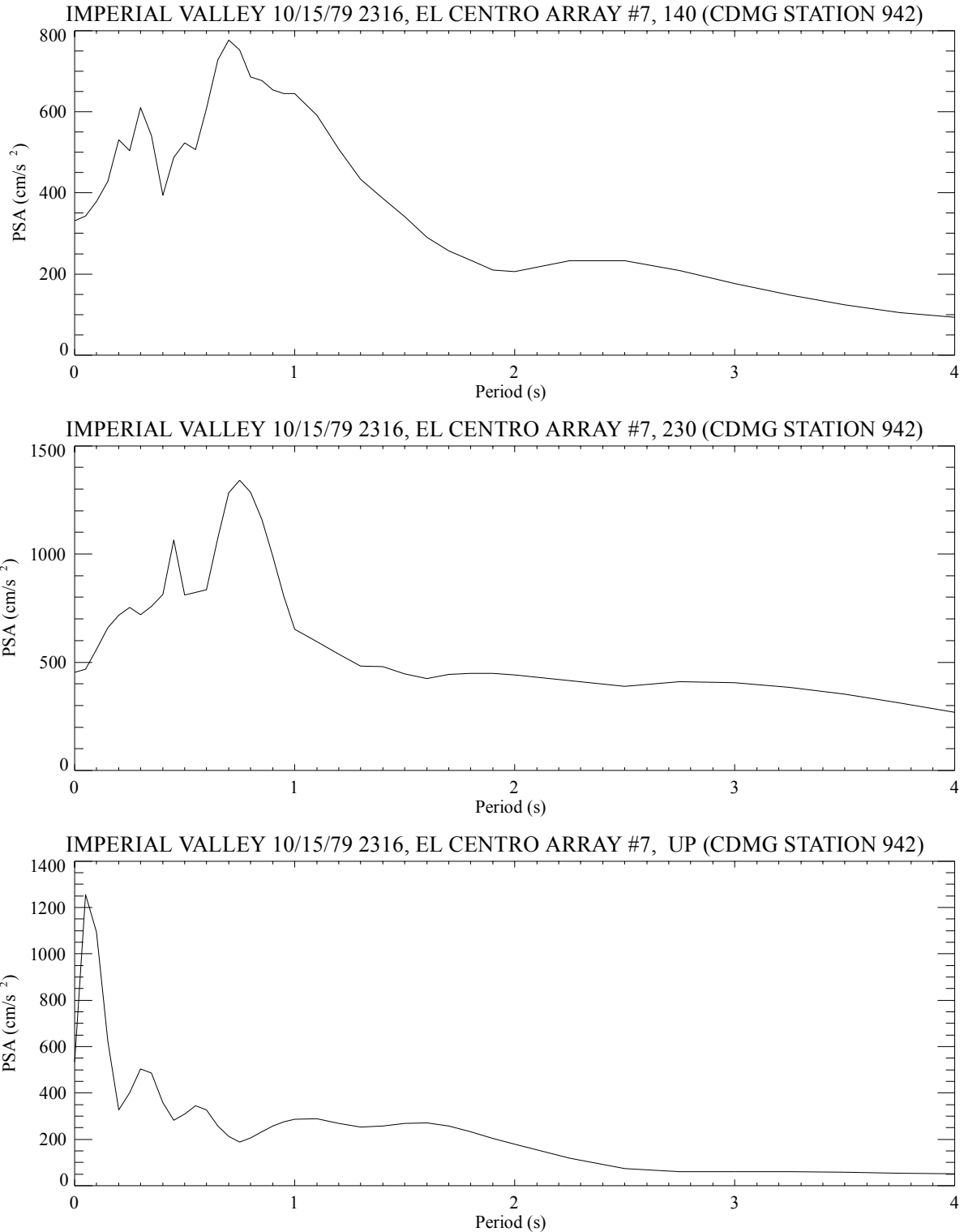


Figure 7-7: El Centro Array station E07 pseudo-acceleration response spectra. Vertical is labeled UP. Horizontal components are labeled by their orientation in degrees east of north (e.g., 140° and 230°). See Figure 7-1 for station position relative to fault rupture. The horizontal components are oriented in approximately strike-normal (230°) and strike-parallel (140°) directions relative to the strike of the Imperial fault.

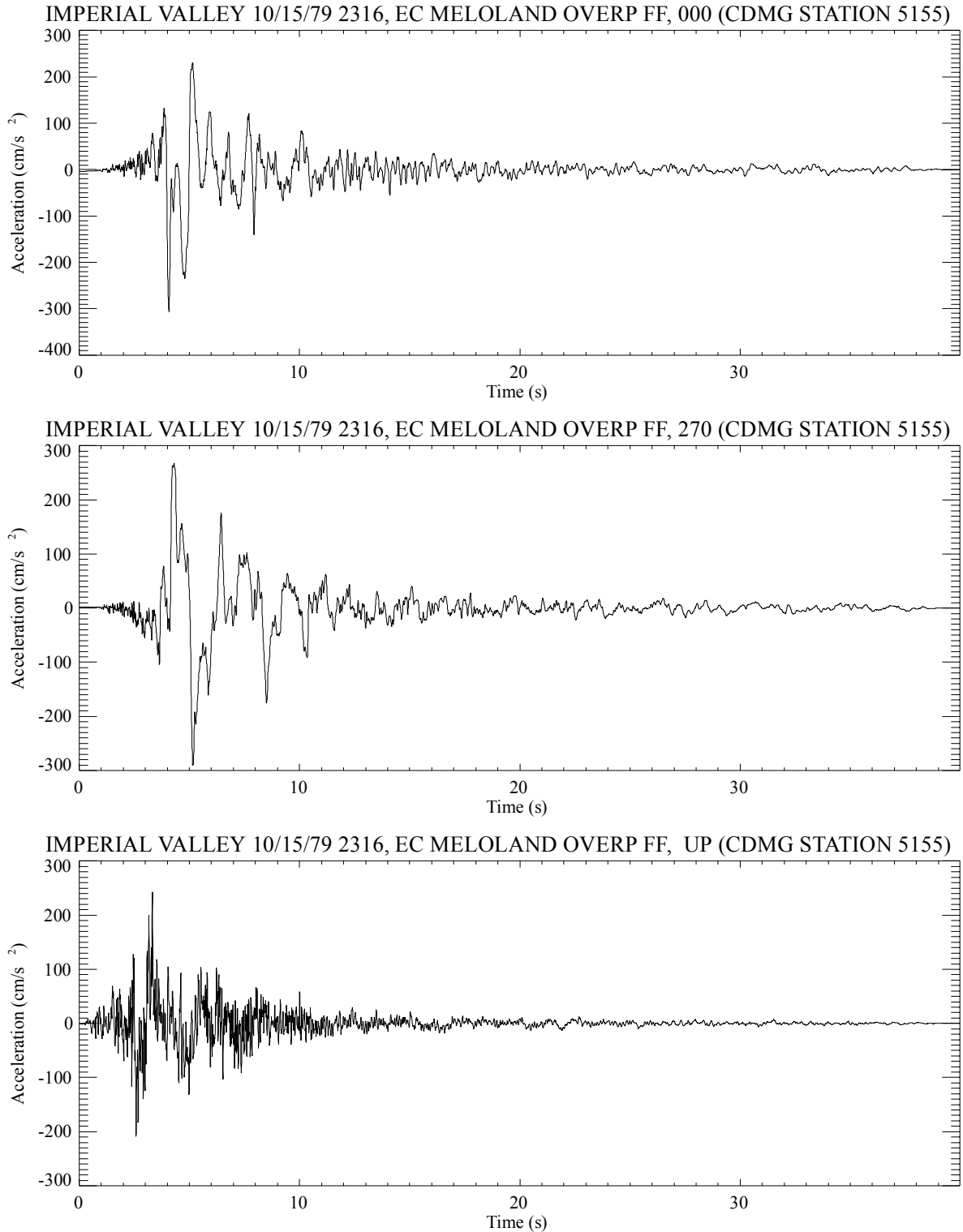


Figure 7-8: El Centro Array station EMO acceleration seismograms. Vertical is labeled UP. Horizontal components are labeled by their orientation in degrees east of north (e.g., 0° and 270°). See Figure 7-1 for station position relative to fault rupture.

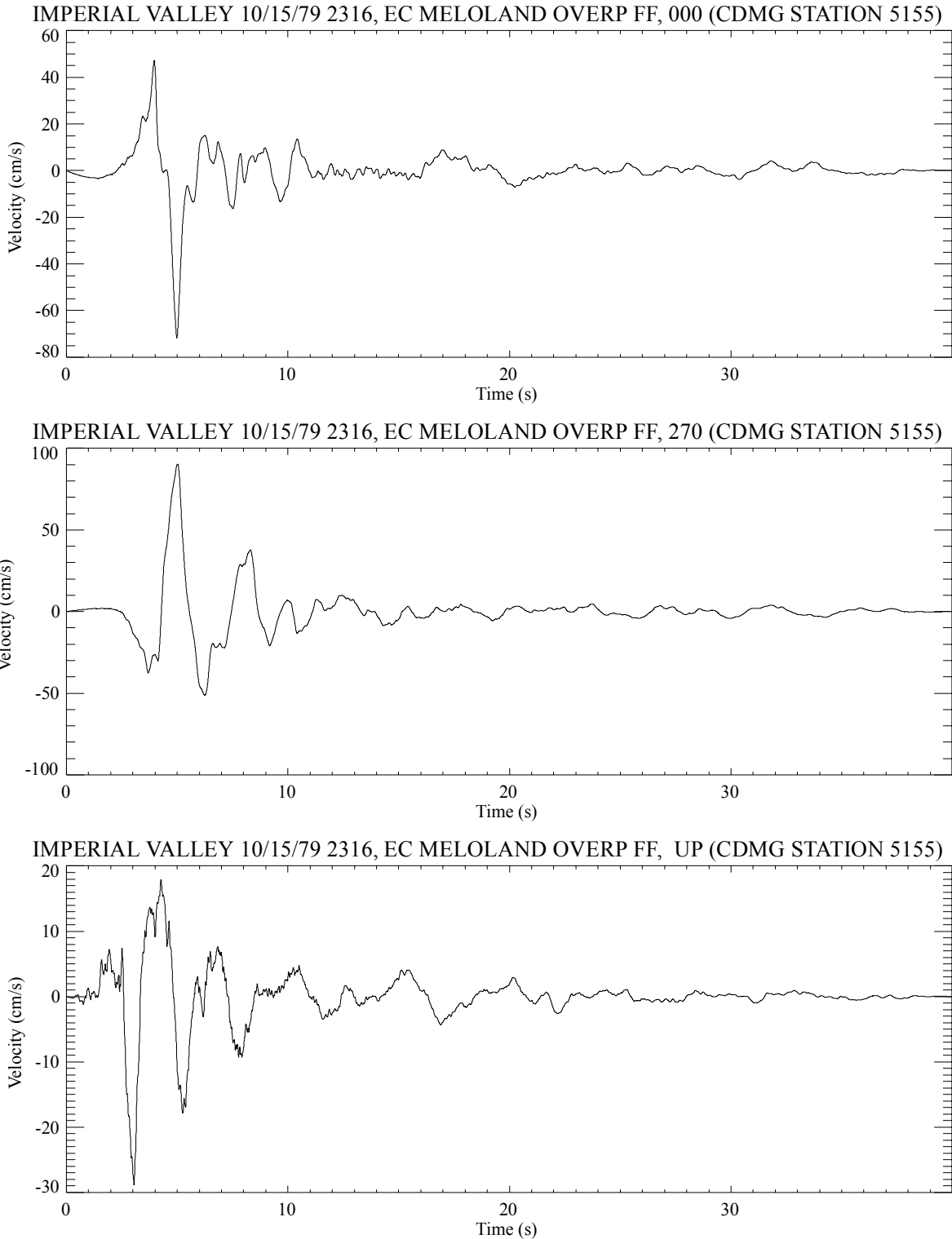


Figure 7-9: El Centro Array station EMO velocity seismograms. Vertical is labeled UP. Horizontal components are labeled by their orientation in degrees east of north (e.g., 0° and 270°). See Figure 7-1 for station position relative to fault rupture.

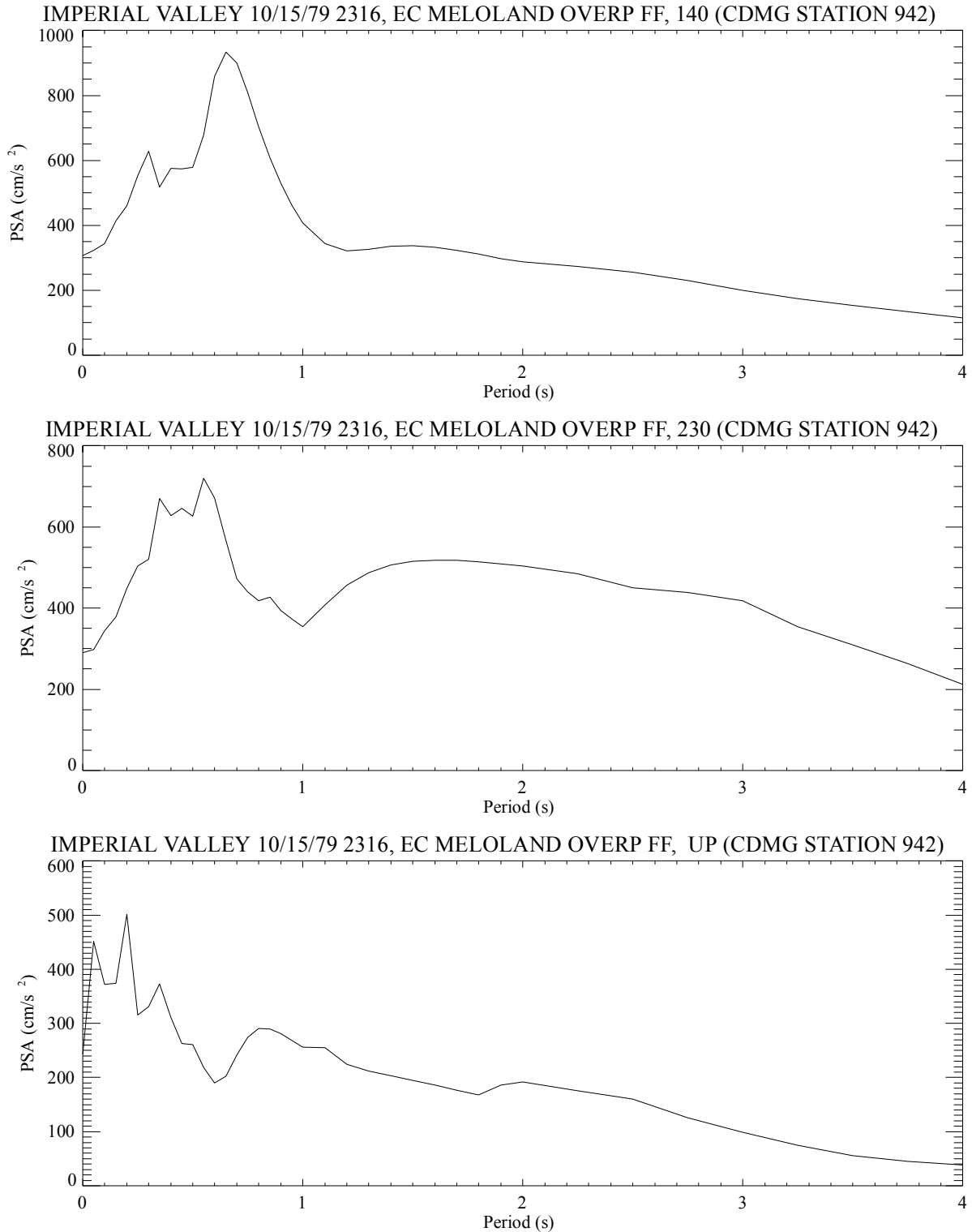


Figure 7-10: El Centro Array station EMO pseudo-acceleration response spectra. Vertical is labeled UP. Horizontal components are labeled by their orientation in degrees east of north (e.g., 0° and 270°). See Figure 7-1 for station position relative to fault rupture.

low-velocity sediments and the basement at Jackson Lake Dam, the large ($> 0.5 g$) > 2 -s-period acceleration responses make physical sense, particularly with respect to the incidence angle criteria of Somerville et al. (2003) for predicting the amplification of long-period motions in low-velocity basin. Sections 7.4 and 7.5 use broadband site recordings of earthquakes at Jackson Lake Dam to evaluate the likelihood of unusually large > 2 -s-period acceleration responses at the dam. To reduce ground motion uncertainties associated with ground motion synthesis approaches, the next two sections present and evaluate two source models and ground motion simulation approaches. First, in Section 7.2, the kinematic rupture model of Section 6 is used to simulate near-source ground motions from the 1994 $M 6.7$ Northridge earthquake. A simplified ground motion synthesis technique developed in Frankel (1995) is summarized in Section 7.3 in preparation for its application with the broadband earthquake records to simulation ground motions at Jackson Lake Dam from $M 7.1$ earthquakes on the northern Teton fault segment in Sections 7.4 and 7.5.

7.2 Performance of the Kinematic Rupture Model

The primary purpose of the synthetic ground motion modeling in this report is to determine peak ground motion responses, ground motion variability, and durations as a function of site position relative to the Teton fault. To establish that the synthetic ground motion modeling approach outlined in Section 6 (in particular, the stochastic kinematic rupture model) provides a reasonable basis to estimate peak ground motions, synthetic Green's functions are used to calculate ground motions at near-source sites that recorded strong ground motions from the 1994 $M 6.7$ Northridge, California, blind thrust earthquake using the same ground motion simulation methods used in Section 6.

The peak ground motions at a site near a fault are strongly dependent on the orientation of the fault relative to the site and details of the fault rupture. These differences in peak ground motions are well illustrated using peak velocity and acceleration data from the Northridge blind thrust earthquake (Figure 7-11). Sites located within about 5 km of the fault tip were subjected to updip rupture directivity and typically experienced peak velocities in the 80-160 cm/s range and peak accelerations between 500 cm/s^2 and 1000 cm/s^2 . Sites outside this zone experienced peak velocities of less than about 50 cm/s and accelerations generally less than 500 cm/s^2 .

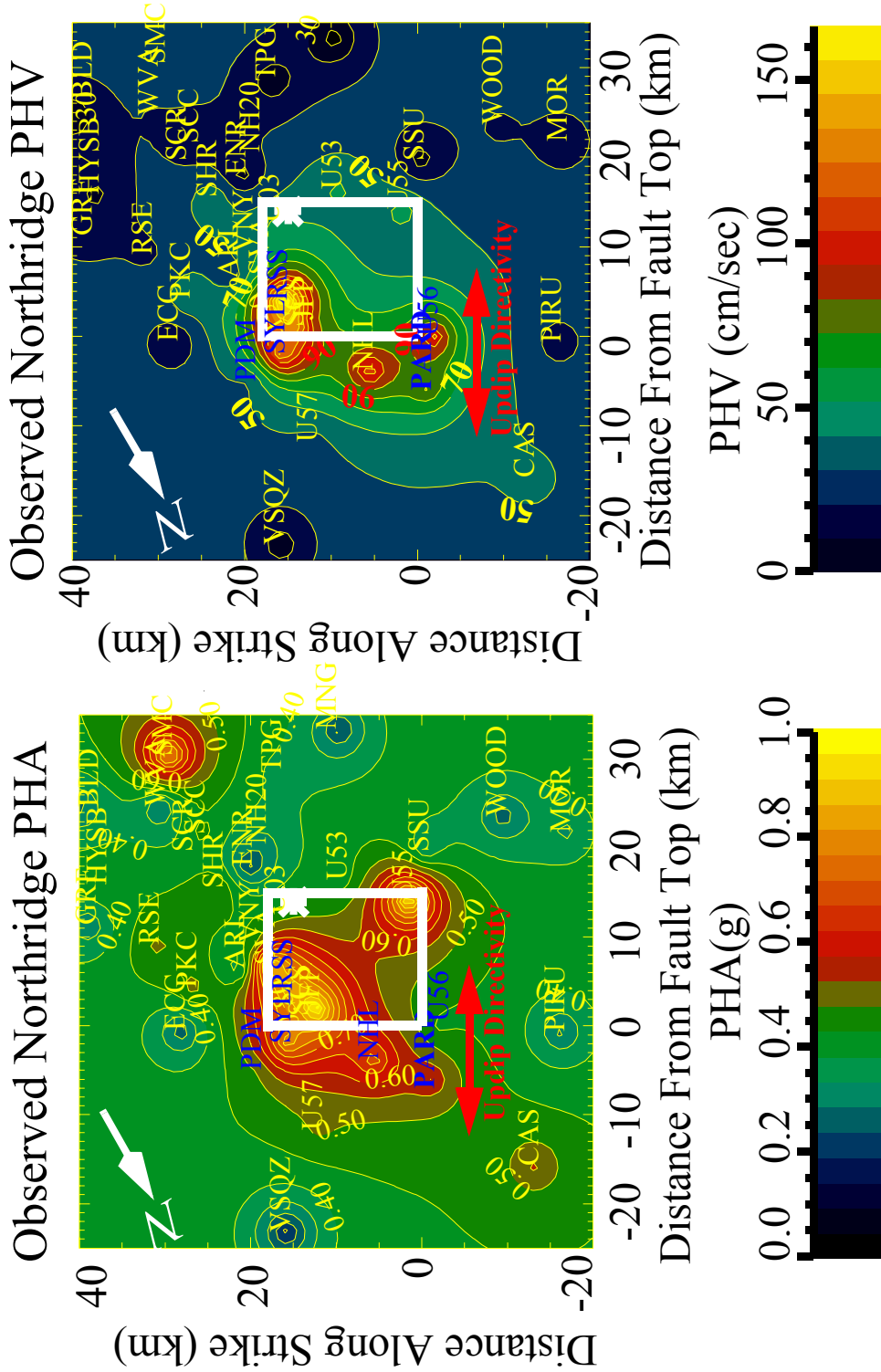


Figure 7-11: Plan view of observed peak velocities and accelerations from the M 6.7 1994 Northridge earthquake. The stations used in ground motion model are labeled in blue. The extent of pronounced rupture directivity around the fault tip is shown in red. The white box outlines the surface projection of the fault plane. The top of the fault is to the left at 5 km depth and the fault extends to 20 km depth at a dip of 45 degrees.

While the Northridge earthquake provides a nice illustration of directivity, it is important to realize that there are significant differences between conditions at Northridge and Jackson Lake Dam. However, for the purposes of evaluating the performance of the kinematic rupture model, these differences are probably not important.

7.2.1 Validation Ground Motion Modeling Approach: Green's Functions. Site-specific ground motion recordings were used in Section 6 to simulated strong ground motions. Here, purely theoretical Green's functions appropriate for crustal and site conditions in the near-fault region of the Northridge earthquake are used and it is necessary to discuss them in detail. Bernard and Madariaga (1984) and Spudich and Frazer (1984; 1987) developed the isochrone integration method to compute near-field seismograms for finite-fault rupture models. Isochrones are all the positions on a fault that contribute seismic energy that arrives at a specific receiver at the same time. The simplest way to employ the isochrone method in the near-field is to assume that all significant seismic radiation from the fault consists of direct shear-wave arrivals. This assumption is reasonable in the near-field, particularly for a deeply buried, blind-thrust fault that produces dominantly near-vertical source-receiver paths. A further simplification is to use a simple trapezoidal slip-velocity pulse. Let $f(t)$ be the slip function, For simplicity we assumed $\ddot{f}(t) = \delta(t - t_r) - \delta(t - t_h)$, where t_r is rupture time, and t_h is healing time. Then, all seismic radiation from a fault can be described with rupture and healing isochrones. Surface ground motions velocities, v , and accelerations, a , from rupture or healing can be calculated from (Spudich and Frazer, 1984)

$$v(\mathbf{x}, t) = \ddot{f}(t) \otimes \int_{y(t, \mathbf{x})} (\mathbf{s} \cdot \mathbf{G}) c dl \quad (7-1)$$

$$a(\mathbf{x}, t) = \ddot{f}(t) \otimes \int_{y(t, \mathbf{x})} \left[c^2 \left(\frac{d\mathbf{s}}{dq} \cdot \mathbf{G} \right) + c^2 \left(\frac{d\mathbf{G}}{dq} \cdot \mathbf{s} \right) + \frac{dc}{dt} \cdot (\mathbf{s} \cdot \mathbf{G}) \right] dl \quad (7-2)$$

where c is isochrone velocity, \mathbf{s} is slip velocity (either rupture or healing), $d\mathbf{q}$ is the spatial derivative, $y(t, \mathbf{x})$ defines the isochrone, and \mathbf{G} is a hybrid ray theory Green's function combined with synthetic 3D scattering functions or microearthquake ground motions recorded at the dam as described below.

Spudich and Frazer (1984) showed that c can be eliminated from (7-1) by integrating along an isochrone over a finite time window defined by the isochrones $t - dt$ and $t + dt$. By limiting the integration to frequencies lower than 10 Hz ($dt = 0.05$ s) band-limited ground motions are obtained making the isochrone method useful for qualitatively evaluating accelerations. This approach was used here with a first-order approximation, where (7-1) was reduced to a point-source summation of over the isochrone strip corresponding to the finite time window:

$$v(\mathbf{x}, t) = \ddot{f}(t) \cdot \int_A \int s_r \cdot \mathbf{G}^S \frac{1}{dt} B \left[\frac{(t - t^S)}{dt} \right] dA \quad (7-3)$$

We used this approach to efficiently calculate seismograms for a large number of receiver positions relative to a fault. For the point source integrations, the ray theory portion of \mathbf{G} was approximated as

$$G^S(x, \xi) = \frac{F(x, \xi) \cdot \tilde{W}(x, \xi)}{4\pi \sqrt{\rho(x)\rho(\xi)\beta(x)\beta(\xi)}^{5/2} \sqrt{(x - \xi)^2}} \quad (7-4)$$

where x is the receiver position, ξ is position on the fault, $F(x, \xi)$ is the source radiation term, $\tilde{W}(x, \xi)$ is the free surface amplification factor, ρ is density, and β is the shear-wave velocity. In this approximation, only first shear arrivals are included in the calculation. Although ray spreading factors are simply approximated by the inverse source-receiver distance, a 1D approximation consistent with crustal shear-wave velocities in southern California, was used to calculate, $\beta(\xi)$, takeoff angles for $F(x, \xi)$, and incidence angles for $\tilde{W}(x, \xi)$ to incorporate first-order geometric effects of vertically heterogeneous velocity structure which varied from $\beta=1.7$ at the surface to $\beta=3.5$ km/s at 9 km depth (details in O'Connell, 1999a). This produced realistic partitioning of S_V velocities between vertical and horizontal components of ground motion.

The amplitude effects of S_V transmission were approximated by computing the median vertical-incidence amplification of a band-limited (0.5-5 Hz) S_V plane wave propagated through a 3D heterogeneous media. A self-similar, fractal correlation model of random spatial variations of crustal seismic velocities with an autocorrelation function, P , of the form

$$P(k_r) \approx \frac{a^n}{1 + (k_r a)^n} \quad (7-5)$$

where a is the correlation distance, k_r is the radial wavenumber, and $n = 3$ was used in a 3D elastic finite-difference calculation to compute S_V transmission amplification through the top 9 km of the crust. The free-surface was omitted since (7-4) was used to calculate free-surface amplification. The 3D randomization of the 1D velocity model was normalized to produce a standard deviation of 5% of β for $ak_r \gg 1$ with $a = 2.5$ km.

O'Connell (1999a) showed that 3D scattering in the upper crust can have a significant influence on the scaling of near-field peak ground motions. Scattering of direct S_V waves by correlated-random crustal velocity variations tends to reduce peak horizontal velocities associated with near-field rupture directivity by increasing the time and phase dispersion of direct S_V waves. Scattering is included here using the 3D finite-difference approach of Graves (1996) to produce synthetic three-component S_V scattering functions. S_V plane waves were propagated at incidence angles of 80° and azimuths of 45° and 135° relative to the strike of the steeply-dipping sedimentary rocks through the upper 2 km of the crust using a velocity structure typical of fold-and-thrust belts (Figure 7-12). Three-component S_V scattering functions were obtained for receiver positions within the high-velocity portion of the velocity model as shown in Figure 7-12. The depth limit of 4 km in the 3D velocity model was dictated by the need to produce scattering functions to a maximum frequency of 10 Hz, the horizontal dimensions necessary to sample a 2.5 km correlation distance adequately (12 km), and the limitations of fitting a 3D elastic finite-difference calculation into computer memory.

The 3D scattering functions were normalized so that the median peak velocity for each component matched the median S_V transmission amplifications derived above. Geometric spreading and free-surface amplification were applied using (7-4). A 3D scattering function was chosen at random at each integration position in the point source summation from a total of 5200 scattering functions used in the ground motion simulations.

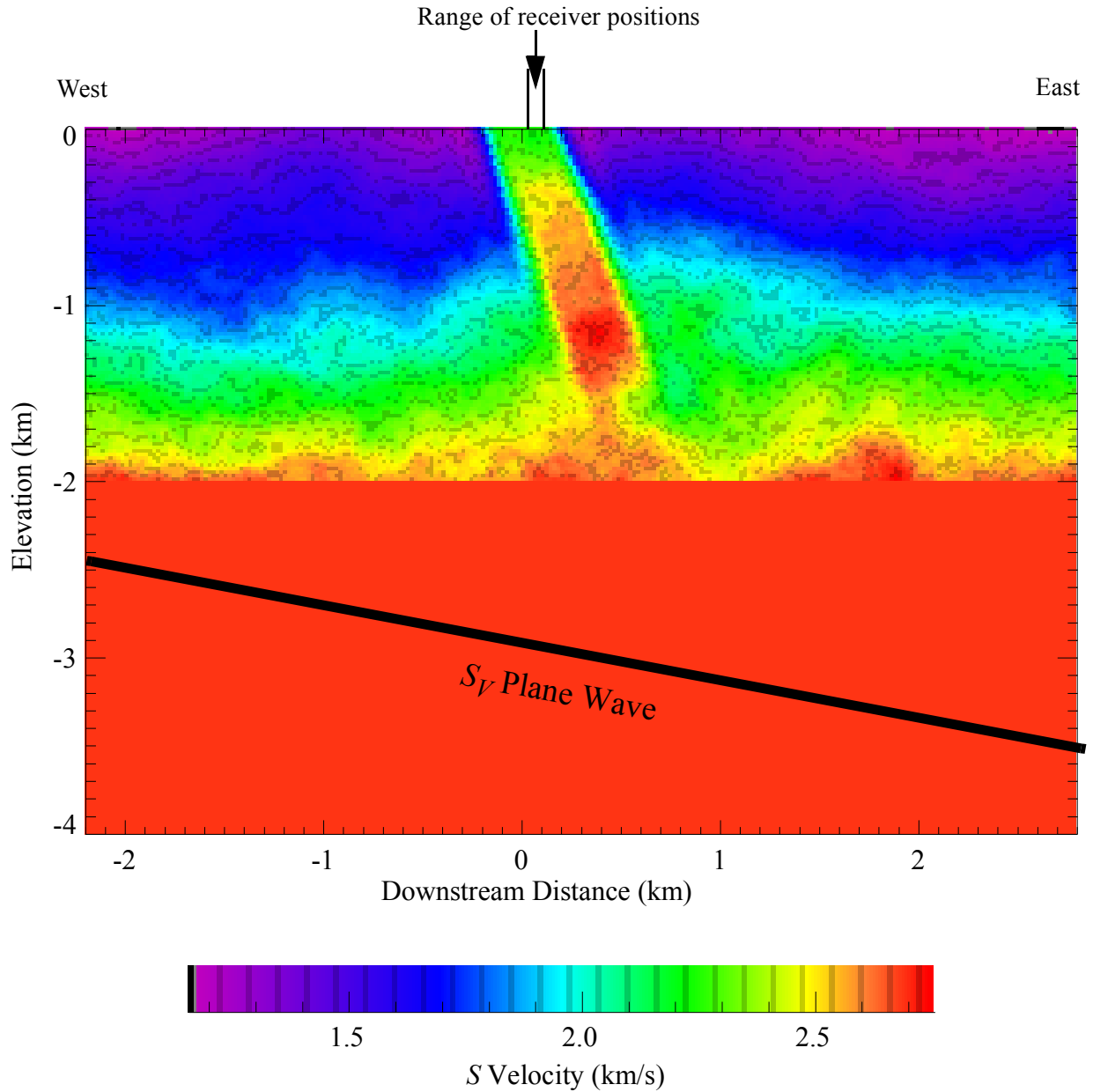


Figure 7-12: S -wave velocity profile from a 3D randomization of a 2D velocity model for the top 2 km of the crust. For (7-5) $n=2$ and $a=1$ km. A 2 km thick homogeneous region is inserted at the bottom to introduce a uniform amplitude S_V plane wave. The scattering functions for the ground motion simulations were derived using $n=3$ and $a=2.5$ km to produce the 3D randomization of the 2D velocity model. The standard deviation of the velocity randomization was set to 5% for all cases. The extent of the region used to extract scattering functions is shown at the top.

The scattering functions possess fairly simple waveforms (see Figures 7-13 and 7-14). The scattering function responses are consistent with the rather simple site responses; coda durations are relatively short, and direct *S* waveforms are fairly simple. Shear-wave splitting is often observed associated with folded sedimentary rocks. Consequently, kinematic time-shifting of horizontal components was used to delay east-west polarized, direct *S* waves relative to north-south components using the method described in O'Connell (1999c).

7.2.2 Kinematic Rupture Model Test: Northridge Ground Motions. The synthetic Green's function from Section 7.2.1 are used to provide rock-site synthetic ground motions. A total of 200 random rupture models were generated using the approach in Section 6.2 to simulate strong ground motions at the six stations shown in blue in Figure 7-11. The station naming convention follows Wald et al. (1996). The **M** 6.7 Northridge hypocenter was fixed at a depth of 19 km and 1.5 km from the eastern edge of the fault. Figures 7-15 to 7-20 show the rupture model that produced the best fit to six near-fault strong motion recordings and illustrate detailed aspects of the kinematic rupture model used in Section 6.

A large number of parameters must be specified in the kinematic rupture model. Velocity ground motions are the direct outputs of the simulations, from which, all other quantities, such as accelerations and response spectra, are obtained. Fractal parameterizations of effective stress (Figure 7-15) produce slip velocity models (Figure 7-16) consistent with the dynamic rupture modeling results of Boatwright and Andrews (1998). The rise times (Figure 7-17) are specified using an approach similar to Herrero and Bernard (1994) which makes rise time inversely proportional to effective stress (Figure 7-15). Let k be spectral wavenumber and ω be angular frequency. Resulting fault slip models (Figure 7-18) are consistent with the k^{-2} decay slip behavior proposed by Somerville et al. (1999), based on analyses of slip inversions for recent earthquakes. The synthetic slip models also have displacement spectra with a ω^{-2} spectral decay consistent with Andrews (1980) and Frankel (1991). For the Jackson Lake Dam ground motion simulations, effective stress correlation lengths were increased by 33% relative to the **M** 6.7 Northridge rupture simulations of this section to be consistent with the empirical relations of Somerville et al. (1999), that indicate that asperity size increases with magnitude. Rupture

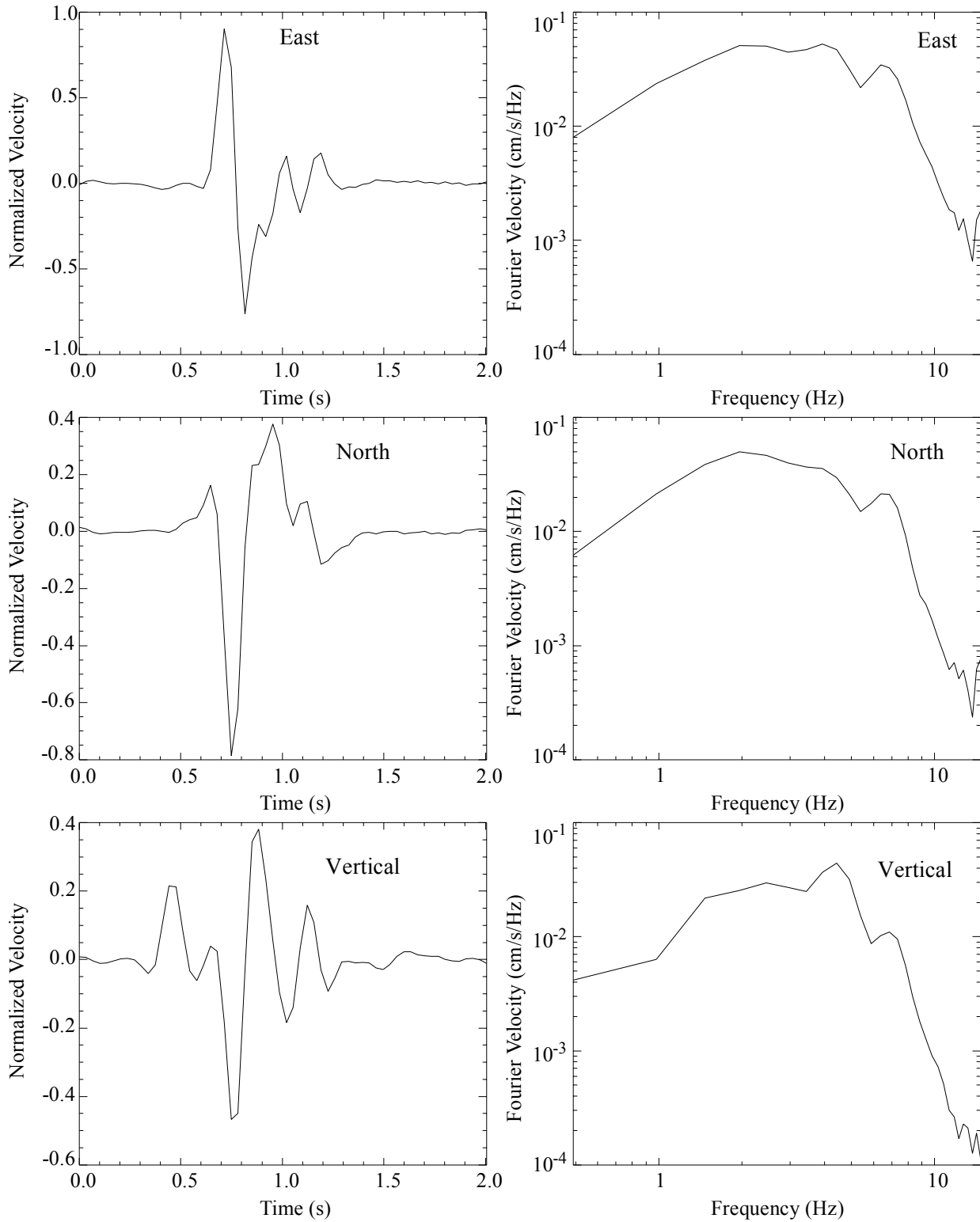


Figure 7-13: First example of a synthetic three-component S_V scattering function. Normalized velocity waveforms on the left and Fourier velocity spectra on the right for the components as labeled.

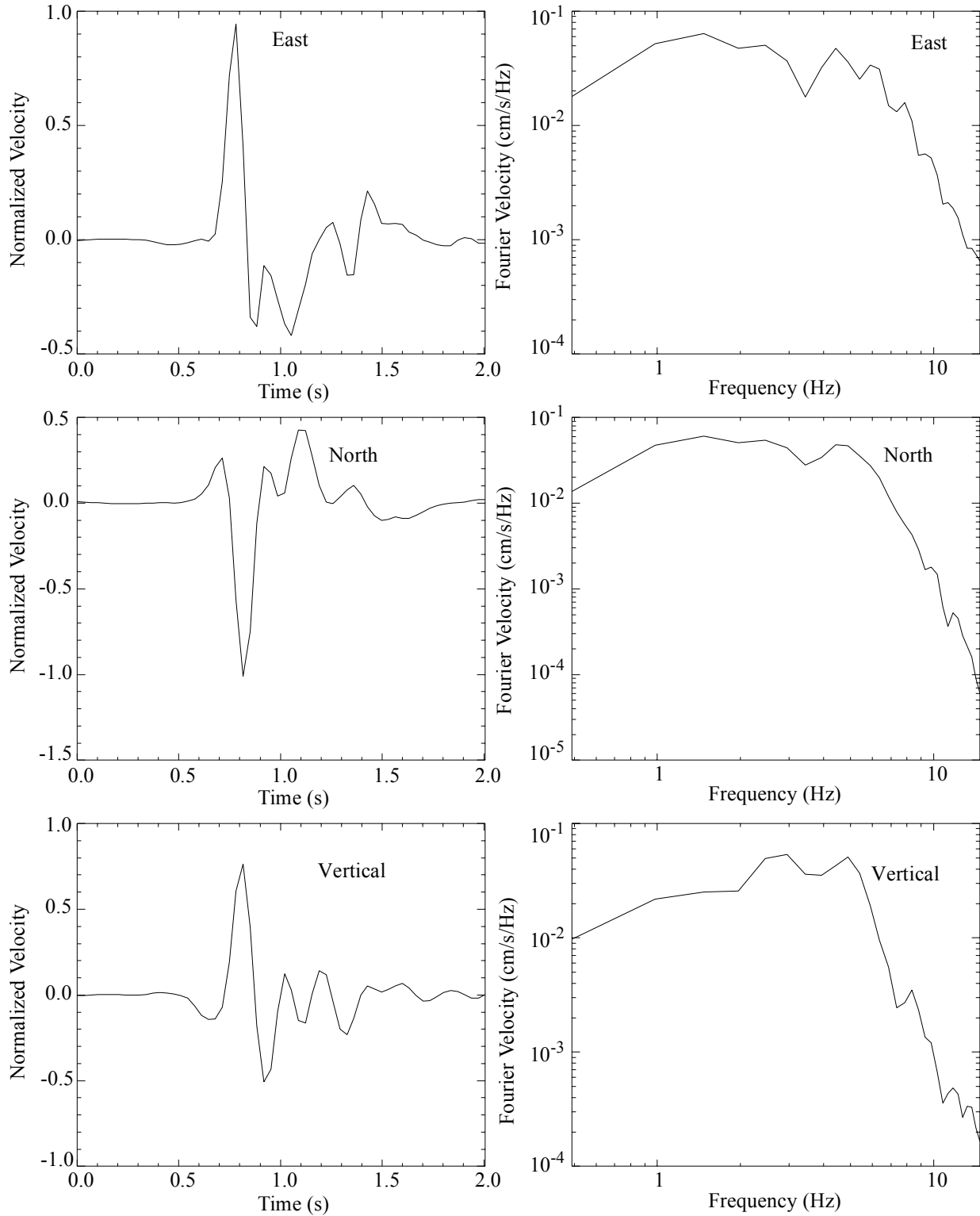


Figure 7-14: Another example of a synthetic three-component S_V scattering function. Normalized velocity waveforms on the left and Fourier velocity spectra on the right for the components as labeled.

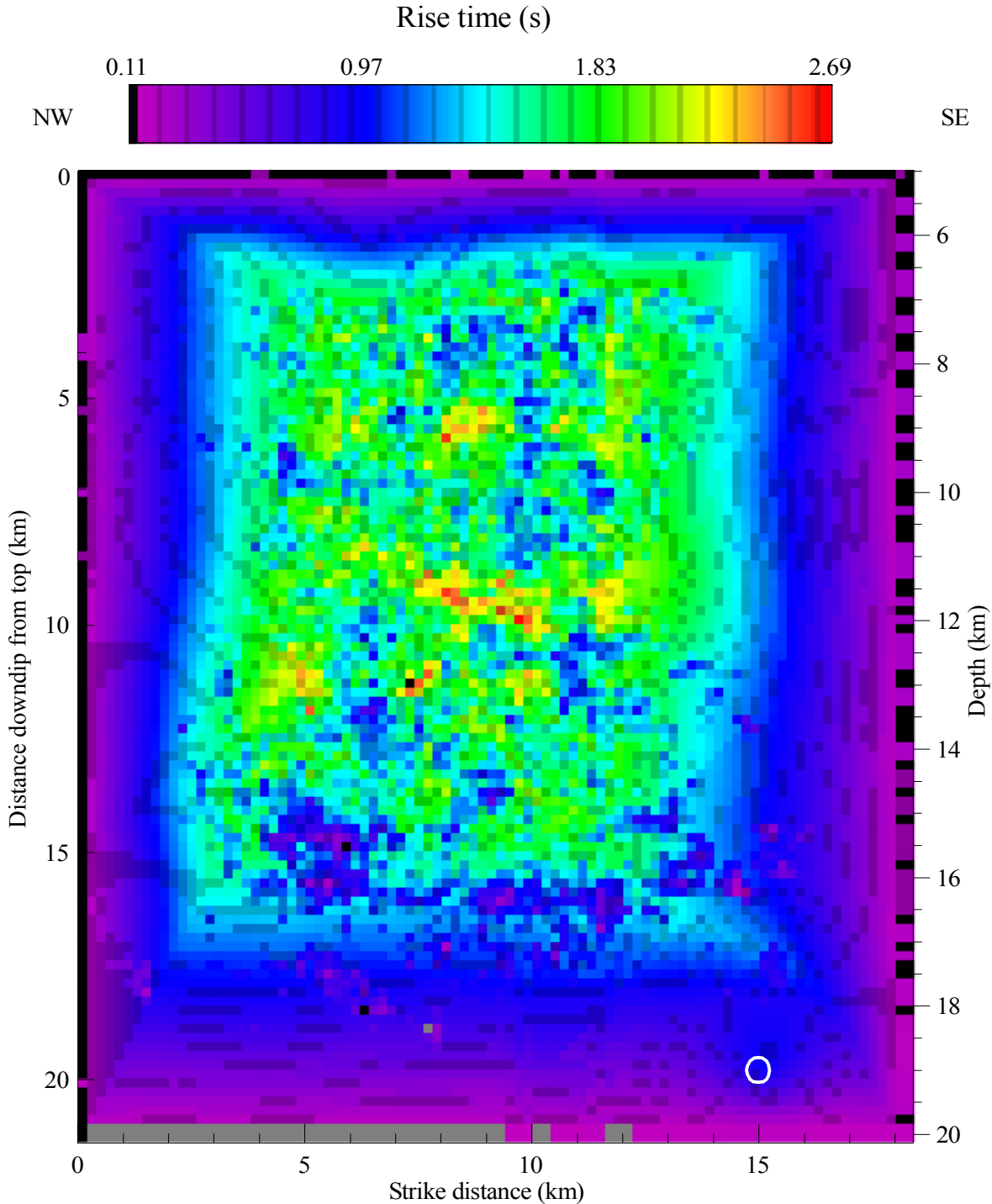


Figure 7-17: Rise-time distribution that produced the best-fitting Northridge ground motion . Since rise time is inversely proportional to slip velocity (Figure 7-16), it is dependent on effective stress (Figure 7-15) and rupture time (Figure 7-20). The perspective is looking down, normal to the fault plane. The hypocenter is the white circle. The fault is discretized using a 0.2 km spacing. The healing of the fault boundaries tapers rise times toward zero at the boundaries, resulting in a tapering of slip toward the boundaries as well (Figure 7-18). In the interior of the fault, rise time strongly inversely correlates with slip velocity (Figure 7-16).

velocities were allowed to vary over a wide range (between 0.6β to 1.05β , see Figure 7-19) to allow rupture directivity caustics to develop, and to produce variable rupture times (Figure 7-20). A large number of assumptions and choices must be made to specify an earthquake rupture models. Some of the interdependencies between different rupture parameters are discussed in the captions of Figures 7-15 to 7-20.

A scale factor of 1.5 was used for the five stiff soil sites since hard-rock site-specific stochastic 3D Green's functions were used at all sites, consistent with the results of Field et al. (1997). The scale factor for the Paicoma Dam (PDM) record was set to one since its foundation shear-wave velocities of ~ 2 km/s correspond to a hard rock site. The rupture model that produced the best-fitting synthetic peak azimuth oriented velocity and acceleration horizontal ground motions (Figures 7-21 to 7-26) and response spectra (Figure 7-27) fit the observed data about as well as O'Connell (1999a; 1999c). The stochastic kinematic rupture model and synthetic Green's function reproduce the Northridge near-source strong motion data as well as the deterministic kinematic rupture model of O'Connell (1999a; 1999c).

The region of low rupture velocity west of the hypocenter in Figure 7-19 is required to reproduce the observed delays between the initial shear waves from the hypocentral region and the largest amplitude shear waves that generally occur several seconds later (Figure 7-23 to 7-25). Hartzell et al. (1996) also find a region of relatively low rupture velocity west of the hypocenter in their inversion for slip, rupture velocity, and rake associated with the Northridge earthquake. This region of low rupture velocities is the only deterministic aspect of the Northridge rupture model. All other portions of the model were generated using stochastic methods intrinsic to the kinematic rupture model of Section 6.

The slip model (Figure 7-18) is similar estimated slip from Wald et al. (1996). Hartzell et al. (1996) estimate a greater proportion of slip near the hypocenter. The stochastic rupture slip-velocity model has largest slip-velocities below 14 km depth (Figure 7-16), but the longest rise times are at shallower depths (Figure 7-17) which results in the largest slips occurring at in the top portion of the rupture (Figure 7-18). It may be possible to reconcile the contrasting slip estimates of Wald et al. (1996) and Hartzell et al. (1996), if the Wald et al. (1996) results are more sensitive

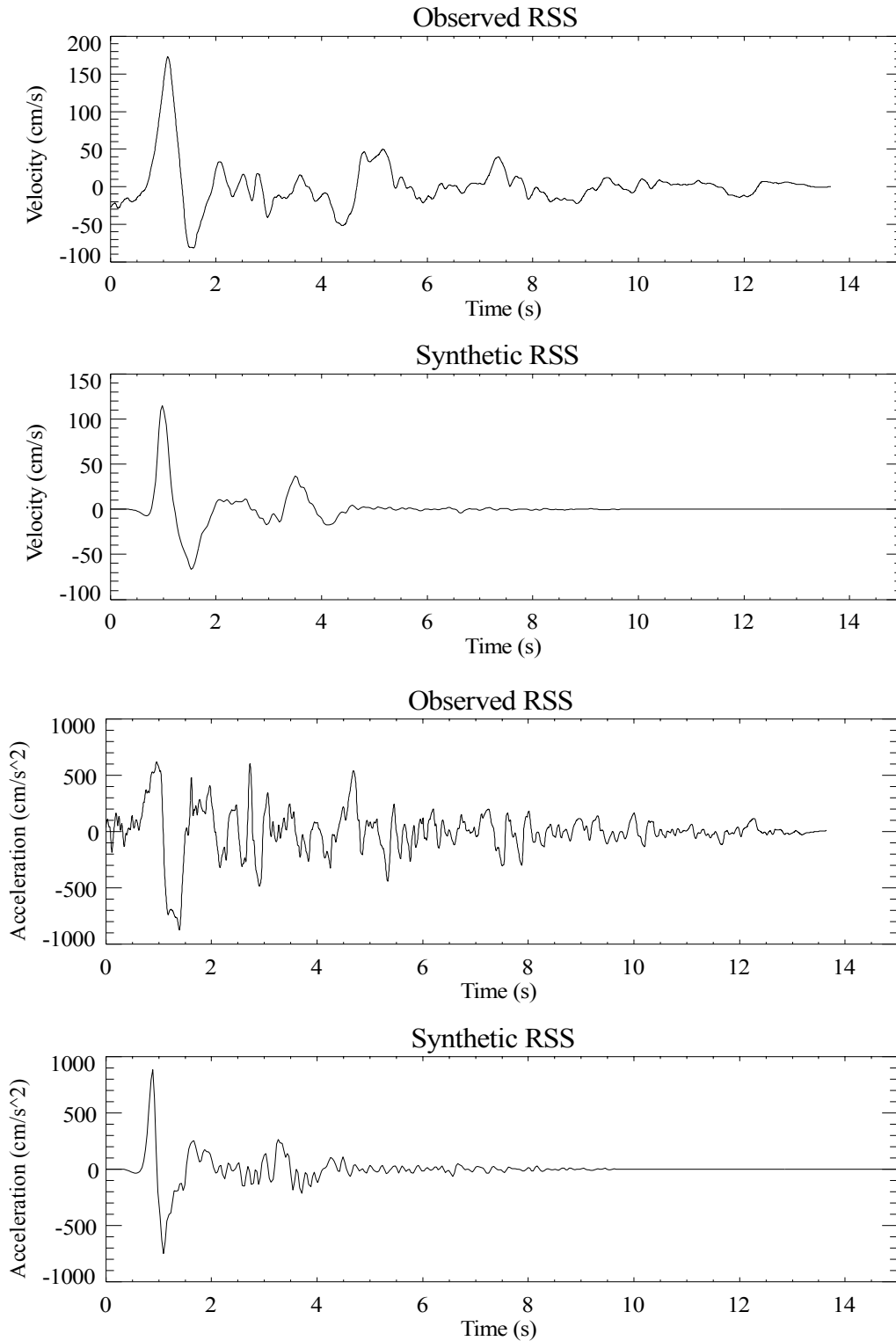


Figure 7-21: Observed and simulated peak horizontal component velocities and accelerations as labeled for station RSS (Rinaldi). Figure 7-11 provides station position.

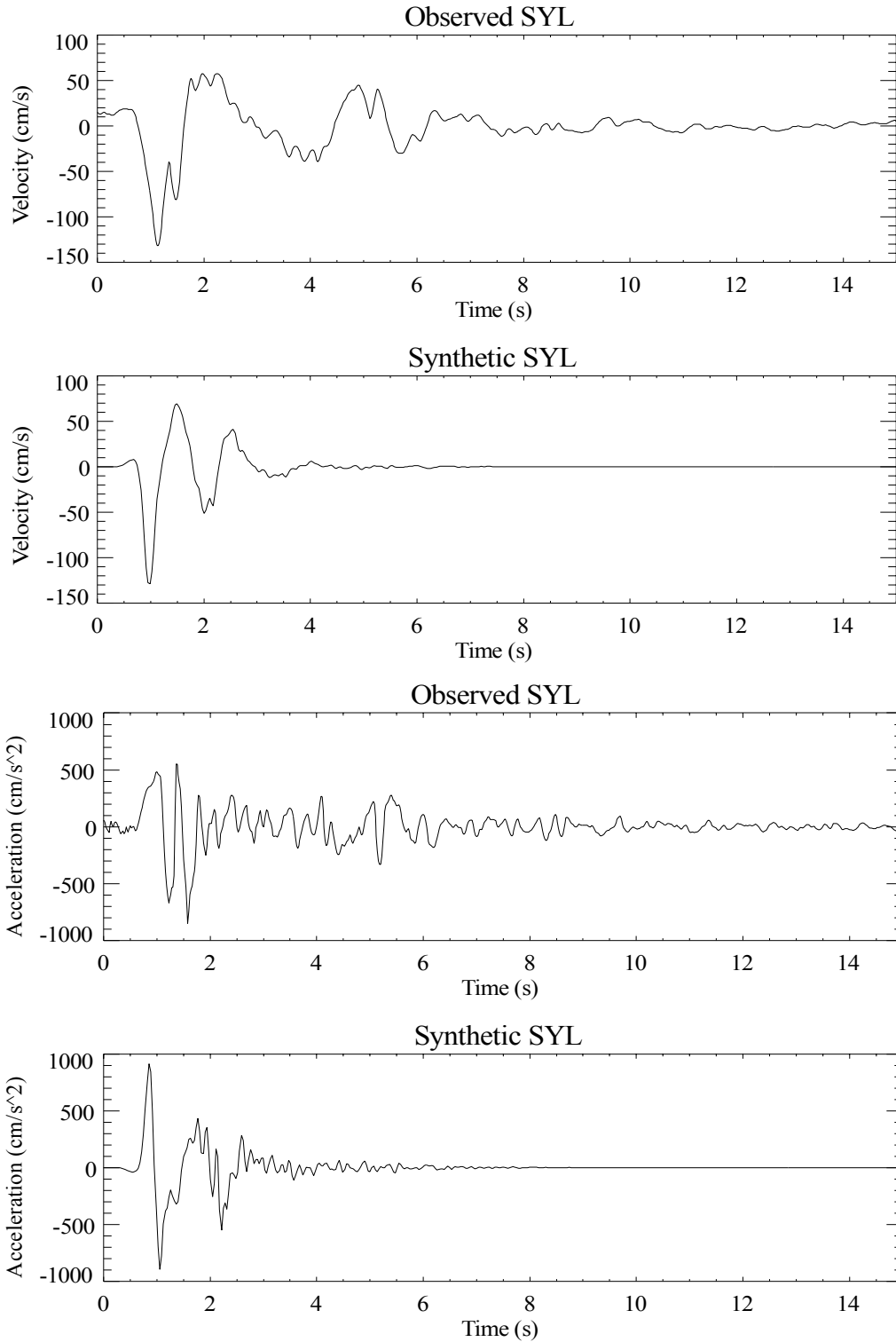


Figure 7-22: Observed and simulated peak horizontal component velocities and accelerations as labeled for station SYL (Sylmar). Figure 7-11 provides station position.

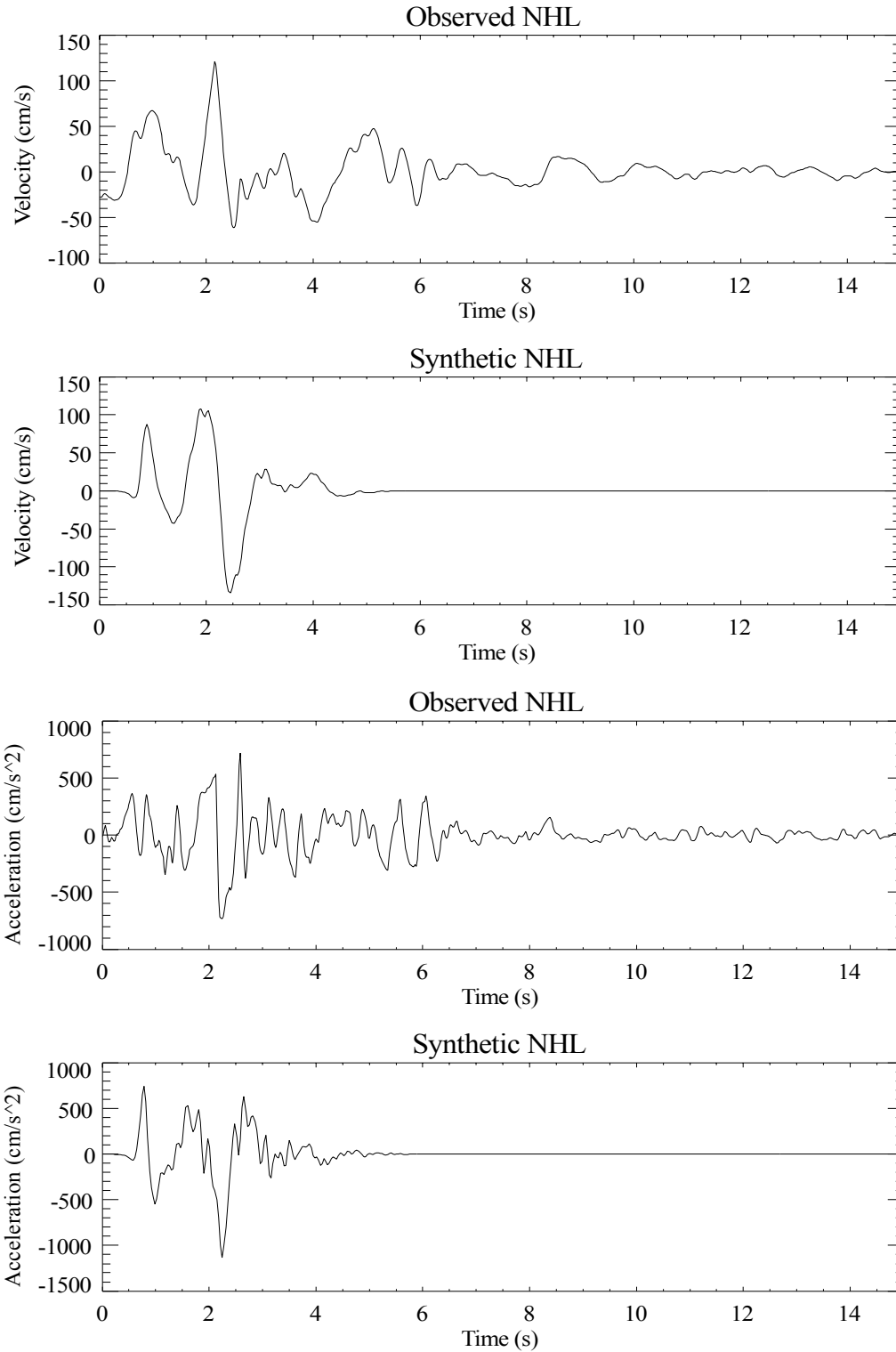


Figure 7-23: Observed and simulated peak horizontal component velocities and accelerations as labeled for station NHL (Newhall). Figure 7-11 provides station position.

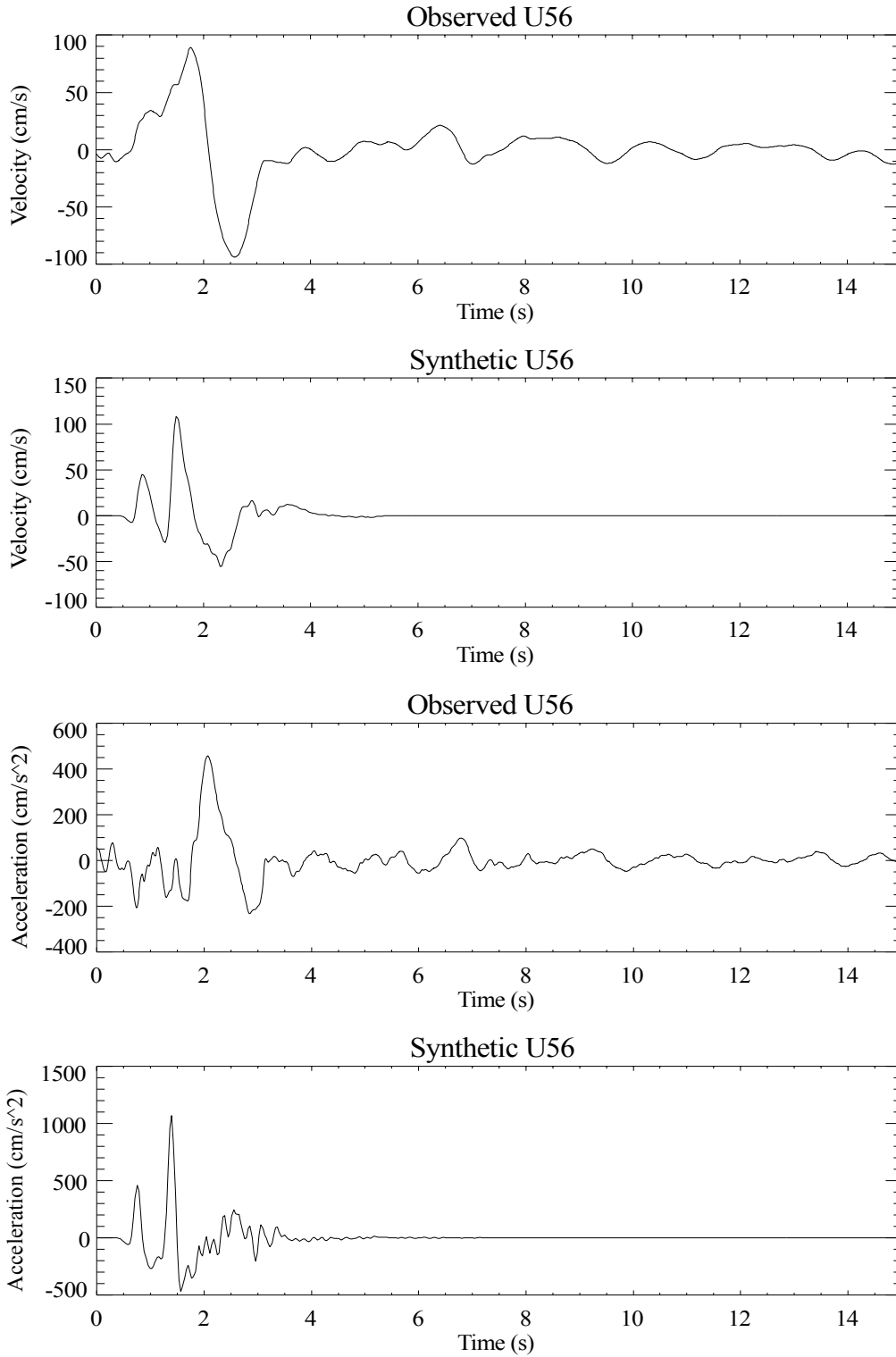


Figure 7-24: Observed and simulated peak horizontal component velocities and accelerations as labeled for station U56. Figure 7-11 provides station position.

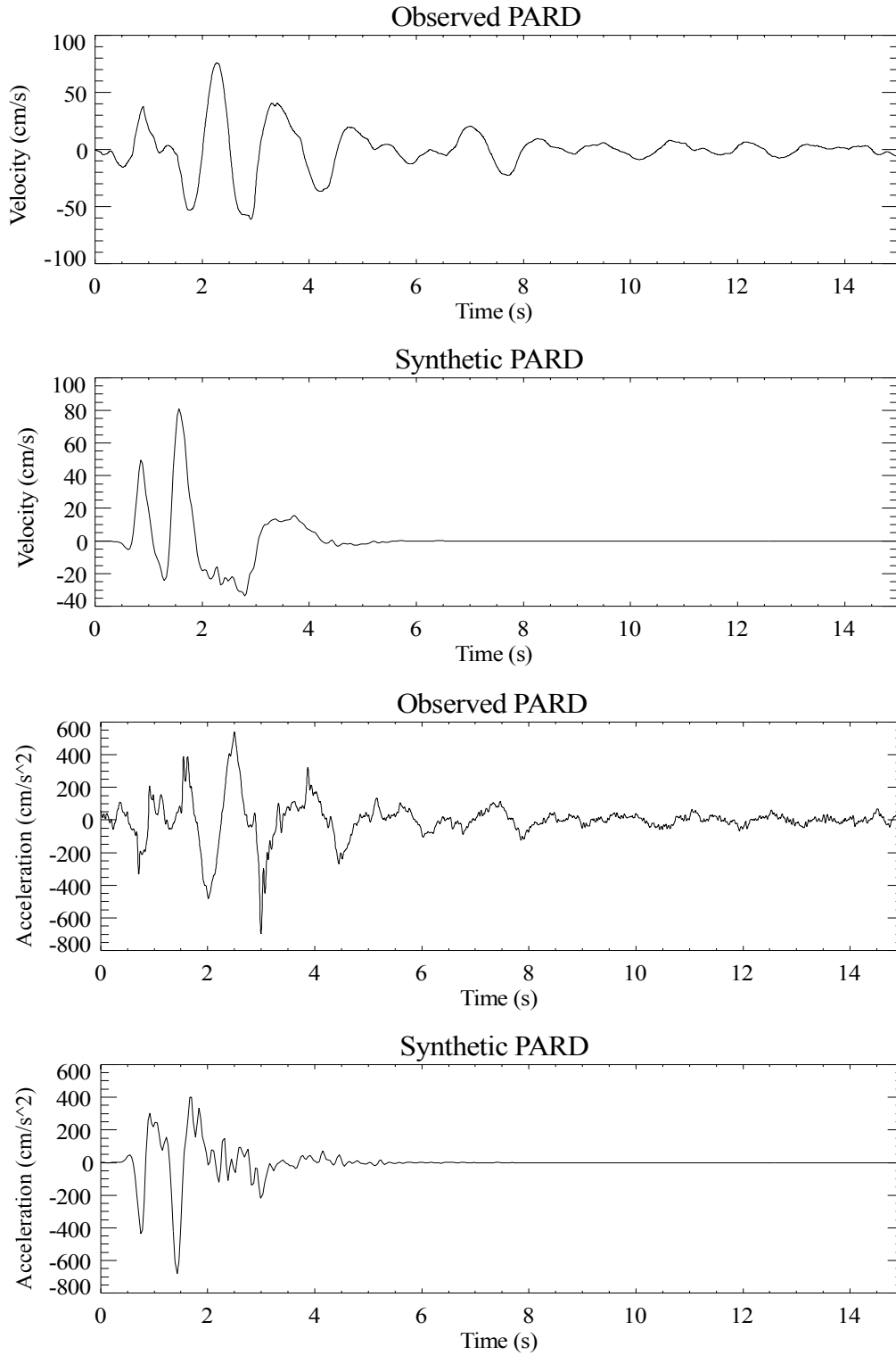


Figure 7-25: Observed and simulated peak horizontal component velocities and accelerations as labeled for station PARD. Figure 7-11 provides station position.

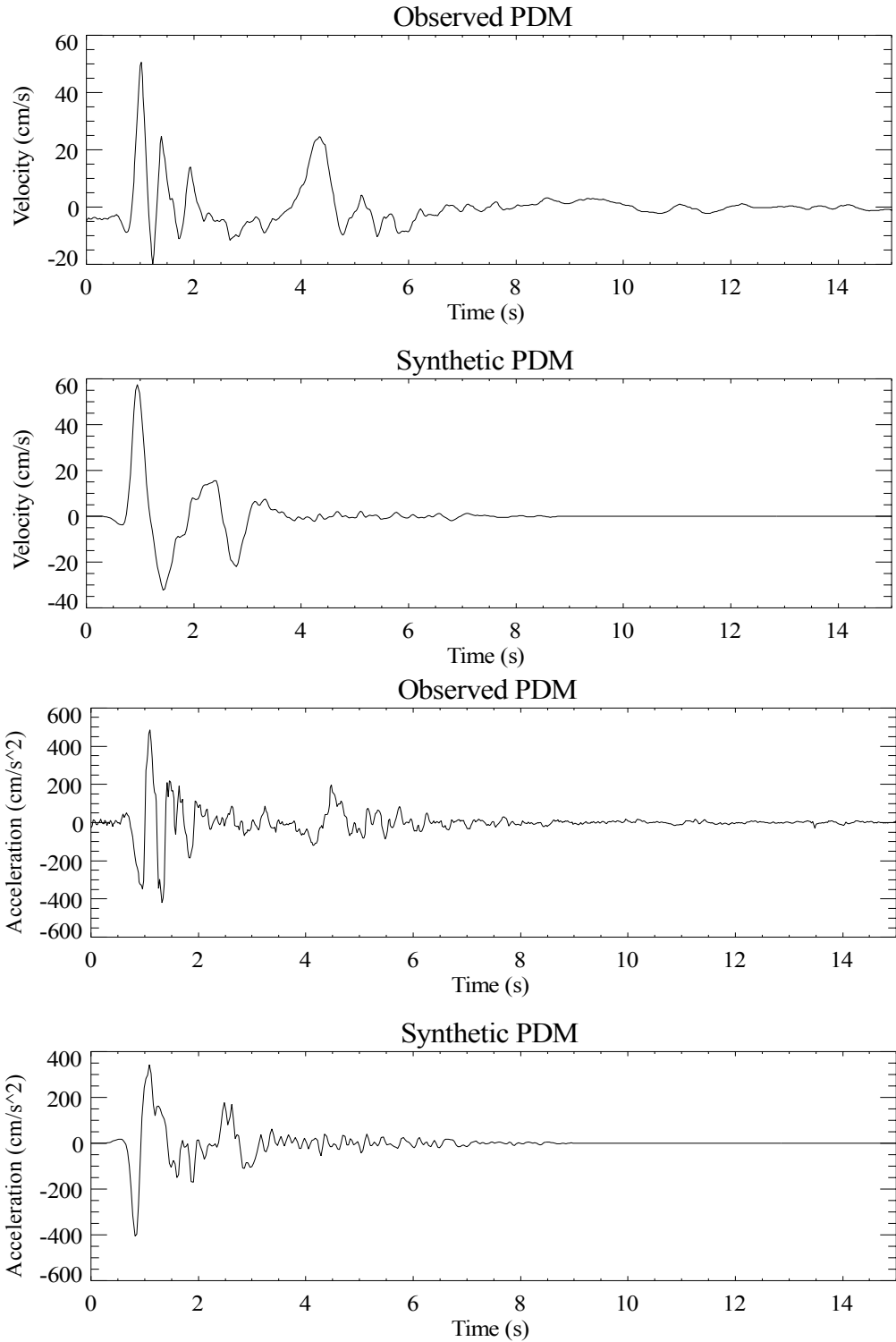


Figure 7-26: Observed and simulated peak horizontal component velocities and accelerations as labeled for station PDM (Pacoima Dam downstream station). Figure 7-11 provides station position.

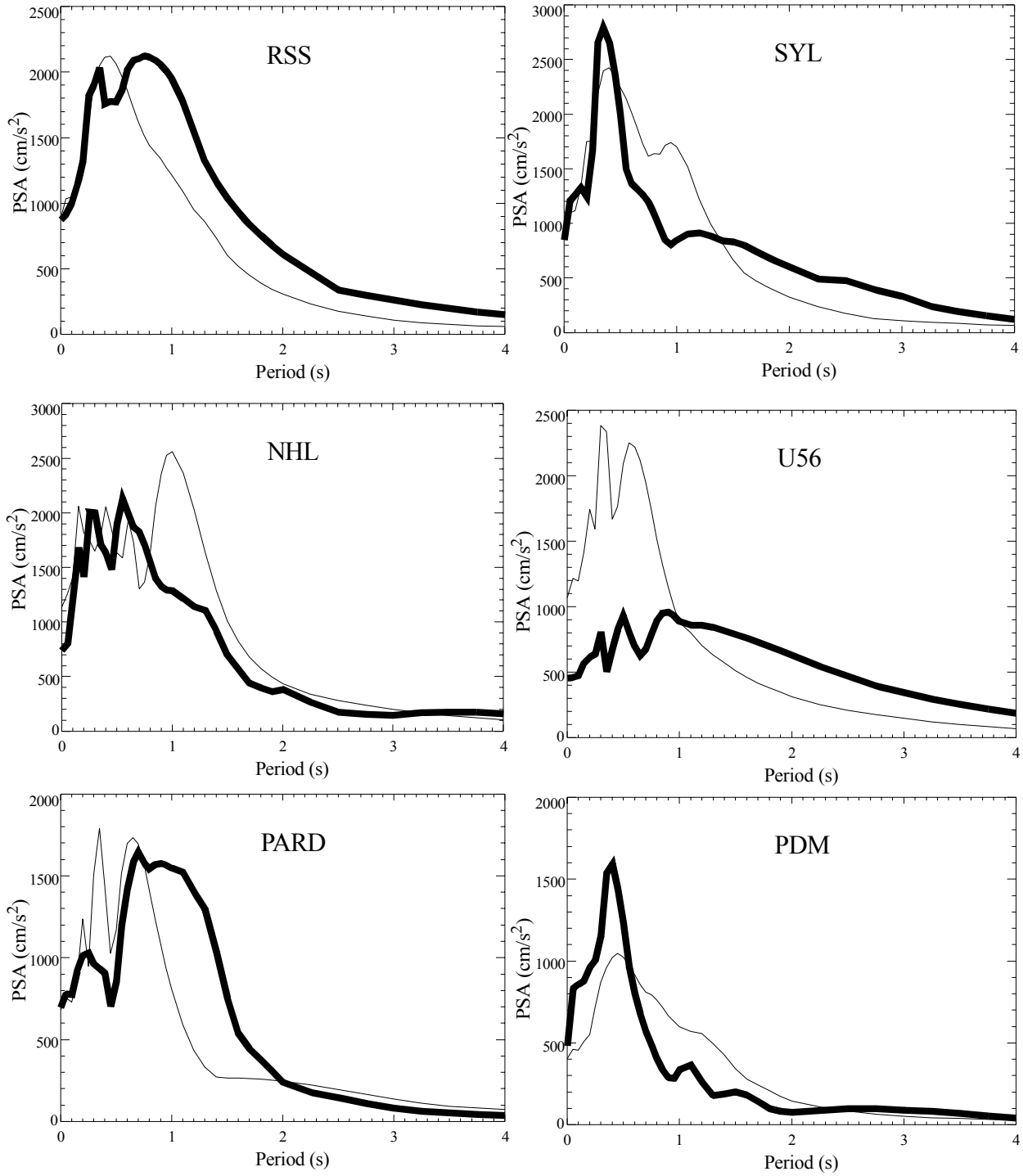


Figure 7-27: Observed and best-fitting Northridge horizontal PSA response spectra. Observed spectra are thick curves and best-fitting synthetic spectra are thin curves. Stations are as labeled.

to total slip, because they include geodetic data, and Hartzell et al. (1996) are more sensitive to slip velocity because they only use strong motion data. Since Hartzell et al. (1996) used an L2 norm their inversion may only weakly constrain rise times because the inversion strongly emphasizes fitting the largest amplitudes. Interestingly, Hartzell et al.'s (1996) inversions for high-frequency radiation intensity are very similar to the slip-velocity patterns in Figure 7-16, with the highest intensities confined to depths > 14 km. Thus, it may be possible that the stochastic Northridge rupture model is compatible with both Wald et al. (1996) and Hartzell et al. (1996). Resolution of these issues would require extensive resolution-trade-off analyses of the various rupture inversion approaches.

The fractional rupture velocities suggest that supershear rupture velocities occurred below 15 km depth over a significant portion of the fault (Figure 7-19). However, a 1D velocity model was used to specify crustal shear-wave velocities in the source model. The 3D shear-wave velocity model of Haucksson and Haase (1997) shows a strong velocity change between the footwall and hangingwall of the Northridge fault between 15 and 20 km depth, with footwall velocities $\sim 20\%$ higher than hangingwall velocities. Fault rupture propagating at about 85% of the local footwall shear-wave velocities below 15 km depth would appear as slightly supershear rupture relative to the 1D reference shear-wave velocity model. Consequently, the apparently large fractional rupture velocities in Figure 7-19 most likely represent rupture velocities of 80-90% of local 3D shear-wave velocities from Haucksson and Haase (1997). Using a hybrid global search inversion Hartzell et al. (1996) obtain a similar pattern of rupture velocities as Figure 7-19.

The kinematic rupture model produces a broad range of ground motions as illustrated by the quantile plots for the acceleration response spectra at the six stations (Figure 7-28). The rupture model is clearly capable of produce ground motions larger and smaller than observed during the Northridge earthquake. The Northridge simulations produced PSA natural logarithm variability of ~ 0.6 , consistent with existing ground motion relations (Abrahamson and Silva, 1997; Sadigh et al., 1997; Spudich et al., 1999). For instance, the synthetic model suggests that the Rinaldi (RSS) ground motions correspond to 84% quantiles for the Northridge rupture geometry and that most of the observed near-fault ground motions represent near-median expectations based on the simulations. Thus, the stochastic kinematic rupture model produce ground motions consistent

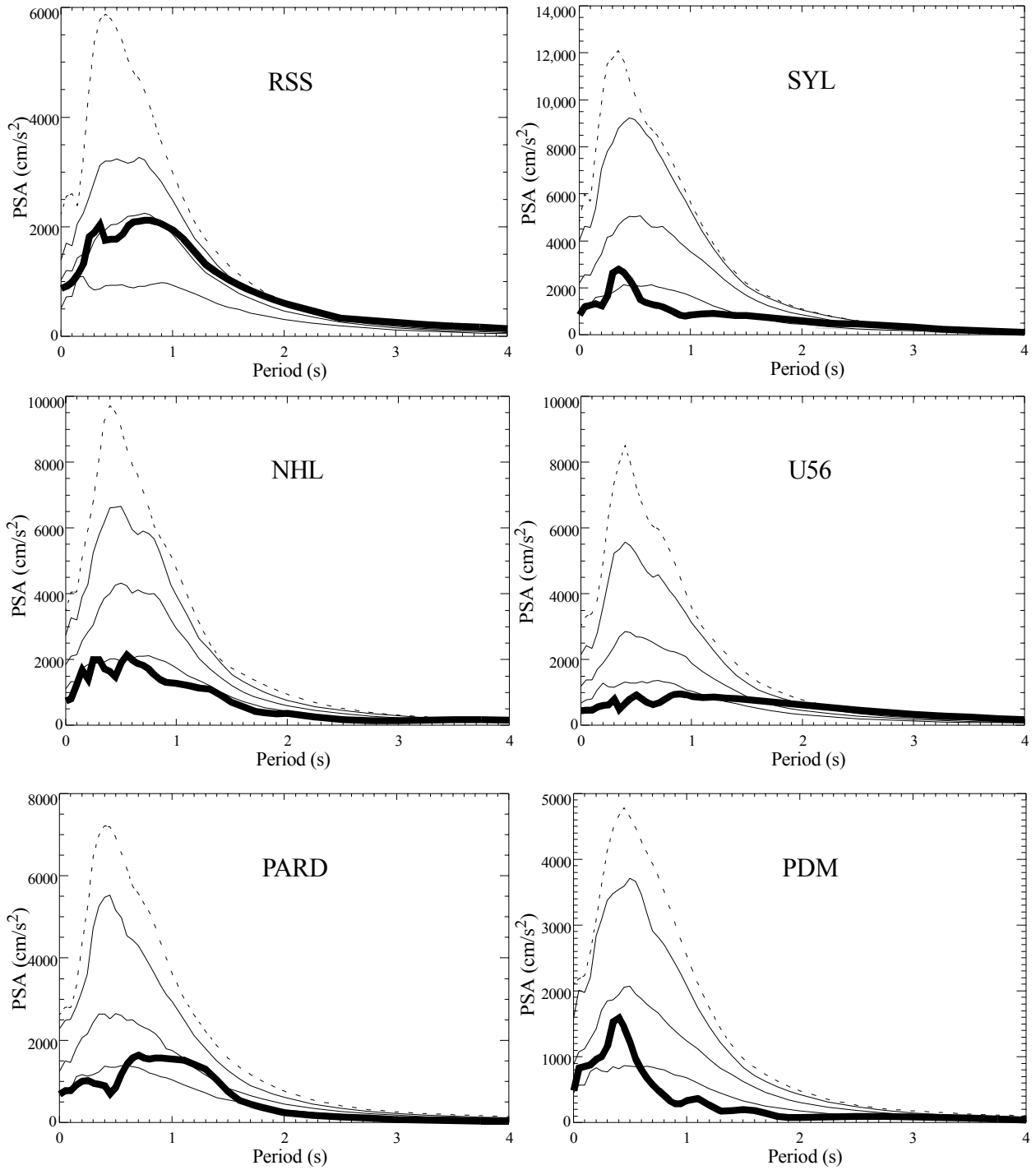


Figure 7-28: Statistical synthetic PSA results. Observed Northridge horizontal PSA response spectra are thick curves, synthetic PSA response spectra quantiles are thin curves, and the envelopes of the maximum amplitudes are dashed curves for stations as labeled. The quantiles from lowest to highest are 0.5, 0.84, and 0.975.

with statistical expectations. Some stochastically-generated kinematic rupture models may be physically unrealizable (see Oglesby and Day, 2002) but this is a problem common to all kinematic rupture models. The waveform-fitting and PSA spectral performance tests indicate that the stochastic kinematic rupture model used to estimate ground motions in Section 6 performs as well or better than other published kinematic rupture models (Silva and Lee, 1987; Somerville et al., 1991; Schneider et al., 1993; Heaton et al., 1995; Jarpe and Kasameyer, 1996; Zeng et al., 1994; Beresnev and Atkinson, 1997; Zeng and Anderson, 2000) for predicting realistic near-source ground motions. The only differences between the Northridge rupture models and the Teton fault rupture models, besides obvious differences in fault geometry, were that no regions of very low rupture velocity ($< 0.6 \cdot V_s$) were used for the Teton fault rupture simulations and correlation lengths for effective stresses and other fault parameters were increased 33% to account for the differences in magnitude between Northridge ($M 6.7$) and the northern Teton fault segment ($M 7.1$), an approach consistent with the findings of Somerville et al. (1999). Confirmation that the synthetic ground modeling approach used in Section 6 can reproduce near-source ground motions from Northridge provides a justification to use the approach to consider other dip-slip earthquake rupture geometries, including modeling ground motions associated with normal-slip earthquakes on the Teton fault.

7.3 Alternative Ground Motion Synthesis Approach of Frankel (1995)

Frankel (1995) developed a ground motion synthesis approach that is relatively simple, consistent with fundamental constraints on earthquake source properties, and reproduced near-fault ground motions from the 1989 $M 7.0$ Loma Prieta earthquake using aftershocks as empirical Green's functions (EGF), an approach pioneered by Hartzell (1978). The information necessary to synthesize ground motions are the moments of the mainshock and the EGF earthquake, the focal mechanism and corner frequency of the EGF earthquake, the distance of the EGF earthquake from the site, the geometry of the mainshock fault surface, fault rupture times, shear-wave travel times from the fault to the site, and a model for the spatial variability of stress drop on the mainshock fault surface. Compared to the source model presented in Section 7.2, Frankel's (1995) approach is much simpler; it does not require explicit specification of parameters such as slip, slip velocity, or rise time.

Let M_{0main} be the moment of the mainshock, M_{0small} be the moment of the EGF earthquake, and A_{main} be the fault area of the mainshock. Frankel's (1995) ground motion synthesis approach consists of the following steps:

1. Calculate the empirical Green's function fault area using the ratio of the EGF moment to the target mainshock moment in a manner to preserve constant stress-drop scaling. This is done by dividing the mainshock fault area into square cells (subfaults) with dimensions h by h , where h^2 is the area of the smaller EGF earthquake. The estimate of h is derived from

$$h^2 = \left(\frac{M_{0small}}{M_{0main}} \right)^{2/3} A_{main} \quad (7-6)$$

2. Sum the EGF of subfault patches distributed over the mainshock fault surface with appropriate delays for rupture times and shear-wave propagation times and scaling at each fault EGF patch by the ratio of the local stress drop to the mean EGF stress drop to obtain ground velocity as

$$\dot{u}(\mathbf{X}, t) = \sum_{i=1}^N \left(\frac{R_0}{R_i} \right) \left(\frac{\Delta\sigma_i}{\Delta\sigma_{small}} \right) g(t - t_{si} - t_{ri}) \quad (7-7)$$

where $g(t)$ is the EGF velocity seismogram at the receiver site, \mathbf{X} , N is the number of square cells on the mainshock fault, $\Delta\sigma_i$ is the cell stress drop, $\Delta\sigma_{small}$ is the stress drop of the EGF earthquake, t_{si} is the travel-time from the center of the subfault cell to the receiver, calculated using the 3D shear-wave velocity model from Section 4, and t_{ri} is the rupture time calculated using the kinematic rupture model outlined in Sections 6 and 7.2, R_0 is the distance of the EGF recording site from the EGF hypocenter, and R_i is the distance from the EGF recording site from the subfault cell on the mainshock fault.

3. Apply a minimum phase convolution operator to $\dot{u}(t)$ from (7-7) to scale frequencies less than the EGF corner frequency to produce the correct proportion mainshock longer-period energy relative to the EGF earthquake a relative slip-velocity with the spectrum

$$S(f) = C \frac{1 + (f/f_{0small})^2}{1 + (f/f_{0main})^2} \quad (7-8)$$

where f is frequency, f_{0small} is the corner frequency of the EGF earthquake, and f_{0main} is the corner frequency of the mainshock. The term C is chosen so that the total moment of the summed subevents is the same as the mainshock moment using

$$C = \frac{M_{0main}}{\sum_{i=1}^N \frac{\Delta\sigma_i}{\Delta\sigma_{small}} M_{0small}} \quad (7-9)$$

where f_{0main} is determined to produce a unity spectrum for frequencies greater than the small earthquake f_{0small} using

$$f_{0main} = \frac{f_{0small}}{\sqrt{C}} \quad (7-10)$$

Frankel (1995) notes that f_{0main} is proportional to $(M_{0small})^{-1/6}$. While this is an undesirable feature of Frankel's approach, since the corner frequency of the mainshock will depend on the moment of the EGF earthquake, it is not a practical concern for Jackson Lake ground motions for periods < 6 s.

The spectral factorization method of Claerbout (1976) is used to find the minimum phase operator with the spectrum from (7-8). This produces a relative slip-velocity function that starts with a delta function (Figure 7-29) to preserve high-frequency response followed by a long-period pulse to increase energy at frequencies less than the EGF corner frequency. The function in Figure 7-29 is not the slip-velocity function of the mainshock, but is essentially the mainshock slip-velocity function deconvolved using the source-time function of the EGF earthquake (Frankel, 1995). The final step is to high-pass filter the estimated ground motions using corner frequencies dictated by the signal-to-noise characteristics of the EGF earthquake recordings. Specific filter corner frequencies are listed in subsequent sections for each EGF earthquake considered.

Andrews (1980) and Frankel (1991) showed that correlated-random spatial stress drop variations on faults are necessary to reproduce ground motion characteristics, particularly the squared

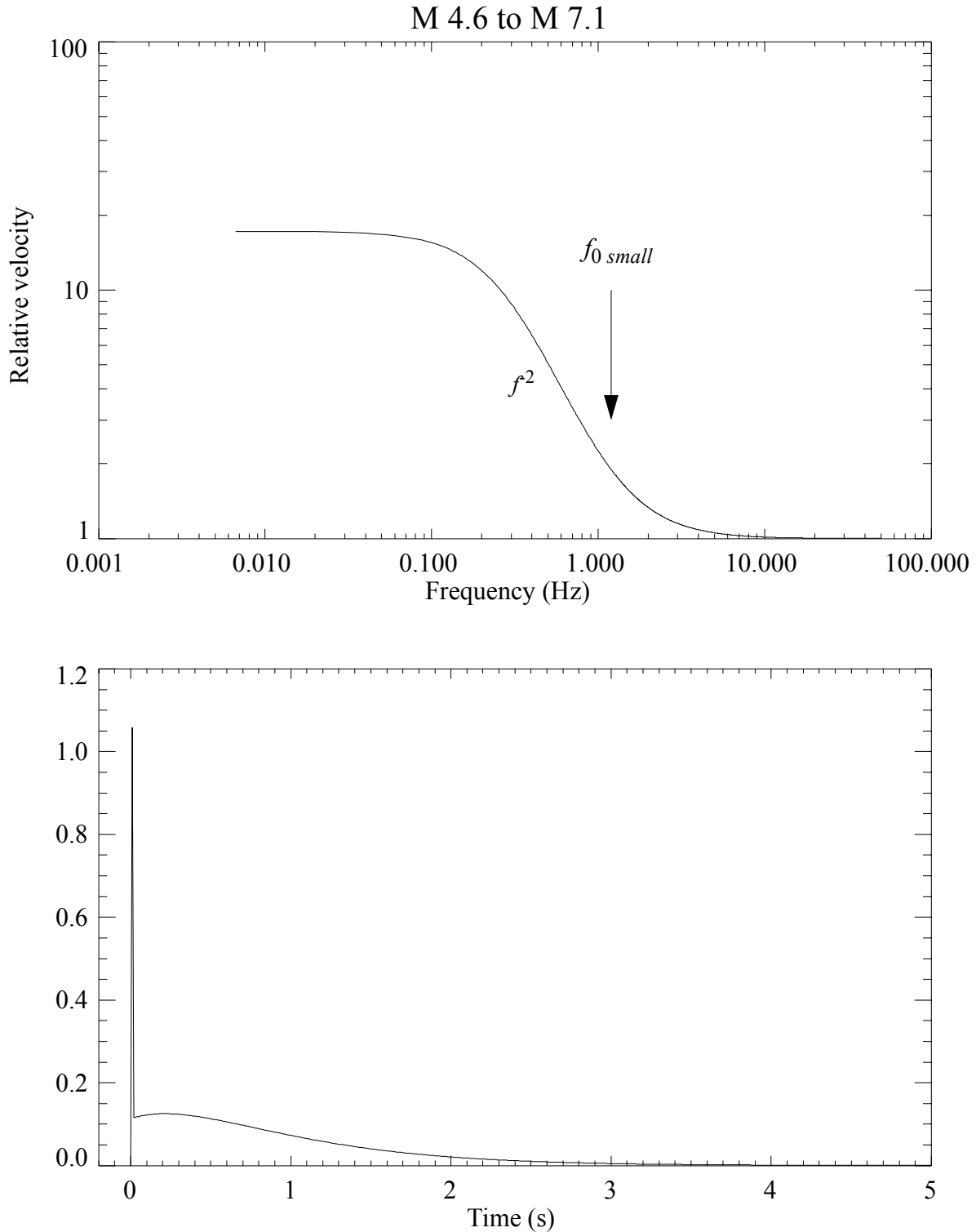


Figure 7-29: Example of relative slip-velocity function. (a) is the Fourier spectrum of the relative slip-velocity function for converting a **M** 4.6 EGF to a **M** 7.1 mainshock. The corner frequency ($f_{0\ small}$) of the **M** 4.6 EGF is denoted by the arrow. (b) Minimum phase relative slip-velocity function corresponding to the spectrum in (a).

frequency spectral decay of ground displacement amplitudes with increasing frequency for frequencies greater than a corner frequency which is inversely proportional to fault rupture dimensions. Estimated ground motions implicitly include EGF effective stresses. If EGF effective stresses are considered representative of mean effective stresses for a region, there is no need to explicitly specify effective stresses. Instead, spatial variability of effective stresses on the fault about the EGF effective stress are specified as indicated in Andrews (1980) and Frankel (1991) using correlation distances that produce dominant asperity dimensions consistent with the asperity size-magnitude relations of Somerville et al. (1999). As shown in Frankel (1995) synthesized ground motions are only modestly dependent on stress drop characteristics. A range of possible rupture velocities (e.g., subshear to supershear as discussed in Ben-Zion, 2002, and O'Connell and Ake, in press) is easily incorporated into rupture time estimates. In all Jackson Lake Dam ground motion simulations in this report, correlated-random Gaussian variations of rupture velocities are constrained to values between $0.6*V_s(z)$ and $1.1*V_s(z)$ with a mean value of $0.85*V_s(z)$, where $V_s(z)$ represents variations in shear-wave velocity with depth. This wide range of rupture velocities provides a rough way to account for modest three-dimensional velocity variations in the crust relative to the 1D shear-velocity model used to calculate rupture times and stopping times on the fault. For instance, a rupture velocity of $1.0*V_s(z)$ would correspond to a rupture velocity of $0.91*V_s(x,y,z)$ at a point in the 3D velocity model where $V_s(x,y,z)$ is 10% faster than $V_s(z)$. This is one way to incorporate Gaussian variations of crustal shear-wave velocities in the kinematic component of the finite-fault source model.

Another appeal of Frankel's (1995) approach is that it requires relatively few parameters that are generally well constrained to specify the influence of wave propagation between the source and the site. For instance, use of empirical Green's functions reduces wave propagation assumptions to the point that the only parameters are the distance of the empirical Green's function from the site and the distances of the discrete fault sub-elements from the site. For this study, broadband recordings at site JLDW of several larger ($M \sim 5$) regional earthquakes and of two $M \sim 3$ earthquakes in the vicinity of the northern Teton fault segment provide empirical Green's functions necessary to estimate ground motions in the 0.2 Hz to 10 Hz frequency band.

Frankel (1995) does not apply a radiation pattern correction to synthesize ground motions. The approach used here is similar. The only portion of the radiation pattern that is accounted for in applications of Frankel's method is the application of shear-wave polarities at each EGF patch on the fault as calculated from the 3D RGF's in Section 6. There was no attempt to calculate the amplitude variation of shear-wave radiation with azimuth and take-off angle. In contrast, in Section 6, the RGF estimates of shear-wave amplitudes in the 0.5-1.5 Hz frequency band for dip-slip faulting were used to scale the EGF amplitudes at each point-source integration point. As summarized in Frankel (1995), a philosophical difficulty of fully employing the shear-wave radiation pattern to the EGF is that scaling of phases following the initial shear-wave may be inappropriate, and at some frequency between 1-10 Hz, the radiation pattern is likely to become statistically insignificant. Since most existing ground motion synthesis methods do not incorporate radiation patterns (Silva and Lee, 1987; Somerville et al., 1991; Schneider et al., 1993; Zeng et al., 1994; Beresnev and Atkinson, 1997; Zeng and Anderson, 2000) using Frankel's approach provides a nice basis for comparison and contrast with the results from Section 6.

7.4 Ground Motions From Larger Regional Earthquakes

Broadband site recordings of $M \sim 4-5$ EGF earthquakes on the Teton fault would represent ideal EGF's for the purposes of synthesizing ground motions at Jackson Lake Dam because large S/N ratios would be available in the 0.1 to 10 Hz frequency band of engineering interest. Such data does not exist. However, several regional earthquakes within 150 km of Jackson Lake Dam were recorded at sites JLDW and JLD3 which have adequate signal-to-noise (S/N) ratios to serve as EGF's for synthesizing ground motions in the 0.1-0.2 Hz to 5-10 Hz frequency band. The two best regional earthquakes are a M 5.2 earthquake in Idaho about 120 km from site JLDW and a M 4.6 earthquake near Yellowstone about 100 km from site JLDW (Table 7-1).

Table 7-1: Regional EGF Earthquake Locations

Date/Time (day mon yr hr:min:s)	Latitude (degrees)	Longitude (degrees)	Stress drop (MPa)	Depth (km)	M	Moment (dyne-cm)
21 Apr. 2001 17:18:57	42.925	-111.395	2.7	16.0	5.2	$6.4 \cdot 10^{23}$
24 Nov. 2000 04:20:06	44.750	-111.690	3.1	4.6	4.6	$8.9 \cdot 10^{22}$

The best S/N ratios are obtained for the **M** 5.2 earthquake that occurred on 21 April 2001 in southeastern Idaho, about 120 km from site JLDW (Figure 7-30). The 211° azimuth from JLDW to the epicenter makes this earthquake a rough analog for seismic energy emitted from the southwestern corner of the northern segment of the Teton fault. The advantages of this earthquake are that surface wave responses are minimized by the position of the Teton Range between the site and the epicenter and the horst and graben structure along the western portion of the travel path to the dam site, the relatively low attenuation of the lower-crustal refracted initial shear-wave arrival, the incidence of the shear-wave through the Teton fault surface toward the site, the normal-faulting mechanism and moment estimate (USGS, PDE, Harvard CMT), the > 15 s delay between the arrival of the initial shear-wave energy and the likely arrival of surface waves, and the site and basin scaling and duration effects are implicitly contained in the site recordings. The obvious disadvantages are that the earthquake is located more than 8 times distant from the site relative to the mean distance of JLDW from the northern segment of the Teton fault (122 km epicentral distance versus ~15 km mean distance from the northern segment of the Teton fault) and surface waves attenuate more slowly than shear waves, so simple distance scaling will overemphasize whole-path surface-wave amplitudes. Conversely, basin-edge waves including basin-edge surface waves will be appropriately scaled as they are directly produced by incidence shear-waves that are appropriately scaled by distance ratios. Since no broadband stations were installed outside the low-velocity basin, clear identification of whole-path surface waves is not possible. Table 7-1 provides PDE location information and Table 7-2 shows the focal mechanism estimated from organization sources as indicated. The PDE source estimate were used because they were

Table 7-2: 21 April 2001 EGF Focal Mechanism Nodal Plane Estimates

Solution	strike	dip	rake
PDE fault plane1:	345	43	-106
PDE fault plane2:	186	49	-76
Harvard fault plane1:	11	43	-77
Harvard fault plane2:	173	48	-102
FAST NEIC fault plane1:	32	41	-75
FAST NEIC fault plane2:	193	50	-103

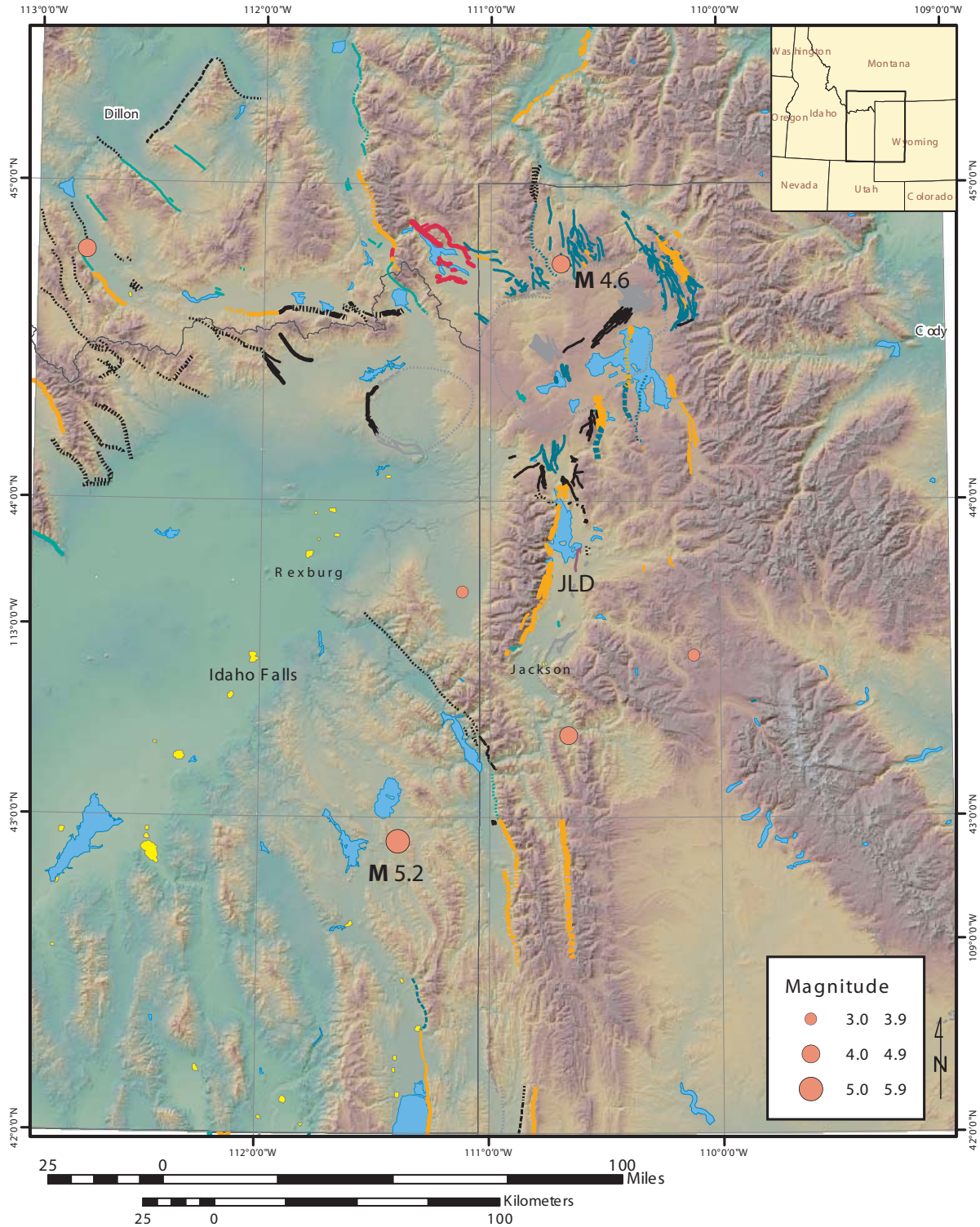


Figure 7-30: Map showing the location of the regional EGF earthquakes relative to the dam. The Idaho earthquake is the red circle labeled **M 5.2** and the Yellowstone earthquake is the red circle labeled **M 4.6**. The Idaho and Teton Ranges are located between the **M 5.2** epicenter and the dam (JLD). Map is colored in relation to topography. Black lines are Quaternary faults, orange lines are late Pleistocene faults, and red lines are faults associated with historical large earthquakes.

the only estimates available for both earthquakes. Harvard moment tensor estimates were also available for the 21 April 2001 earthquake which had moment estimates about 60% larger than the PDE estimates. Since the PDE estimates used more regional stations than Harvard, the PDE estimates were given preference. Although the PDE indicated the availability of a focal mechanism for the **M** 4.6 24 Nov. 2000 Yellowstone earthquake in the monthly listings, no focal mechanism information was found in the monthly listings.

For the **M** 5.2 21 April 2001 earthquake, the average S_V radiation pattern for the azimuth and take-off angle to station JLDW of 0.2 was found by searching over the range of possible strikes, dips, and rakes indicated in Table 7-2 and take-off angle uncertainties of 10° . The average S_V radiation coefficient at site JLDW for a northern segment Teton fault normal-slip earthquake on a 35-45°-dipping normal fault is 0.44. Consequently, the EGF's for the **M** 5.2 21 April 2001 were scaled by a factor of 2.2 to roughly correspond to expected S_V radiation of the northern Teton fault at site JLDW. The EGF's were corrected for crustal shear-wave attenuation since the EGF earthquakes were located at significantly larger distances than distances of sites JLDW and JLD3 from then northern Teton fault segment. A shear-wave quality factor (q) of 200 and average crustal shear-wave velocity (c) of 3.5 km/s were used to produce the frequency-domain attenuation amplitude correction

$$A(f) = \frac{e^{(-r_{egf}\pi f^{0.5}/(cq))}}{e^{(-r_{main}\pi f^{0.5}/(cq))}} \quad (7-11)$$

where f is frequency, r_{egf} is the distance of the EGF earthquake from the site, and r_{main} is the average distance of the simulated mainshock fault from the site. The frequency-dependence in (7-11) ensures that attenuation is not overestimated for large frequencies, although this is not a serious concern, since the principal objective is to evaluate > 1 s responses at sites JLDW and JLD3 using these regional earthquake EGF's.

The second regional EGF earthquake (**M** 4.6) occurred in the Yellowstone region on 24 November 2000 about 100 km from site JLDW. The advantage of this earthquake is that its nearly due north azimuth demonstrates the strong > 1 s period excitation of the low-velocity basin for seismic energy incident from the north. However, there are several significant caveats concerning

using EGF's from this earthquake. The source depth is relatively shallow (~4.4 km) and the refracted low-crustal shear wave likely traversed one or more partial-melt zones associated with the Yellowstone caldera (Nelson and Smith, 1999). Consequently, shear-waves appear severely attenuated at short periods. No moment tensor inversion estimates are available for this event, so event focal mechanism is not known and event moment uncertainties are probably > a factor of two (+- 0.2 moment magnitude). The USGS PDE body-wave magnitude is 4.6 and the Yellowstone seismic network local magnitude (M_L) estimate is 4.3. The USGS PDE magnitude was used to provide a consistent magnitude reference relative to the **M** 5.2 Idaho earthquake. The delay of whole-path surface waves relative to the initial shear-wave arrival are probably ~10 s. It's not possible to distinguish between whole-path and basin-edge surface waves owing to the lack of broadband recordings at stations outside the low-velocity basin. The simple distance correction will overestimate whole-path surface wave amplitudes, but basin-edge surface amplitudes induced by shear-wave arrivals will be appropriately scaled. Thus, the inability to identify and distinguish the various surface waves due to the lack of a broadband seismographic station adjacent to the low-velocity basin severely limits the quantitative interpretation of estimated ground motions within the low-velocity basin produced using these regional EGF's. Attenuation corrections were applied using (7-11). although these corrections are not adequate to account for the severe shear-wave attenuation likely associated with potential partial-melt zones in the Yellowstone area.

The specification of the source parameters in the Frankel (1995) method was made as simple as possible. For the northern Teton fault segment, a hypocenter between the end of the fault segment and station JLDW, and a receiver at site JLDW, isochrones (sum of rupture and shear-wave travel times) have a hyperbolic distribution with a maximum isochrones time of 15 s. Uniform random numbers totaling the number of subfault cells were generated, squared, and scaled to a maximum of 15 s to produce approximate isochrone estimates for each subfault cell. Stress drop variations were constructed using uniform random variations scaled to ratios < a factor of two about the mean while making the mean stress drop of the mainshock the same as the EGF earthquake. This implicitly sets the stress drop correlation length to the subcell dimensions of the EGF earthquakes (see Table 7-3). This provides a source model specification completely independent of the approach used in Sections 6 and 7.2 to test the sensitivity of estimated ground motions to

kinematic source model specifications. EGF parameters used in the ground motion simulations are shown in Table 7-3. The minimum frequencies were determined by inspection of S/N ratios in

Table 7-3: Regional EGF Earthquake Simulation Parameters

Date/Time (day mon yr hr:min:s)	Min f (Hz)	f_{0small} (Hz)	Stress drop (MPa)	M	Moment (dyne-cm)	Scaling
21 Apr. 2001 17:18:57	0.05	0.6	2.7	5.2	$6.4 \cdot 10^{23}$	2.26
24 Nov. 2000 04:20:06	0.1	1.2	3.1	4.6	$8.9 \cdot 10^{22}$	1.0

the site recordings. Corner frequencies were difficult to impossible to reliably selected from the low-velocity basin recordings, given uncertainties due to various propagation effects including attenuation, amplification, etc. Consequently, while the data provide some support for picking the corner frequency of the **M** 5.2 21 April 2001 EGF earthquake, the corner frequency **M** 4.6 for 24 November 2000 EGF earthquake was assigned to produce a stress drop consistent with mean stress drops for the Basin and Range (see discussion in Ichinose et al, 1997) because the severe attenuation of shear-waves precluded estimating the corner frequency from the JLDW site recordings. Ground motions were simulated using the recordings of both regional EGF earthquakes at rock site JLDW and soil site JLD3.

7.4.1 Rock Site JLDW. Site JLDW velocity seismograms from the **M** 5.2 Idaho, earthquake (Figure 7-31) have remarkably long short-period durations for a rock site. Large peak horizontal velocities (PHV) > 50% of initial shear-wave PHV's persist for > 40 s. Peak vertical velocities are about half the PHV's (Figure 7-31). Since there are no broadband seismographic stations outside the low-velocity basin, it is not possible to clearly identify whole-path surface waves or to ascertain if they are significant contributors to the observed ground motions at site JLDW. The S/N for all three components is adequate to model ground motions to periods extending to 10-20 s and for frequencies < 10 Hz (Figure 7-32). The acceleration response spectra are shown in (Figure 7-33).

The synthetic JLDW vertical response prior to application of (7-8) in Figure 7-34 have the spectral responses for typical soil sites with acceleration response spectra amplitudes nearly

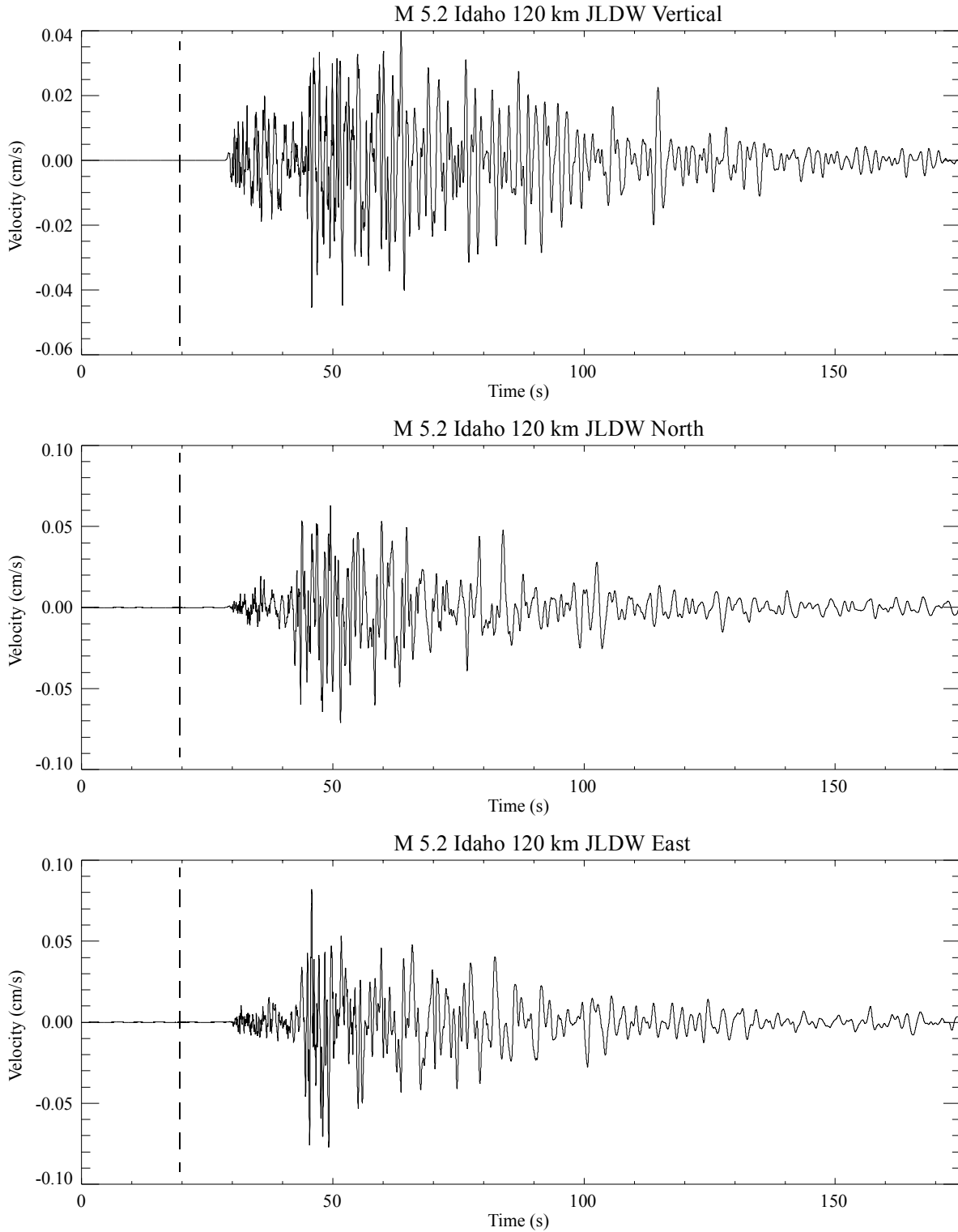


Figure 7-31: Site JLDW velocity seismograms from the 21 Apr. 2001 M 5.2 Idaho earthquake. Components are as labeled. Vertical dashed lines divided the seismograms into pre-event noise and signal portions for spectra shown in Figure 7-32.

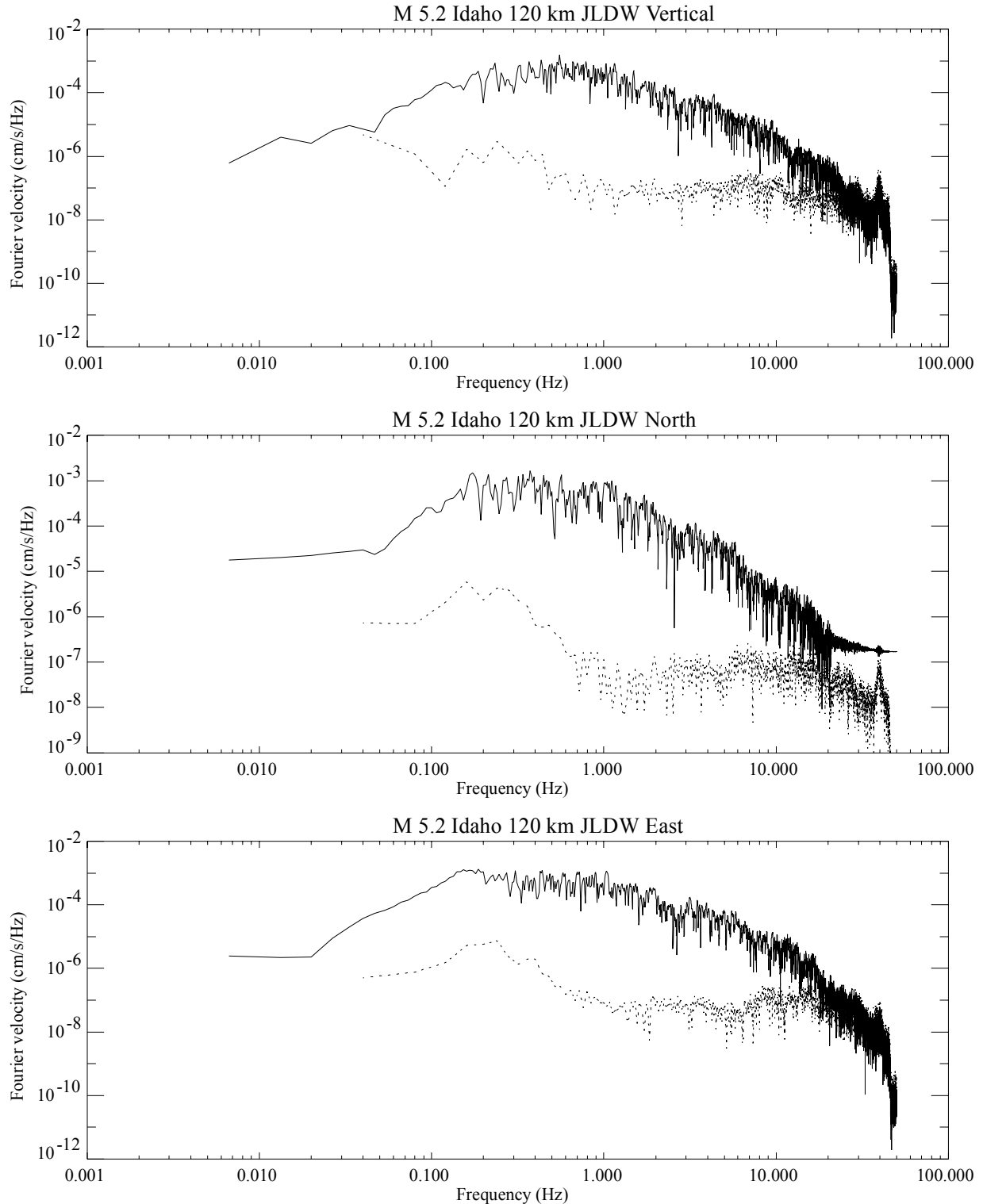


Figure 7-32: Site JLDW Fourier velocity spectra from the 21 Apr. 2001 M 5.2 Idaho earthquake. Components are as labeled. Solid curves are signal spectra and dotted curves are noise spectra using the time windows indicated in Figure 7-31.

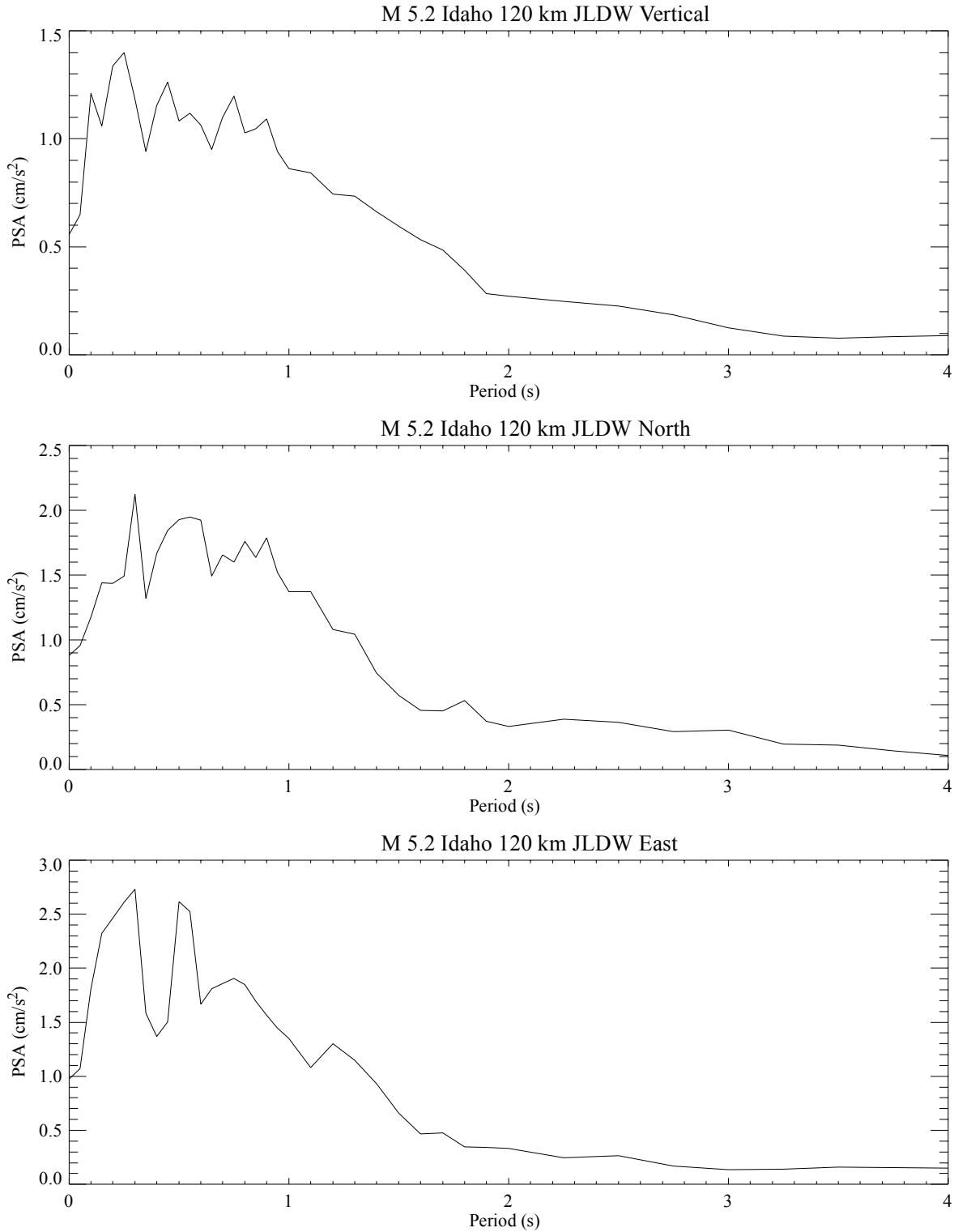


Figure 7-33: Site JLDW acceleration response spectra from the 21 Apr. 2001 M 5.2 Idaho earthquake. Components are as labeled.

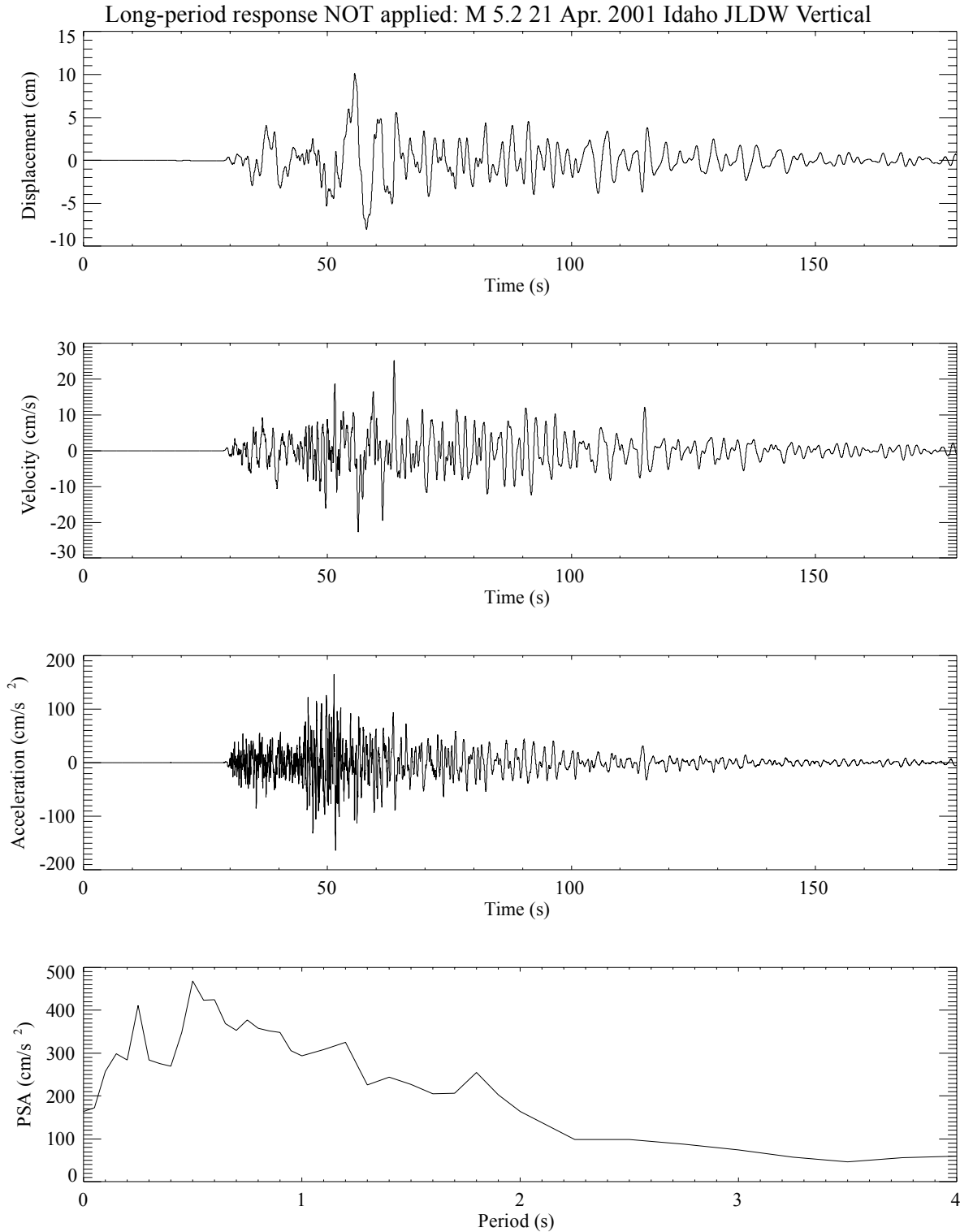


Figure 7-34: Subevent sum **M** 7.1 northern Teton fault earthquake simulation JLDW vertical response before long-period correction. The **M** 5.2 JLDW seismograms from Figure 7-31 were the EGF's used in (7-7). Corresponding complete synthetic vertical responses incorporating (7-8) are shown in Figure 7-35.

monotonically decreasing with increasing period from a peak amplitude at 0.5 s. However, when (7-8) is applied to produce vertical ground motions corresponding to a **M** 7.1 northern Teton fault segment earthquake (Figure 7-35), acceleration response spectral amplitudes begin to increase with period for periods > 3.5 s. This is consistent with the 5-10 s period of the dominant displacement pulse in Figure 7-35, which is also present in Figure 7-34. The timing of the large-displacement pulse within 10 s of the earliest arriving shear-wave is **inconsistent** with the large-displacement pulse being associated with a whole-path surface wave arrival, which should arrive at least 15 s after the initial shear wave, e.g., at times > 60 s. Thus, the large > 3 s synthetic vertical acceleration response at site JLDW in Section 6 appear reasonable because they are produced using purely empirical body-wave site responses (e.g., EGF's) with excellent S/N (Figure 7-32).

The shear-wave attenuation correction over-amplifies the P-wave arrivals at the beginning of the north component (Figure 7-36), particularly when the total amplitude and phases corrections from (7-8) are applied (Figure 7-37). The shear-wave attenuation reverses dispersion which results in overly compressed high-frequency P-wave arrivals. Since the focus here is on responses for periods > 1 s this is not a serious issue. The most remarkable aspect of the north component at rock site JLDW is that peak velocities > 100 cm/s persist for about 40 s and that peak velocities > 50 cm/s span a 60 s time window (Figure 7-37). Peak velocities > 10 cm/s persist for more than 2 minutes. These are long durations for a **M** ~ 7 earthquake close to a rock site. Spectral accelerations remain > 0.5 g for periods extending to 4 s. The north component's long durations and strong long-period acceleration responses are consistent with hypothesis that the low-velocity basin in the hangingwall of the Teton fault efficiently traps energy, amplifying long-period motions, and substantially increasing strong motion durations at even rock sites within the low-velocity basin. The east component exhibits a nearly monochromatic strong ~ 4 -5 s response with peak velocities > 100 cm/s starting with a few seconds of the initial shear-wave arrival at ~ 47 s, even before application of (7-8) (Figure 7-38). The 4-5 s responses are even more pronounced in the complete east synthetic motions (Figure 7-39). The strong excitation of the 4-5 s responses clearly visible in the velocity and displacement seismogram begins within 5 s of the initial shear-wave arrival, which is too early to correspond to whole-path surface wave arrivals in the EGF's. Thus, the increase in acceleration responses for periods > 3 s in Figure 7-39 is associated with real

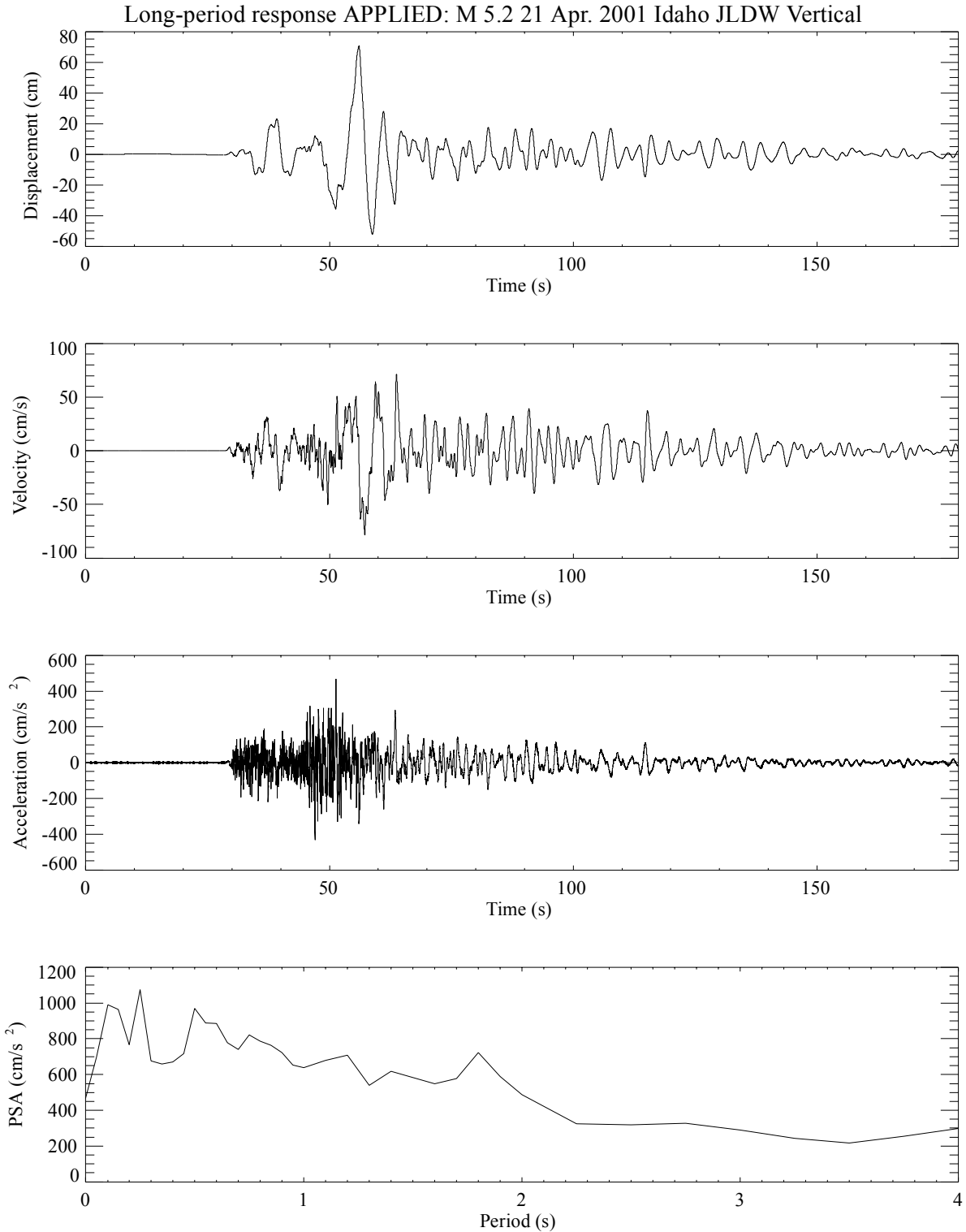


Figure 7-35: **M** 7.1 northern Teton fault earthquake simulation JLDW vertical response. This is the total response obtained by combining the velocity seismograms from Figure 7-34 with (7-8).

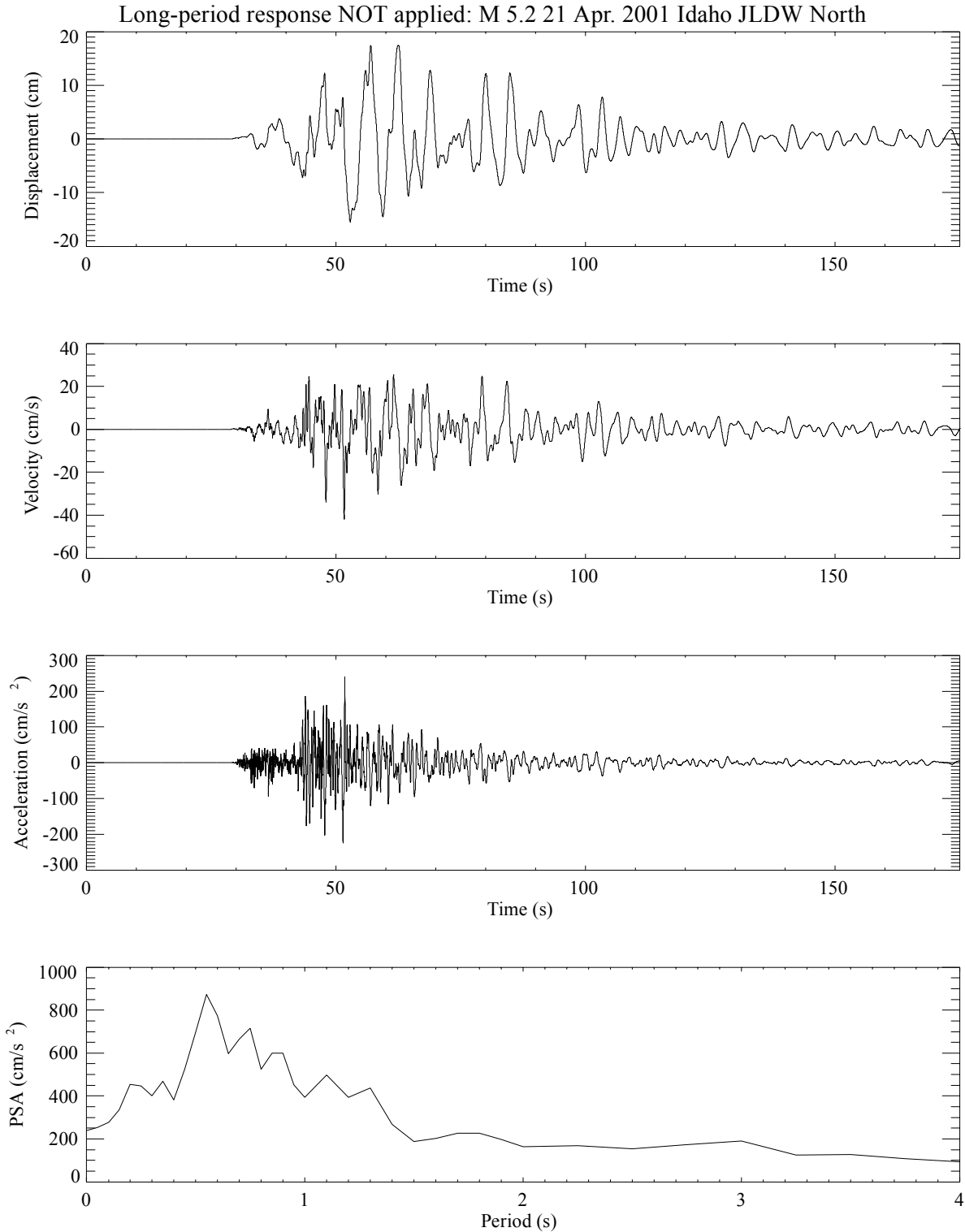


Figure 7-36: Subevent sum **M** 7.1 northern Teton fault earthquake simulation JLDW north response before long-period correction. The **M** 5.2 JLDW seismograms from Figure 7-31 were the EGF's used in (7-7). Corresponding complete synthetic vertical responses incorporating (7-8) are shown in Figure 7-37.

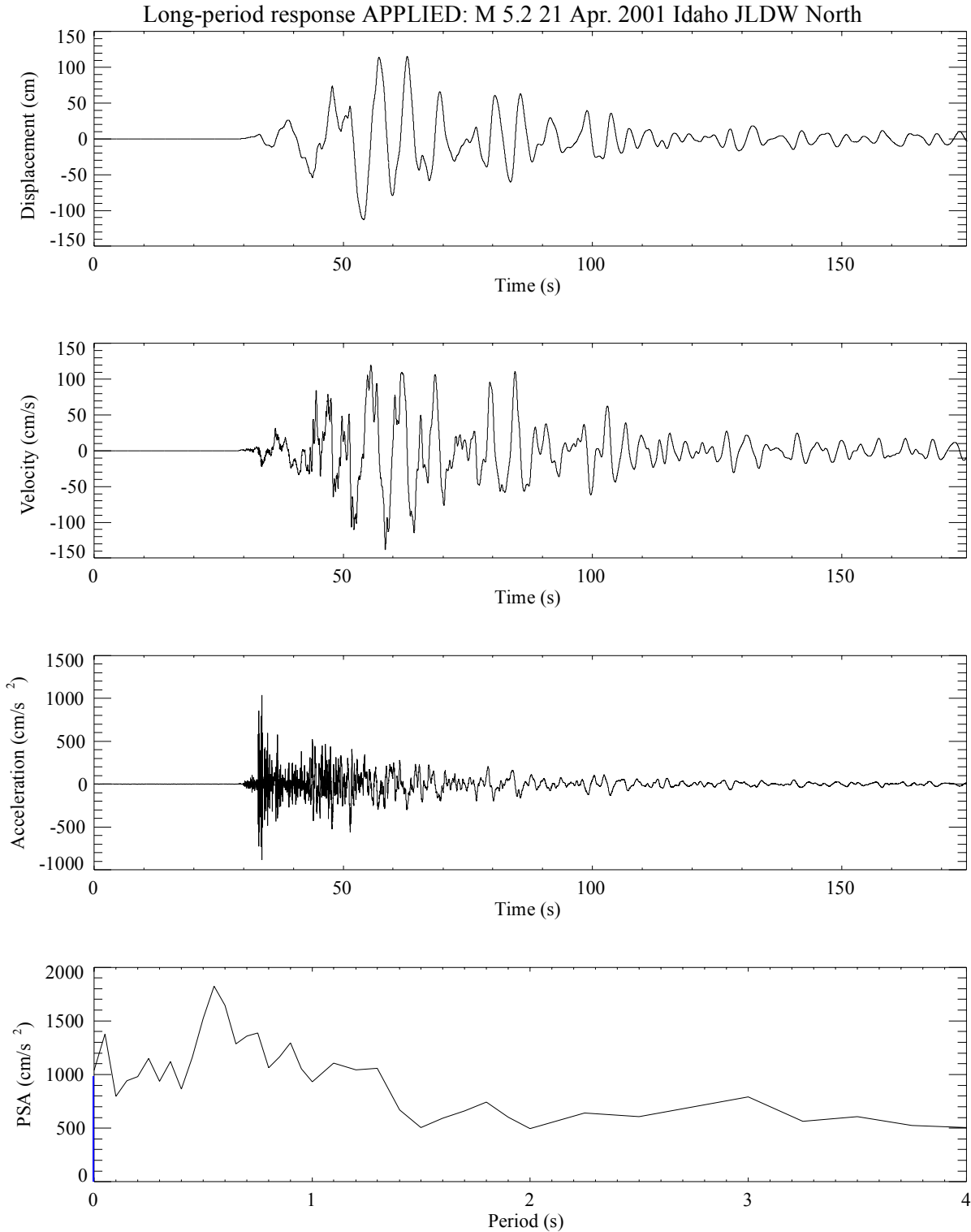


Figure 7-37: **M** 7.1 northern Teton fault earthquake simulation JLDW north response. This is the total response obtained by combining the velocity seismograms from Figure 7-36 with (7-8). Note the largest accelerations are associated with P-wave energy near the beginning of the shaking that reflects overcorrection of the pre-shear-wave energy for whole-path crustal shear-wave attenuation.

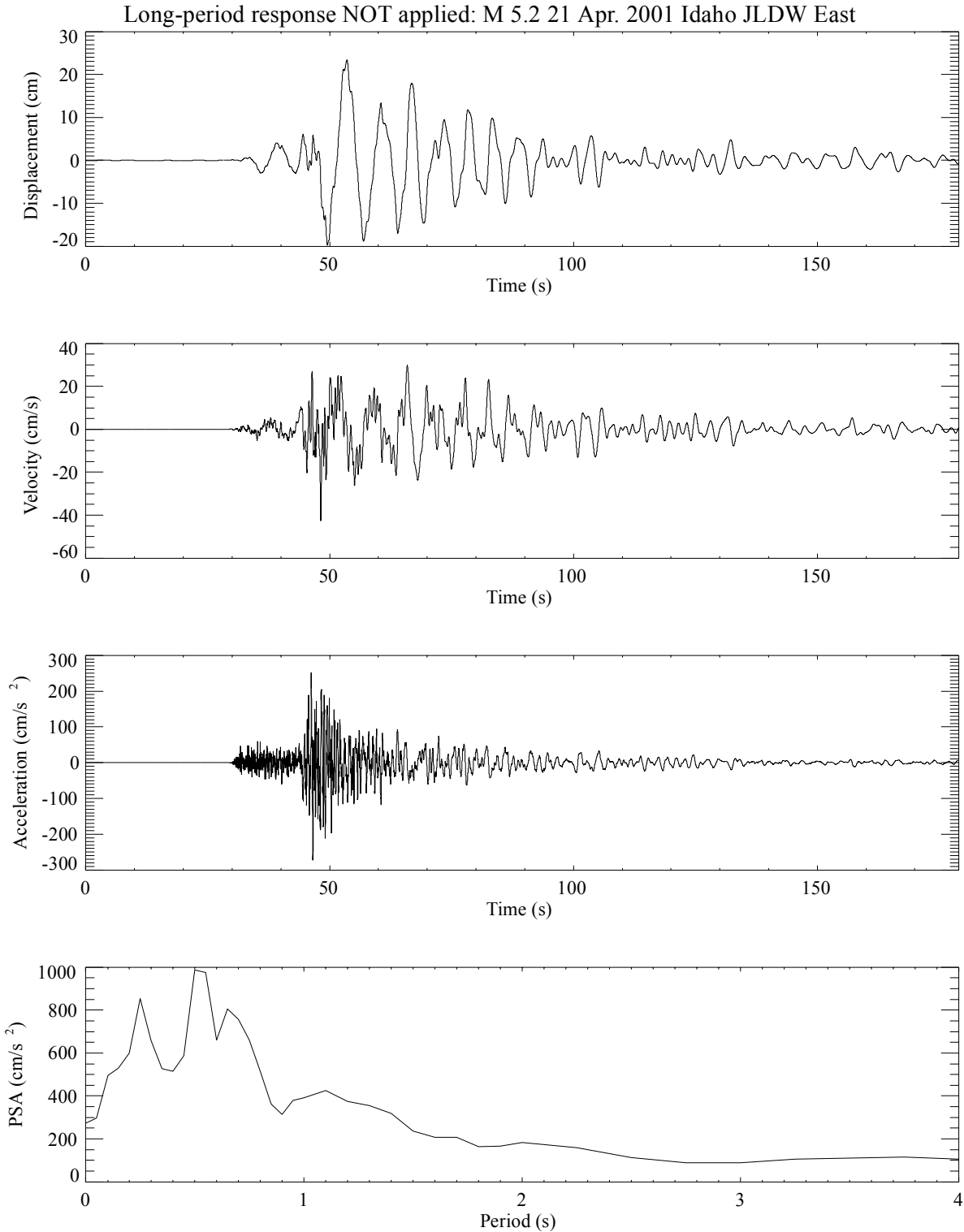


Figure 7-38: Subevent sum **M** 7.1 northern Teton fault earthquake simulation JLDW east response before long-period correction. The **M** 5.2 JLDW seismograms from Figure 7-31 were the EGF's used in (7-7). Corresponding complete synthetic vertical responses incorporating (7-8) are shown in Figure 7-39.

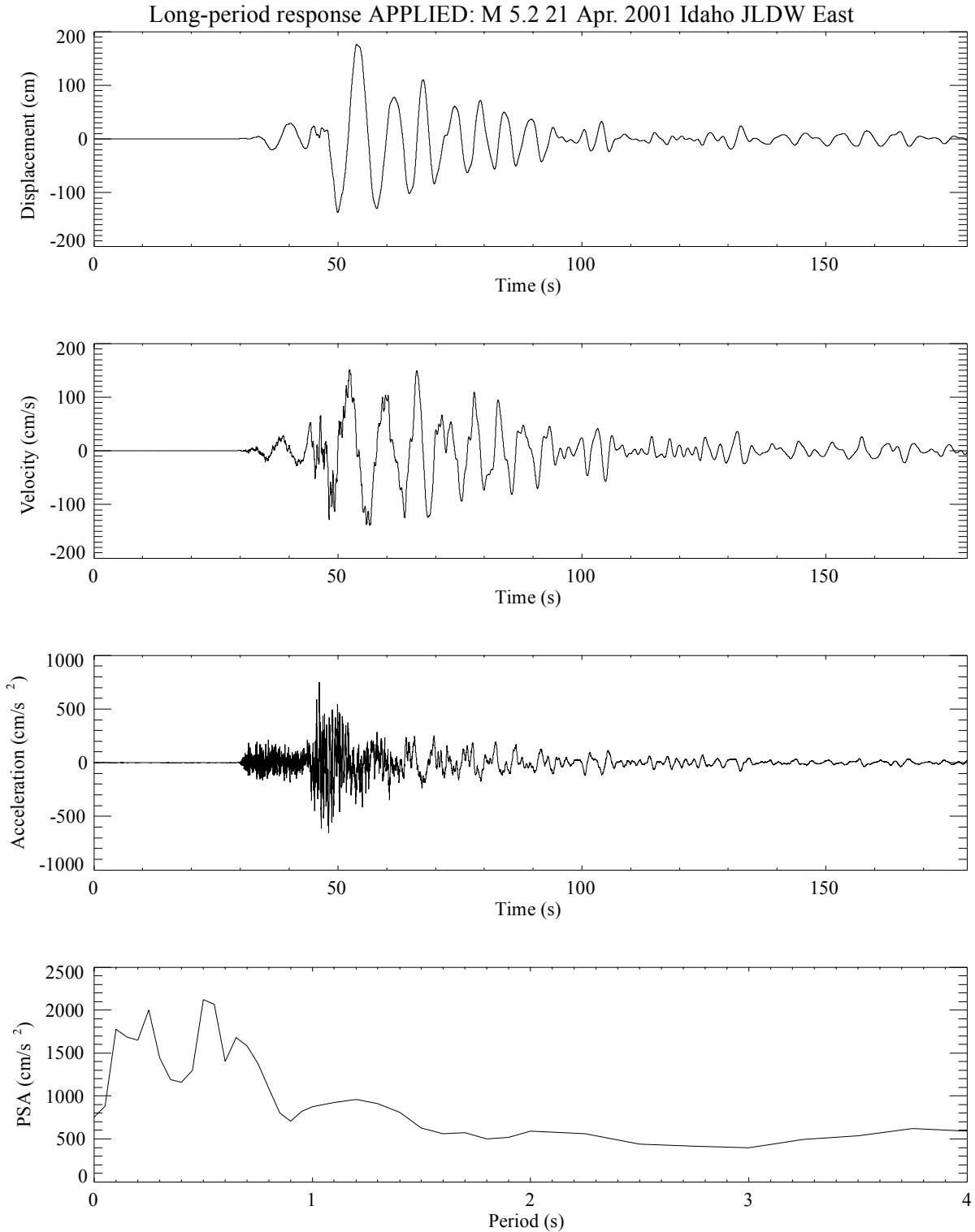


Figure 7-39: **M** 7.1 northern Teton fault earthquake simulation JLDW east response. This is the total response obtained by combining the velocity seismograms from Figure 7-38 with (7-8).

signal because S/N is > 10 for periods < 10 s (Figure 7-32) and suggests that the strong > 3 s synthetic acceleration responses in Section 6 are probably realistic. Conversely, the greater than two-minute-long > 10 cm/s velocity responses in Figures 7-35, 7-37, and 7-39 indicate that the synthetic durations in Section 6 are probably less than half of realistic durations for site JLDW. However, the lack of reference broadband stations adjacent to the low-velocity basin preclude definitive conclusions concerning the basin responses because whole-path surface responses (that could significantly bias impressions of responses within the low-velocity basin) cannot be determined from the basin recordings. To put these rock durations in some perspective, assuming a “normal” duration of about 40 s of coda for a rock site close to a $M \sim 7$ earthquake, a 140 s total duration from results in Figures 3-34 to 3-39, and a rupture velocity of 3 km/s, a duration of 100 s would correspond to a 300-km-long unilateral rupture. The rupture-length relations of Wells and Coppersmith (1994) estimate a magnitude 8 for a rupture length of 300 km. Thus, the effective magnitude at rock site JLDW is about one magnitude higher than the actual earthquake.

The rock site JLDW seismograms from the M 4.6 Yellowstone earthquake are virtually devoid of high-frequency shear-waves (Figure 7-40) in stark contrast to the corresponding seismograms from the M 5.2 Idaho earthquake (Figure 7-31). As discussed earlier, this is consistent with strong shear-wave attenuation associated with partial-melt in the Yellowstone region (Miller and Smith, 1999). Only the east component has adequate S/N to model ground motions to periods extending to 10 s (Figure 7-41), although adequate S/N is available on the vertical and north components to model ground motions to periods extending to 5 s. The minimum periods of adequate S/N are limited to periods > 0.5 s for the horizontal components and periods > 1 s for the vertical component (Figure 7-41). These represent minimally adequate S/N to evaluate long-period ground motions at the site JLDW. The most striking aspect of the seismograms and their acceleration response spectra is the increase of acceleration responses for periods > 2.5 s (Figure 7-42) and the associated long-durations of these long-period motions (> 100 s) at this rock site. It is likely that some of the large-amplitude arrivals in the 50-60 s time window are whole-path surface waves, based on expected surface-wave travel times. However, the persistent reverberations for times substantially later than 60 s are likely the result of waves trapped in the low-velocity basin. This indicates that the basin is more strongly excited by seismic energy approaching from the NNW. Lacking reference broadband stations outside the low-velocity basin

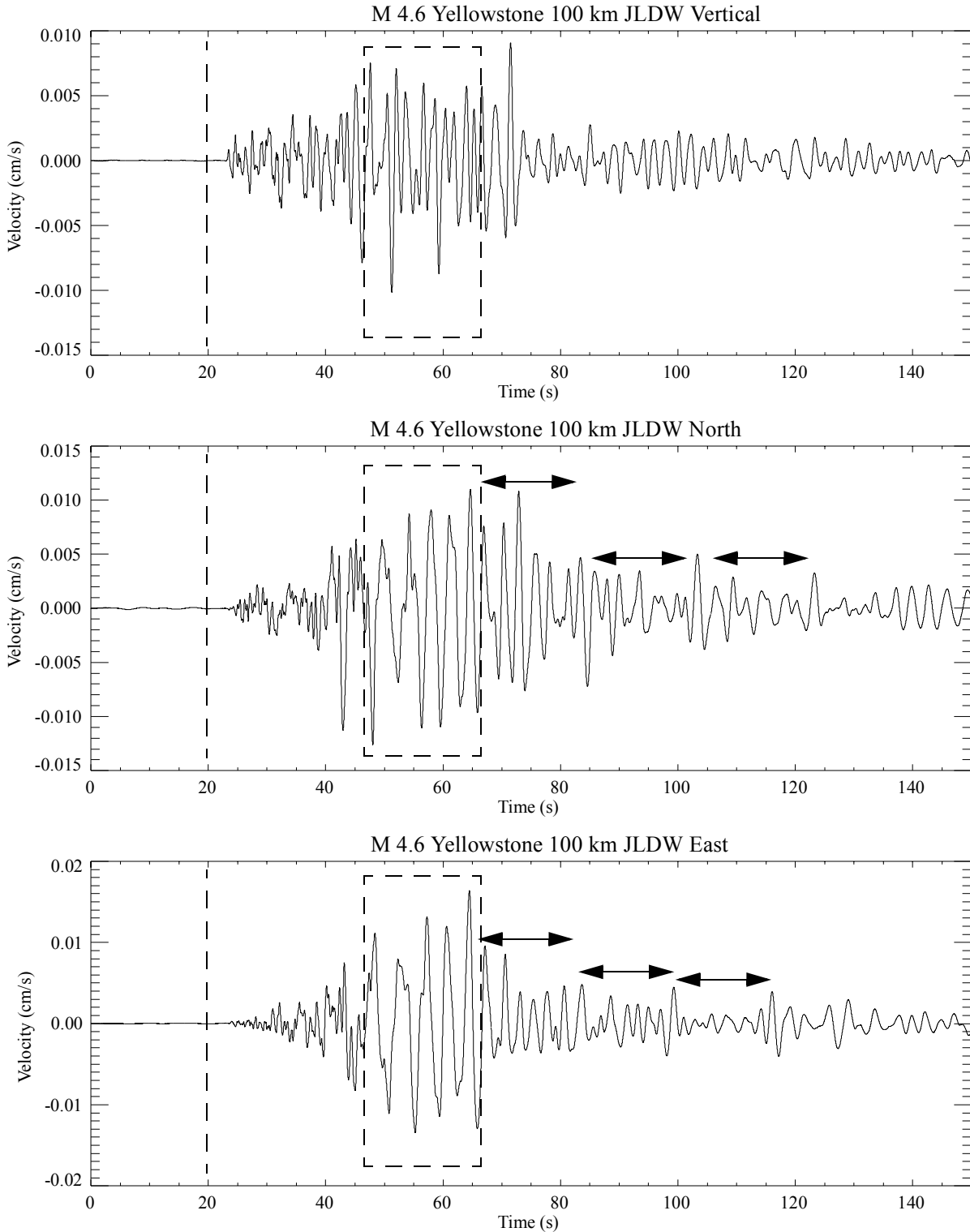


Figure 7-40: Site JLDW velocity seismograms from the 24 Nov. 2000 **M** 4.6 Yellowstone earthquake. Components are as labeled. Vertical dashed lines divide the seismograms into pre-event noise and signal portions for spectra shown in Figure 7-41. Note significant amplitudes persist to the end of the record. The double arrows show ~20 s time intervals between local peak velocities in the coda following the time interval of likely whole-path surface waves, denoted by the dashed-rectangles.

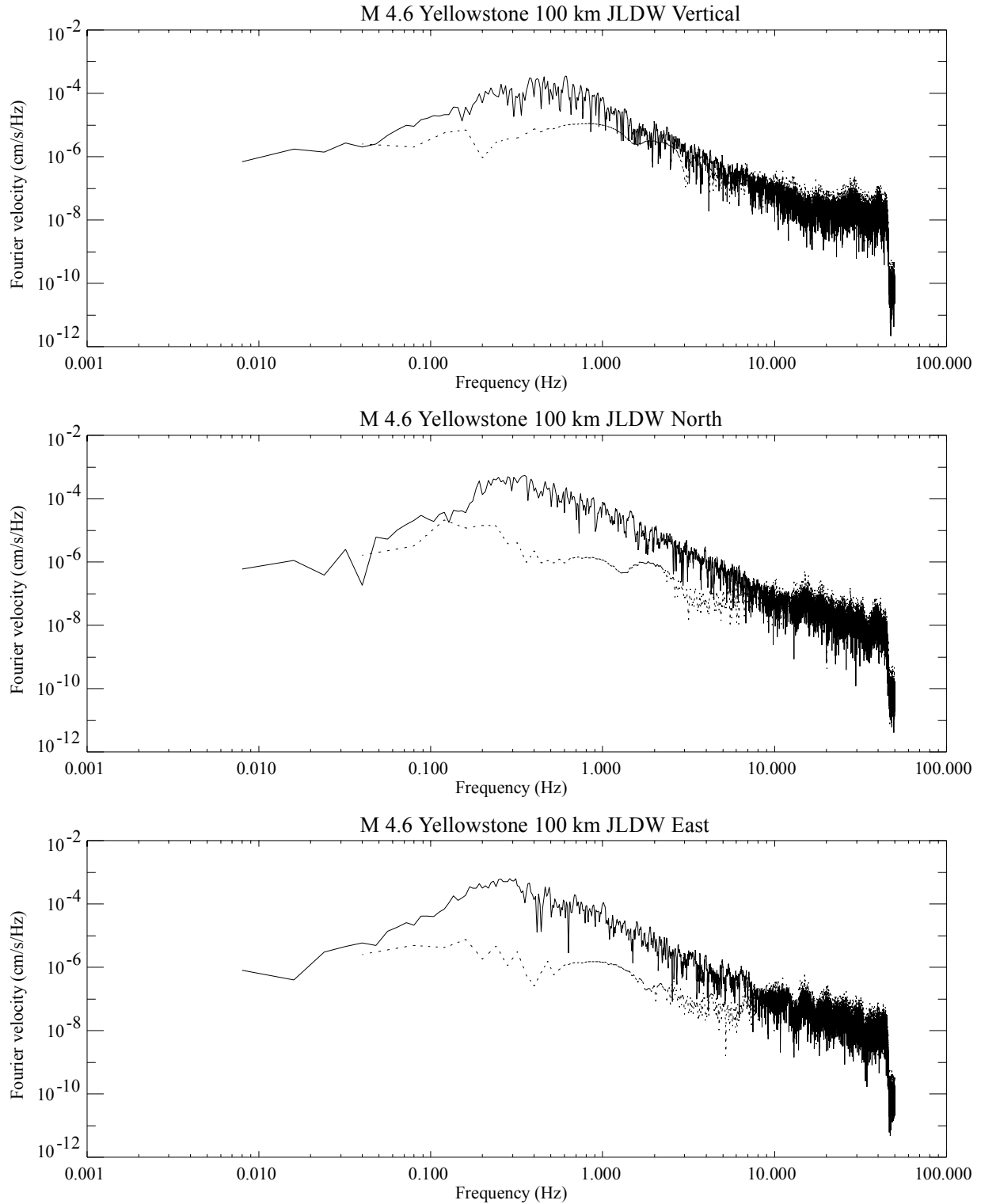


Figure 7-41: Site JLDW Fourier velocity spectra from the 24 Nov. 2000 M 4.6 Yellowstone earthquake. Components are as labeled. Solid curves are signal spectra and dotted curves are noise spectra using the time windows indicated in Figure 7-40.

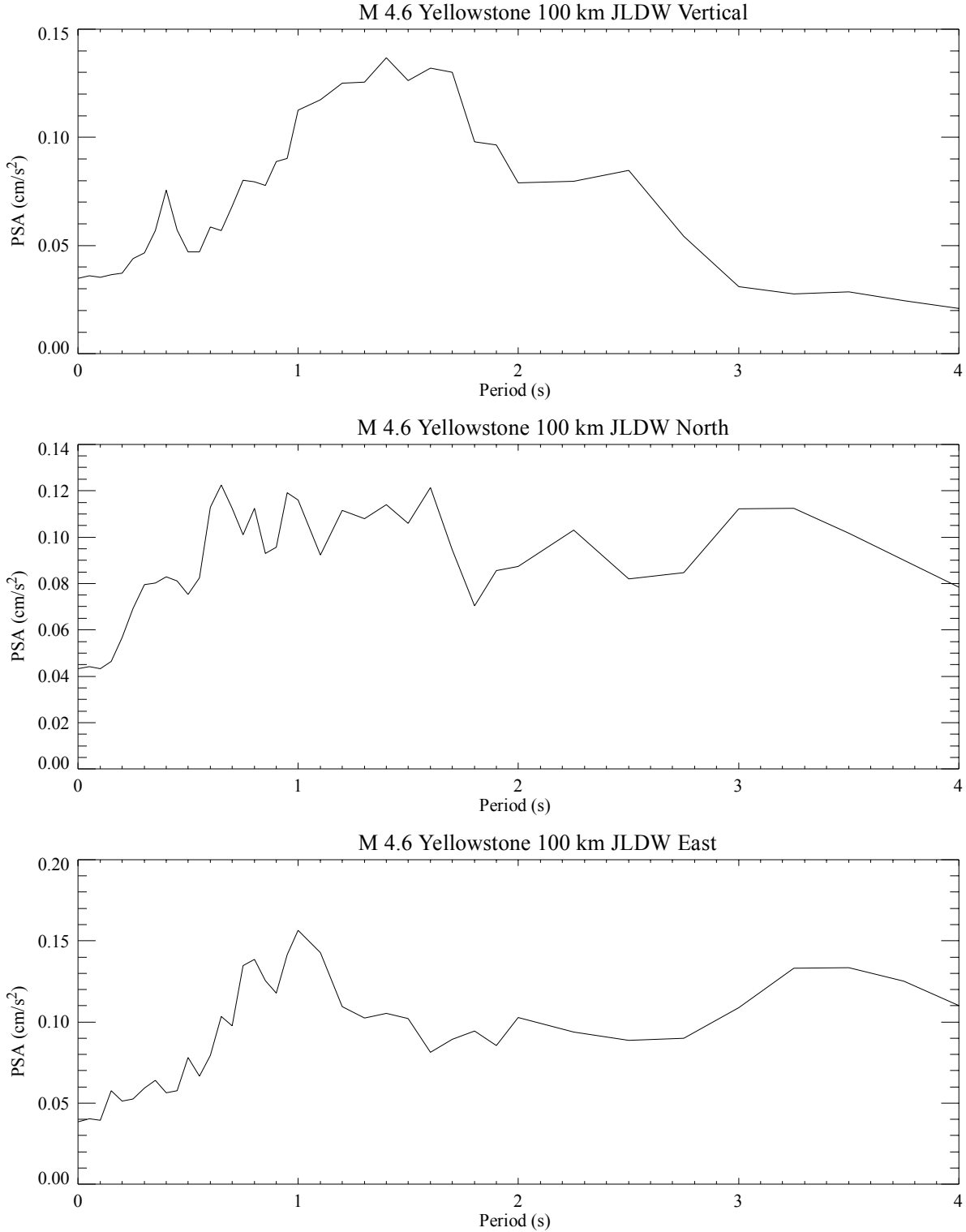


Figure 7-42: Site JLDW acceleration response spectra from the 24 Nov. 2000 M 4.6 Yellowstone earthquake. Components are as labeled.

it is not possible to draw definitive conclusions as to the relative proportions of whole-path and basin-edge induced responses from the JLDW seismograms. There is weak evidence in the horizontal seismograms, particularly the north component, of a ~ 20 s repeating of local peaks in ground velocity (Figure 7-40) which would be consistent with ~ 1 -km/s phase velocities of trapped waves reverberating in the ~ 20 -km-long (north-south extent) low-velocity basin in the 3D velocity model of Sections 4 and 6. The time interval is slightly longer than 20 s for the north component and slightly less than 20 s for the east component which would be consistent with basin-edge-induced Love waves on the east component and basin-edge-induced Rayleigh waves on the north and vertical components and expected surface wave polarizations for energy incident from the NNW. The strong > 2 s horizontal acceleration responses (Figure 7-42) are probably whole-path fundamental-mode surface waves and likely produce the maximum horizontal velocities in Figure 7-40. Thus, long-period acceleration spectra produced using the Yellowstone earthquake as EGF's should be interpreted with caution since body-wave distance-amplitude corrections will overcorrect whole-path surface wave amplitudes for the **M** 4.6 Yellowstone earthquake by as much as a factor of 2.5.

Simulated vertical motions using the Yellowstone earthquake EGF decrease very slowly with increasing time (Figures 7-43 and 7-44). It is likely that some of the largest amplitudes in the 40-60 s time window are associated with exaggerated-amplitude whole-path surface waves. However, it is remarkable that peak amplitudes at 120 s are comparable to peak amplitudes prior to 40 s; neither of these time windows is likely to contain whole-path surface wave energy. The north component has the strongest long-duration responses (Figure 7-45 and 7-46) with a local peak velocity at about 85 s of ~ 50 cm/s that appears to repeat three more times in the record with about 20 s delays between peaks (105 s, 125 s, and 145 s). The peak velocity of each successive peak decreases slowly and is only halved in the third peak at ~ 145 s relative to the peak at ~ 85 s. The acceleration responses for periods > 2 s are probably exaggerated by whole-path surface waves in the 40-60 s time window, but probably not by more than a factor of two since the longer-period basin-edge induced arrivals later than 60 s have amplitudes more than half of the initial shear-waves. The east component (Figures 7-47 and 7-48) shows a weaker pattern of repeated local coda peak amplitudes that have a slightly reduced time separation relative to the north component (Figure 7-48), consistent with the coda of the east component being dominantly

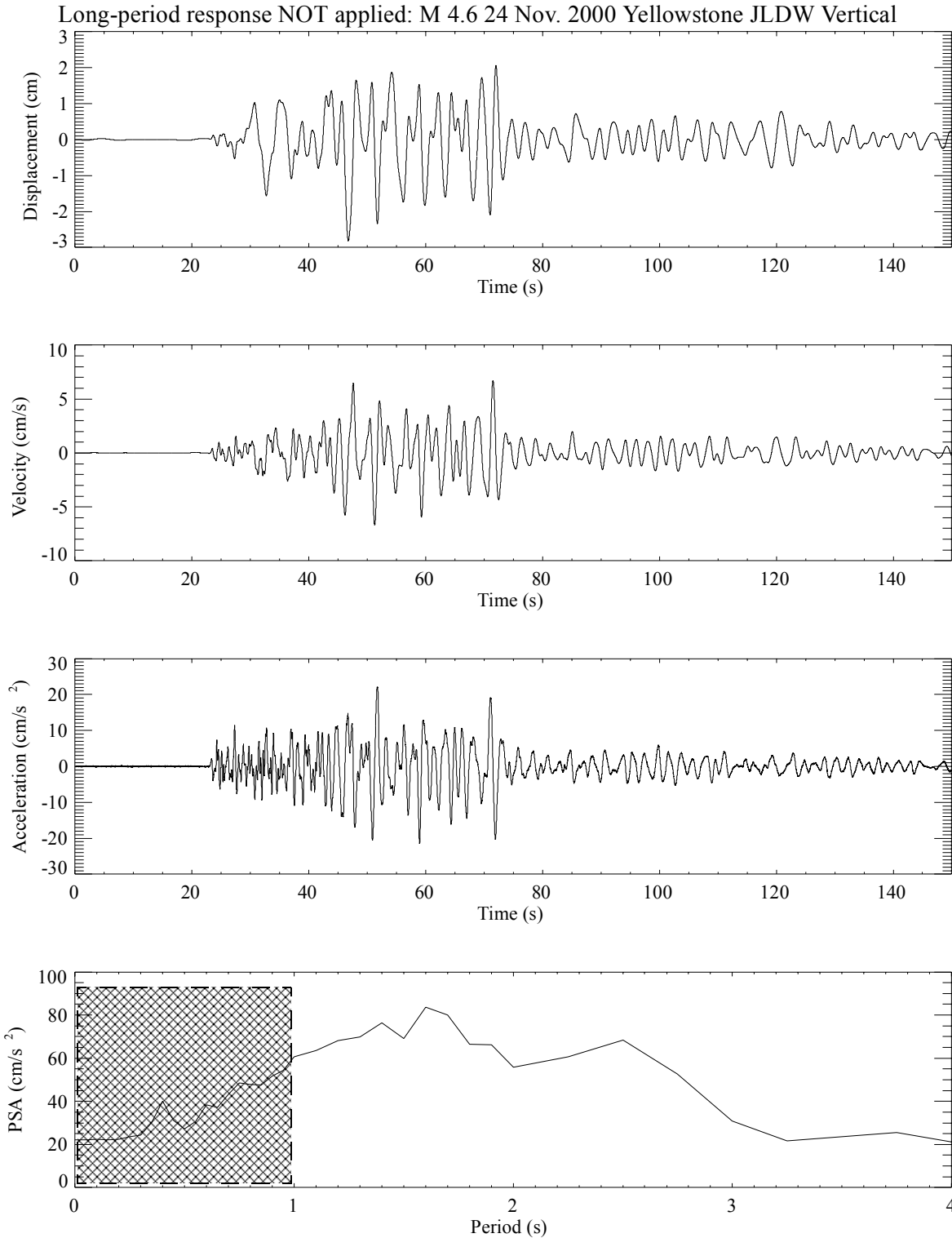


Figure 7-43: Subevent sum **M** 7.1 northern Teton fault earthquake simulation JLDW vertical response before long-period correction. The **M** 4.6 JLDW seismograms from Figure 7-40 were the EGF's used in (7-7). Corresponding complete synthetic vertical responses incorporating (7-8) are shown in Figure 7-44. Periods with inadequate S/N are hatched.

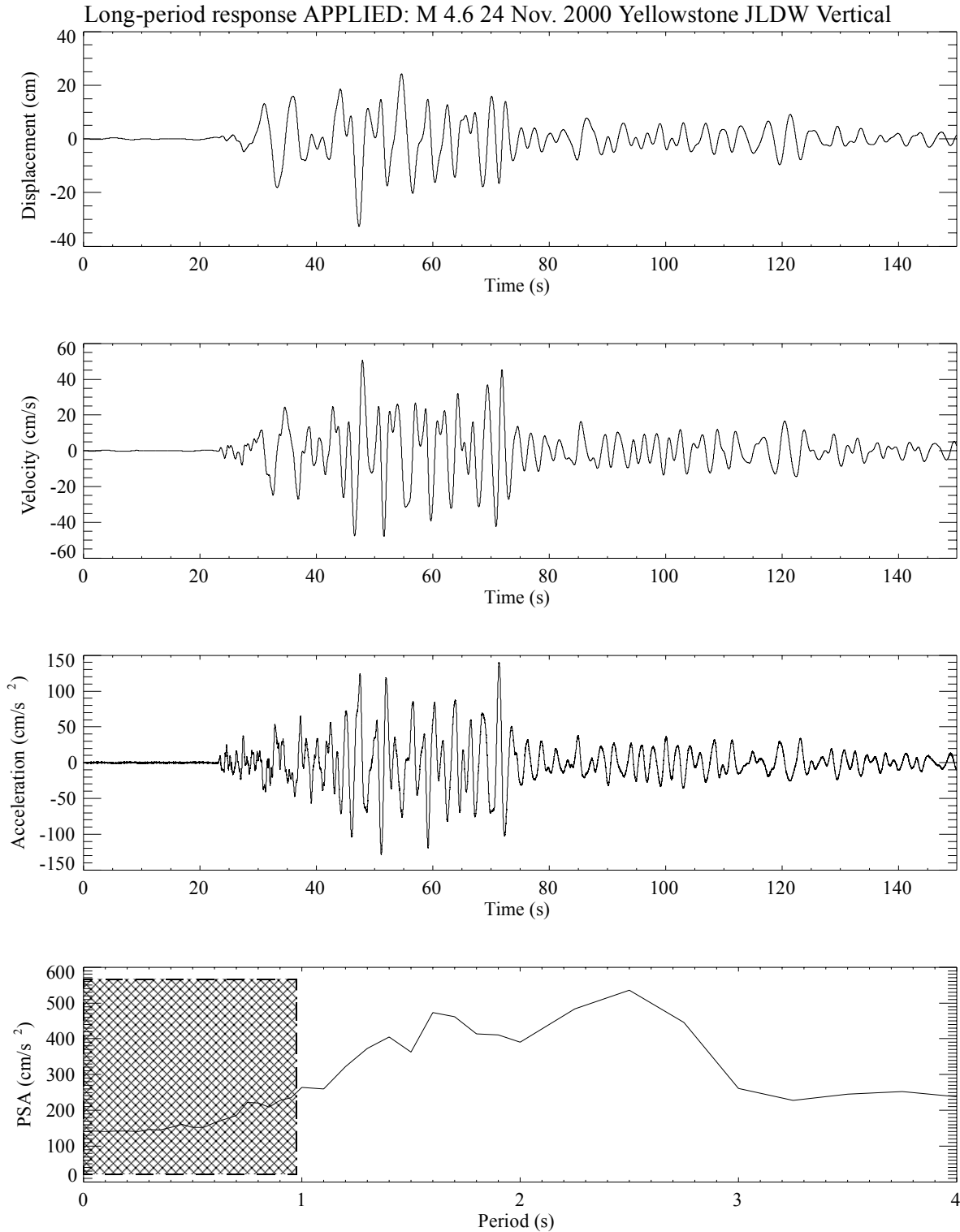


Figure 7-44: M 7.1 northern Teton fault earthquake simulation JLDW vertical response. This is the total response obtained by combining the velocity seismograms from Figure 7-43 with (7-8). Periods with inadequate S/N are hatched.

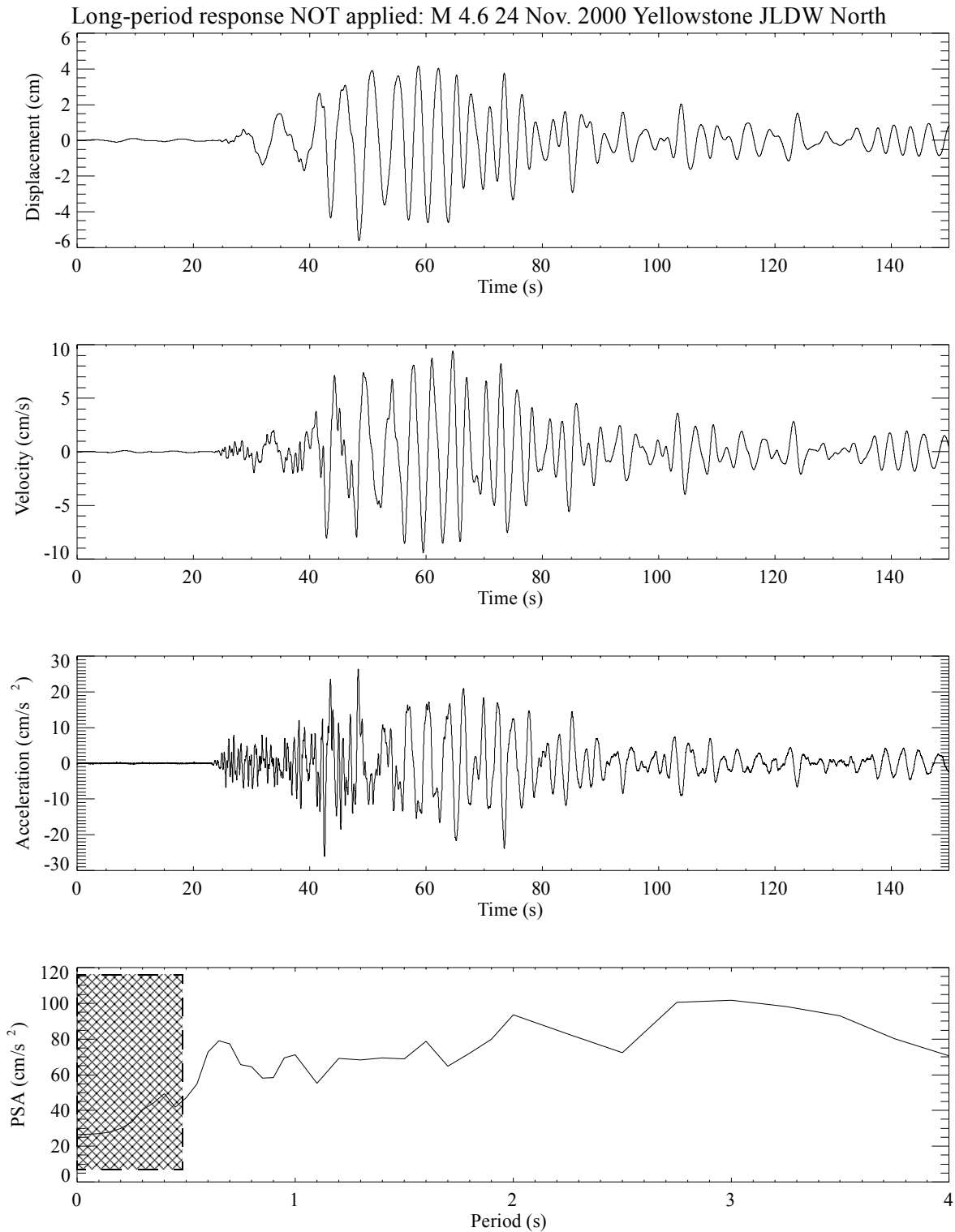


Figure 7-45: Subevent sum **M** 7.1 northern Teton fault earthquake simulation JLDW north response before long-period correction. The **M** 4.6 JLDW seismograms from Figure 7-44 were the EGF's used in (7-7). Corresponding complete synthetic vertical responses incorporating (7-8) are shown in Figure 7-46. Periods with inadequate S/N are hatched.

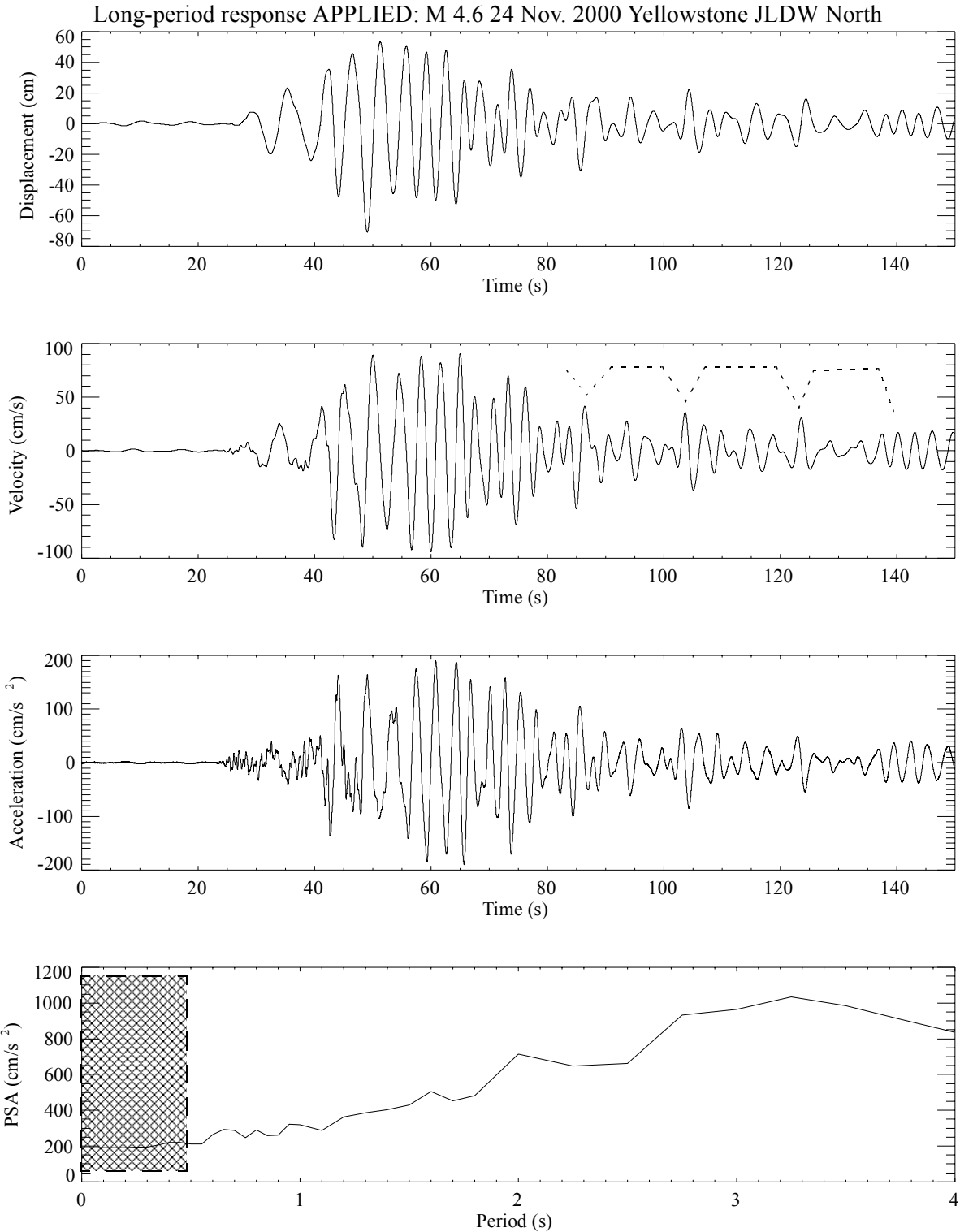


Figure 7-46: **M** 7.1 northern Teton fault earthquake simulation JLDW north response. This is the total response obtained by combining the velocity seismograms from Figure 7-45 with (7-8). Periods with inadequate S/N are hatched. Dotted line outlines local peak amplitudes in the coda separated by ~20 s intervals.

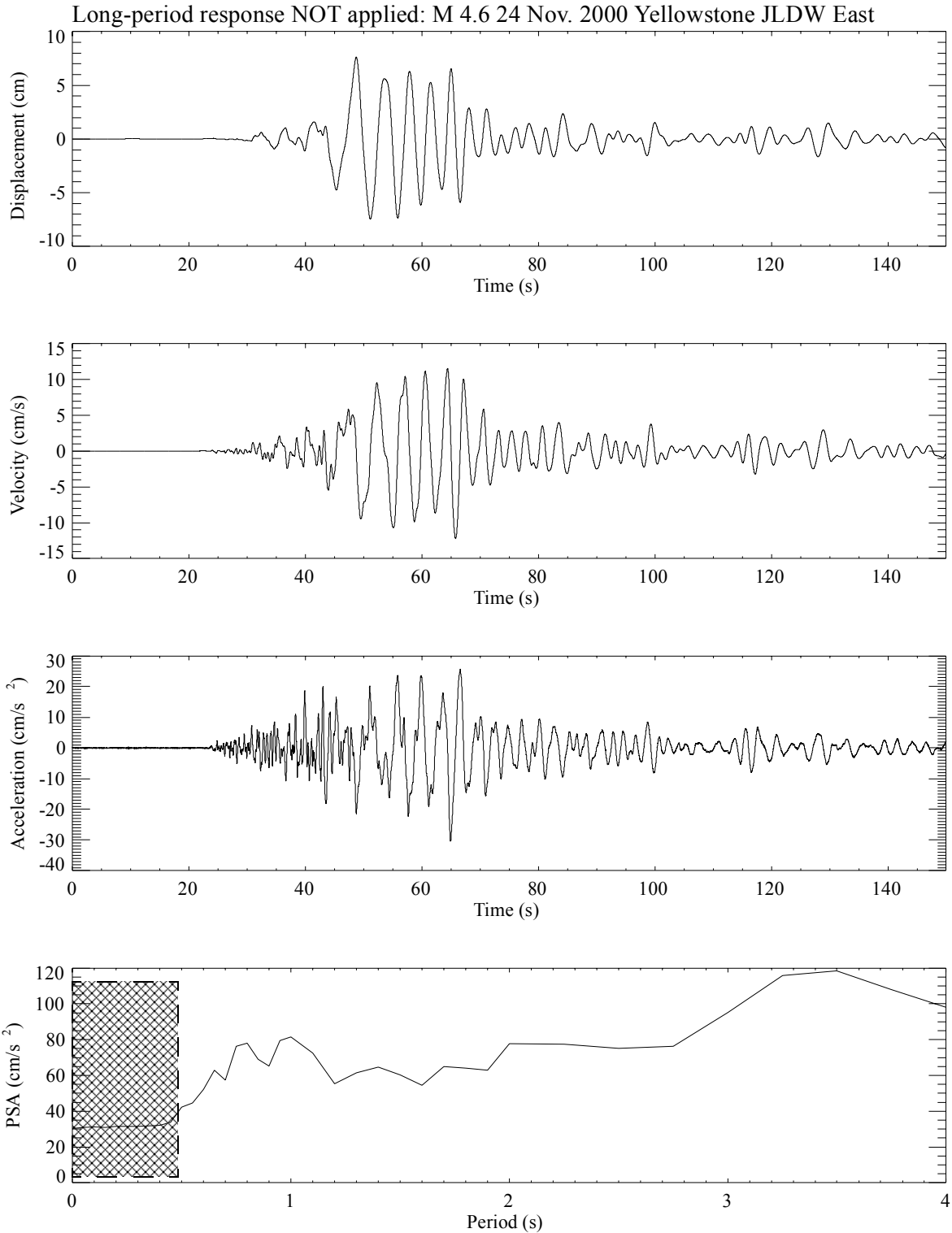


Figure 7-47: Subevent sum M 7.1 northern Teton fault earthquake simulation JLDW east response before long-period correction. The M 4.6 JLDW seismograms from Figure 7-44 were the EGF's used in (7-7). Corresponding complete synthetic vertical responses incorporating (7-8) are shown in Figure 7-48. Periods with inadequate S/N are hatched.

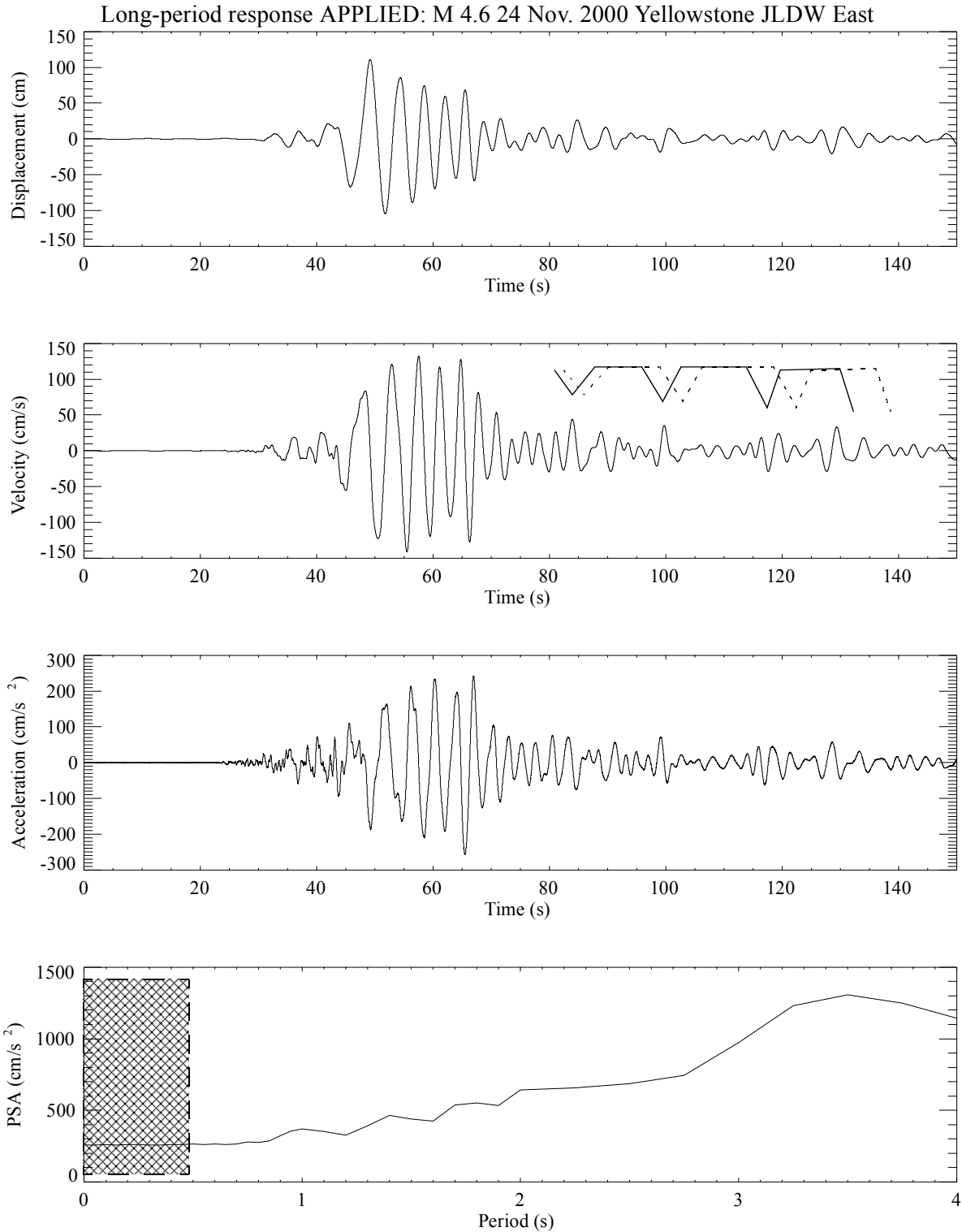


Figure 7-48: M 7.1 northern Teton fault earthquake simulation JLDW north response. This is the total response obtained by combining the velocity seismograms from Figure 7-47 with (7-8). Periods with inadequate S/N are hatched. Dotted line outlines local peak amplitudes in the coda separated by ~20 s intervals in the north component (Figure 7-46) and the solid line shows weaker local amplitude peaks with < 20 s intervals that may be associated with basin-edge-induced Love waves.

comprised of basin-edge-induced Love waves (~10% faster phase velocities relative to Rayleigh waves on the north component). Probably a significant portion of the 45-60 s time window on the east component is dominated by whole-path surface waves, so peak acceleration responses at periods > 2 s in Figure 7-48 are probably overestimated. Without reference broadband recordings outside the low-velocity basin it is not appropriate to make quantitative interpretations of the long-period acceleration responses in Figures 7-44, 7-46, and 7-48. What is clear from these simulations is that energy from the shallow portion of the northern Teton fault segment north of the low-velocity basin is likely to substantially increase strong motion durations at rock site JLDW, with peak velocities possibly exceeding 20 cm/s after two minutes of shaking. This strong basin excitation for energy arriving from a NNW azimuth may be associated with the abrupt, steeply dipping geometry of the northwest portion of the low-velocity basin margin as is discussed in more detail in Section 7.6.

7.4.2 Soil Site JLD3. Soil site JLD3's peak velocities from the **M** 5.2 Idaho earthquake (Figure 7-49) are amplified by a factors of 2-3 relative to the rock abutment reference site JLDW (Figure 7-31) which results in longer durations of stronger ground shaking with east peak velocities at a time of 170 s on Figure 7-49 that are four times larger than corresponding peak velocities at site JLDW. Figure 7-50 shows that there is adequate S/N to synthesize ground motions in the 0.1-10 Hz frequency band. The acceleration response spectra (Figure 7-51) have several strong resonances peak that are absent from the rock site JLD3 (Figure 7-33). The 5 Hz (0.2 s) resonance peak on all components in Figure 7-51 is probably associated with fundamental-mode resonance of the embankment. Assuming a 15 m structural height, an average embankment shear-wave velocity of 300 m/s, and a quarter-wavelength approximation, yields a resonance frequency of 5 Hz. Observation of embankment resonance response at site JLD3 is not surprising, since site JLD3 is located within ~15 m of the downstream toe of the embankment. Because site JLD3 is contaminated with structural resonance responses for frequencies of ~ 5 Hz are greater, interpretation of the JLD3 synthesized motions must be limited to periods > 0.2-0.3 s. The horizontal component resonance at 2 Hz correlates reasonably well with an impedance contrast at a depth of ~10 m in Figure 5-3 and average shear-wave velocities of 80-100 m/s. There is a strong local horizontal acceleration response peak at a period of ~1.2 s (Figure 7-51), consistent with a fundamental quarter-wavelength soil resonance for a 30 m deep soil with an average shear-wave

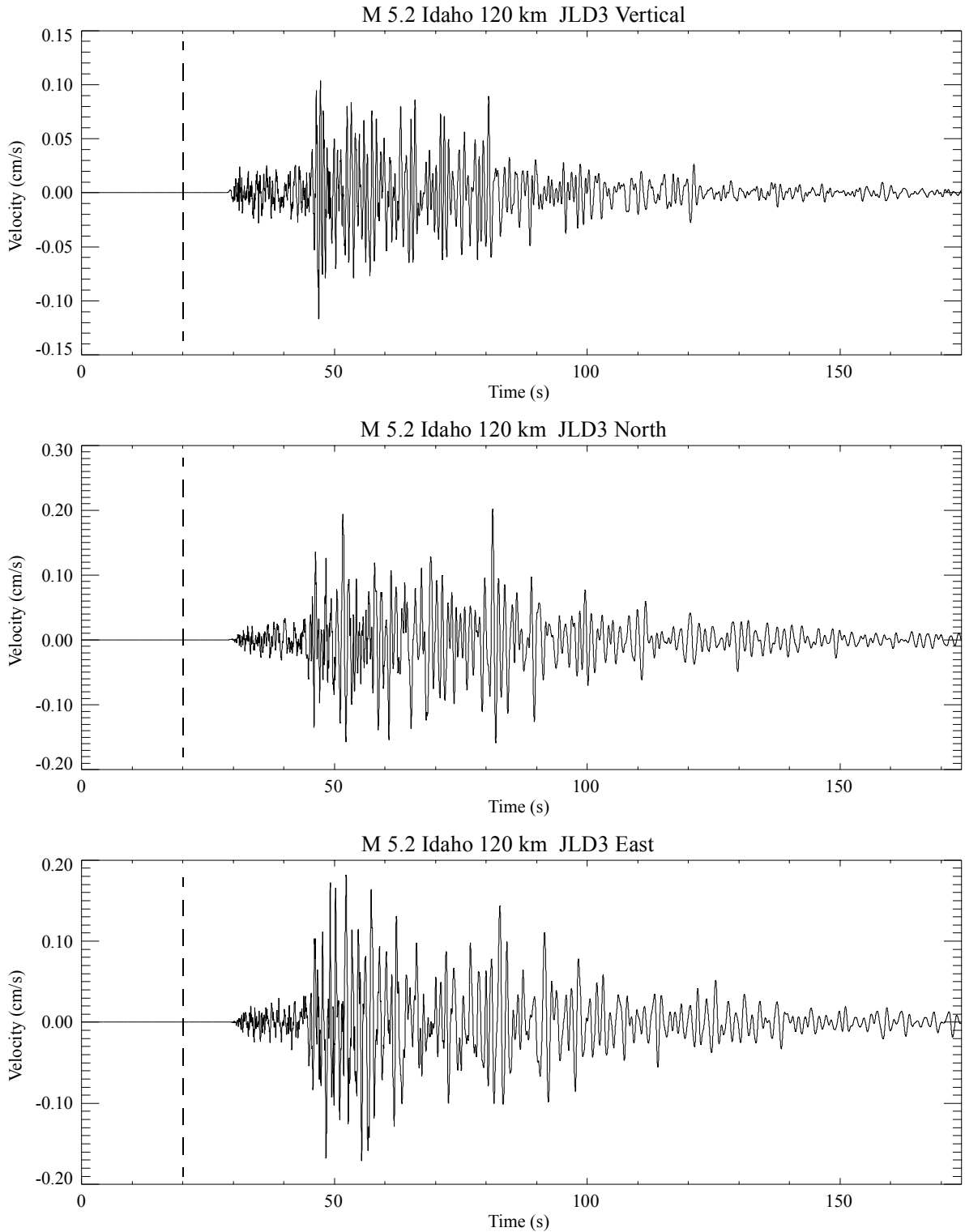


Figure 7-49: Site JLD3 velocity seismograms from the 21 Apr. 2001 **M** 5.2 Idaho earthquake. Components are as labeled. Vertical dashed lines divided the seismograms into pre-event noise and signal portions for spectra shown in Figure 7-50.

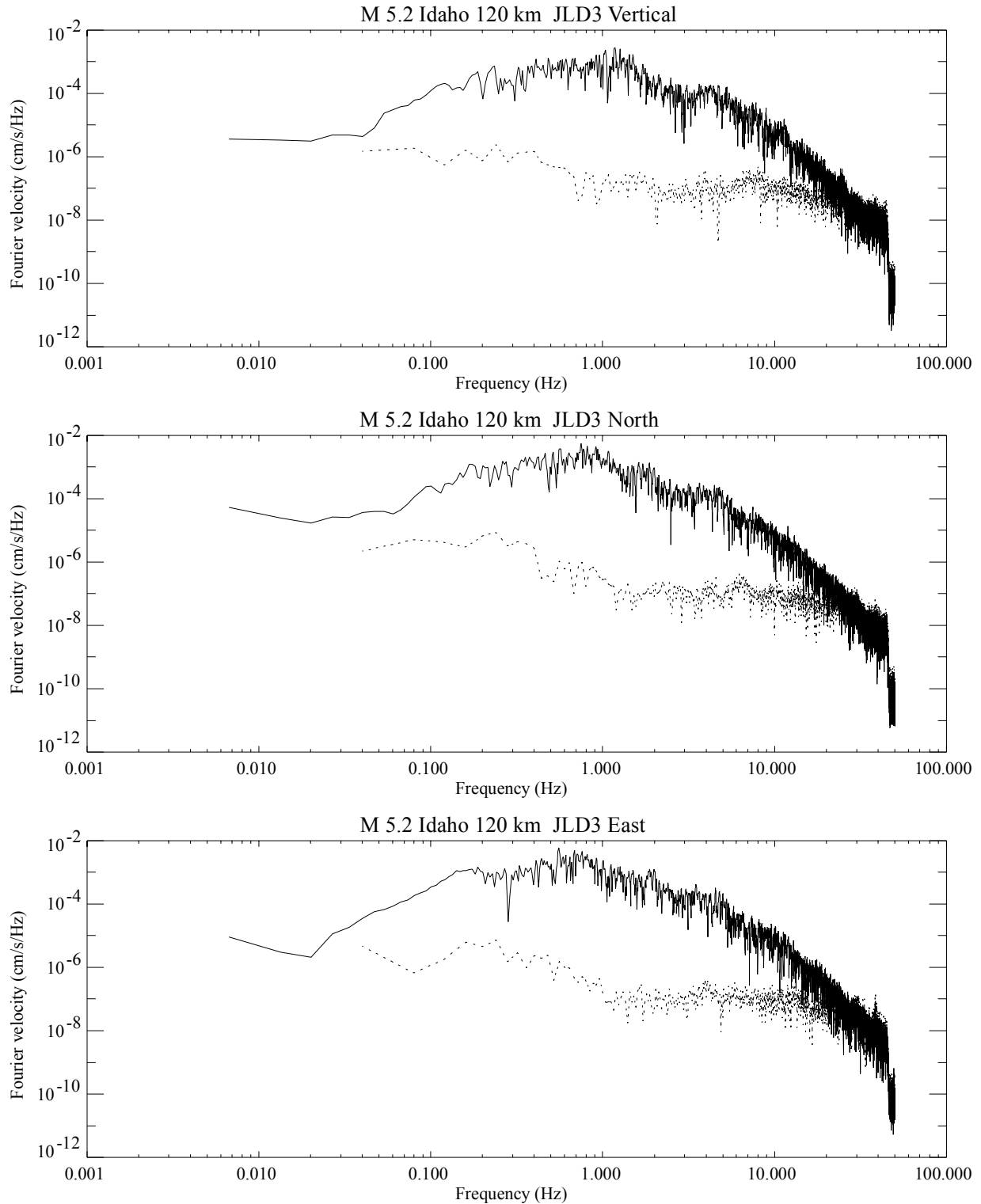


Figure 7-50: Site JLD3 Fourier velocity spectra from the 21 Apr. 2001 M 5.2 Idaho earthquake. Components are as labeled. Solid curves are signal spectra and dotted curves are noise spectra using the time windows indicated in Figure 7-49.

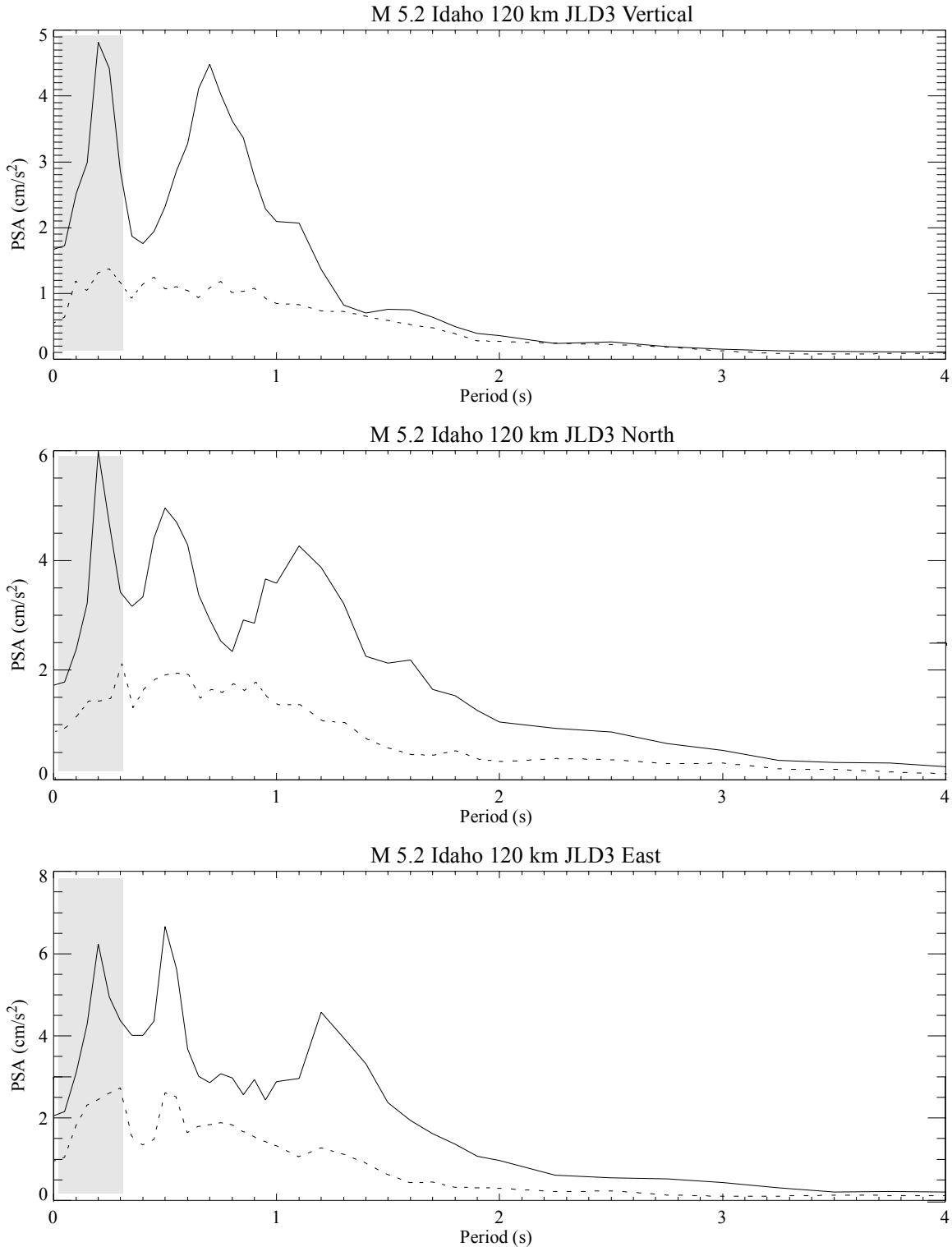


Figure 7-51: Site JLD3 acceleration response spectra from the 21 Apr. 2001 M 5.2 Idaho earthquake. Components are as labeled. The large 1-1.5 s horizontal responses are consistent with ~30 m thickness of low-velocity (~100 m/s shear-wave velocity) sediments. Dashed lines show corresponding rock site JLDW responses from Figure 7-33. Gray regions denote periods where the embankments resonant responses preclude interpreting the results in terms of ground response.

velocity of 100 m/s (From Figure 5-3). This represents a spectral acceleration amplification at 1.2 s of about a factor of 3-4 larger than rock site JLDW. Strong spectral acceleration amplification extends to periods of 3-4 s, consistent with an average soil basin shear-velocity of 140 m/s and an average soil thickness of 140 m beneath site JLD3 (and most of the embankment section of the dam). There is a 0.7 s resonant peak on the vertical component (Figure 7-51) that correlates with a persistent package of large amplitude arrivals in the 45-80 s time window in Figure 7-49 which is not easily explained using P-wave or shear-wave velocities indicated for the site in Figure 5-3.

For the vertical component synthetic motions, the largest differences in response between soil site JLD3 and rock site JLDW are at periods < 1 s (Figure 7-52 and 7-53). This is somewhat inexplicable because soil responses are generally assumed to not strongly influence vertical ground motions (shear-waves at near-vertical-incidence should only weakly influence vertical motions). It's difficult to invoke *S-to-P* converted phases as a suspect since the maximum vertical acceleration responses coincide with the arrival of the first shear-waves and large acceleration phases on the horizontal components (Figures 7-54 to 7-57). If nearly-vertical shear-waves are not responsible for the large < 1 s vertical accelerations, it is not clear how to account for the influence of soil nonlinearity on the vertical soil ground motions.

JLD3 north component soil acceleration responses are nearly uniformly amplified (Figures 7-54 and 7-55) relative to rock site JLDW responses for periods < 2 s with soil amplification nearly monotonically decreasing with increasing period for periods > 2 s (Figure 7-55). Peak velocities exceeding 70 cm/s span an 85 s time window and peak velocities exceeding 100 cm/s span a 45 s time window. While soil nonlinearly is expected to sharply attenuate acceleration responses for periods < 1 s, recent investigations (Archuleta et al., 2000; Bonilla, 2000) have showed that soil nonlinearity is likely to *increase* accelerations responses for periods > 1 s. Thus, while north component soil acceleration responses at site JLD3 for periods in the 1-2 s range exceed 2 g (Figure 7-55) soil nonlinearity may actually further amplify > 1 s acceleration responses. Comparable results are obtained for the east component (Figure 7-56 and 7-57) except that peak accelerations, velocities, and displacements are larger than the north component.

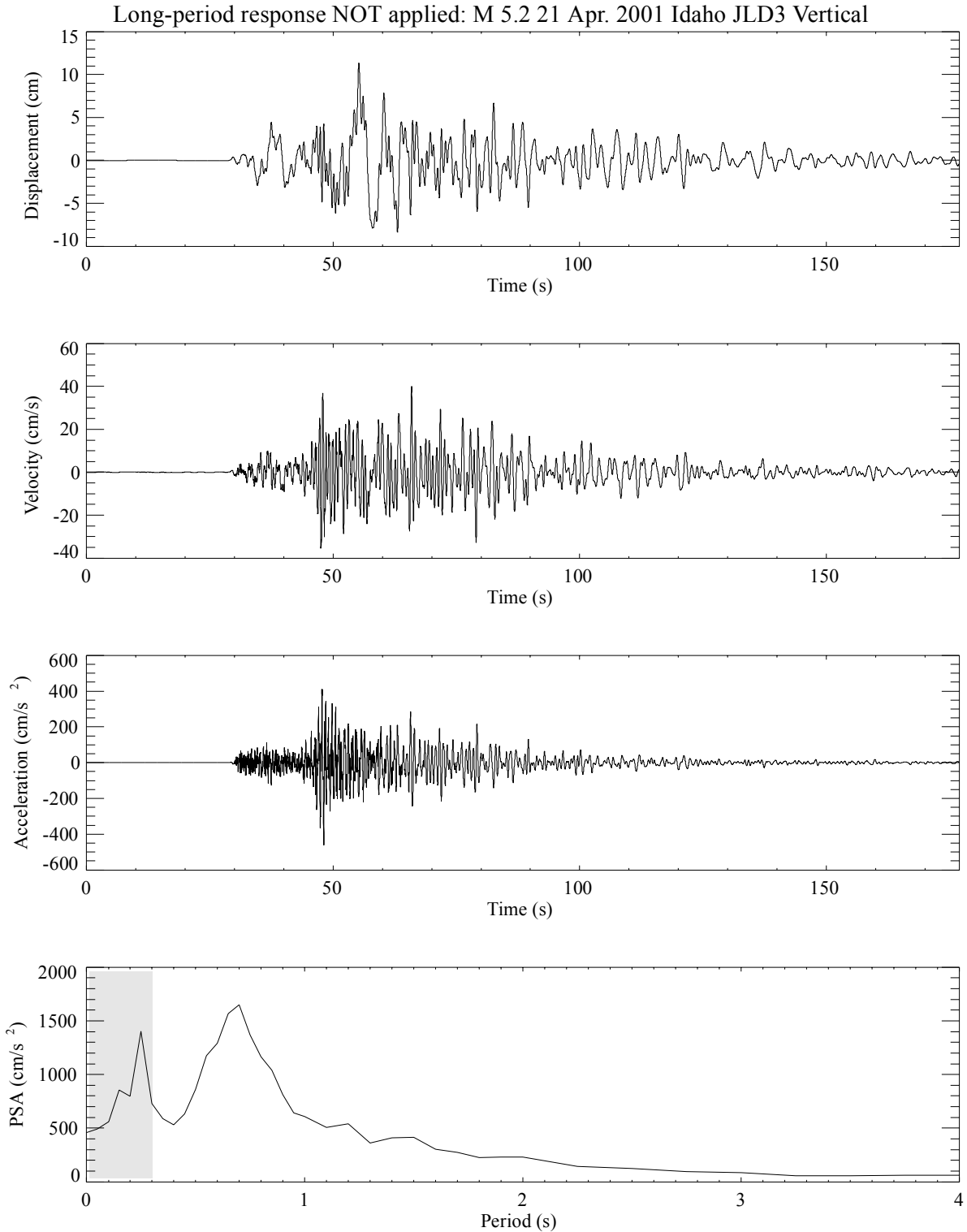


Figure 7-52: Subevent sum **M** 7.1 northern Teton fault earthquake simulation JLD3 vertical response before long-period correction. The **M** 5.2 JLDW seismograms from Figure 7-49 were the EGF's used in (7-7). Corresponding complete synthetic vertical responses incorporating (7-8) are shown in Figure 7-53. Gray region is contaminated with embankment resonant responses.

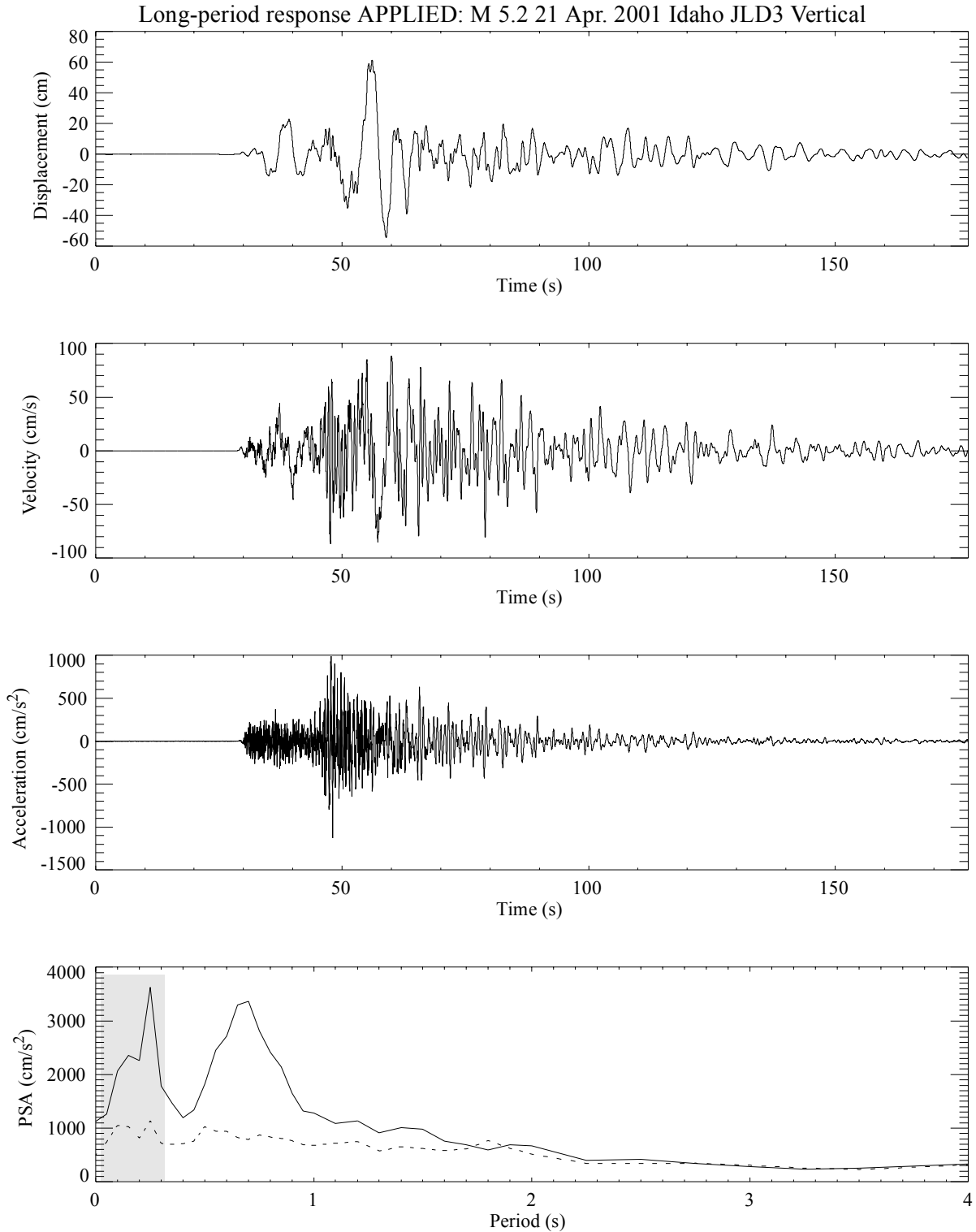


Figure 7-53: **M** 7.1 northern Teton fault earthquake simulation JLD3 vertical response. This is the total response obtained by combining the velocity seismograms from Figure 7-52 with (7-8). Dashed line shows the corresponding JLDW rock site PSA response. Gray region is contaminated with embankment resonant responses.

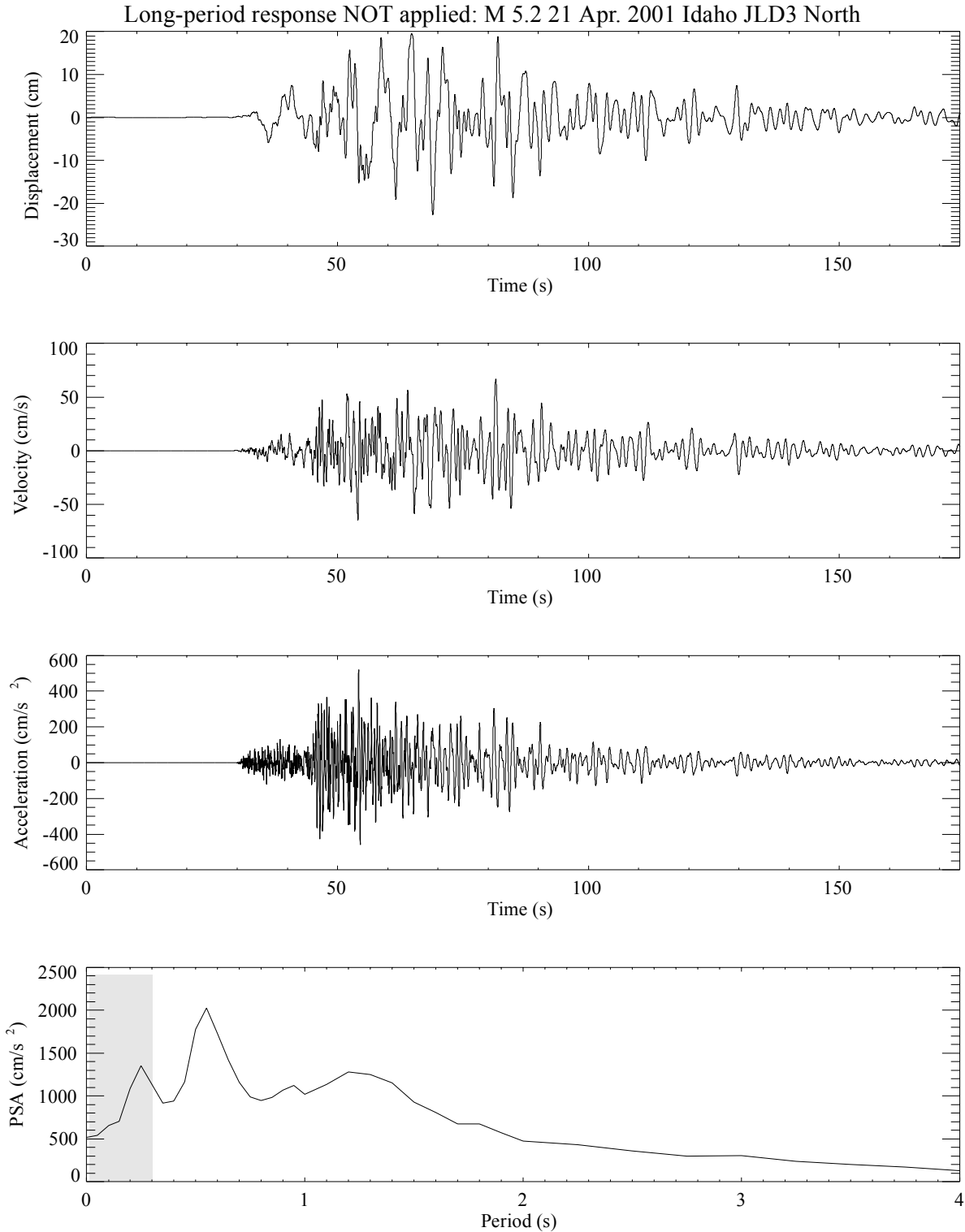


Figure 7-54: Subevent sum **M** 7.1 northern Teton fault earthquake simulation JLD3 north response before long-period correction. The **M** 5.2 JLDW seismograms from Figure 7-49 were the EGF's used in (7-7). Corresponding complete synthetic vertical responses incorporating (7-8) are shown in Figure 7-55. Gray region is contaminated with embankment resonant responses.

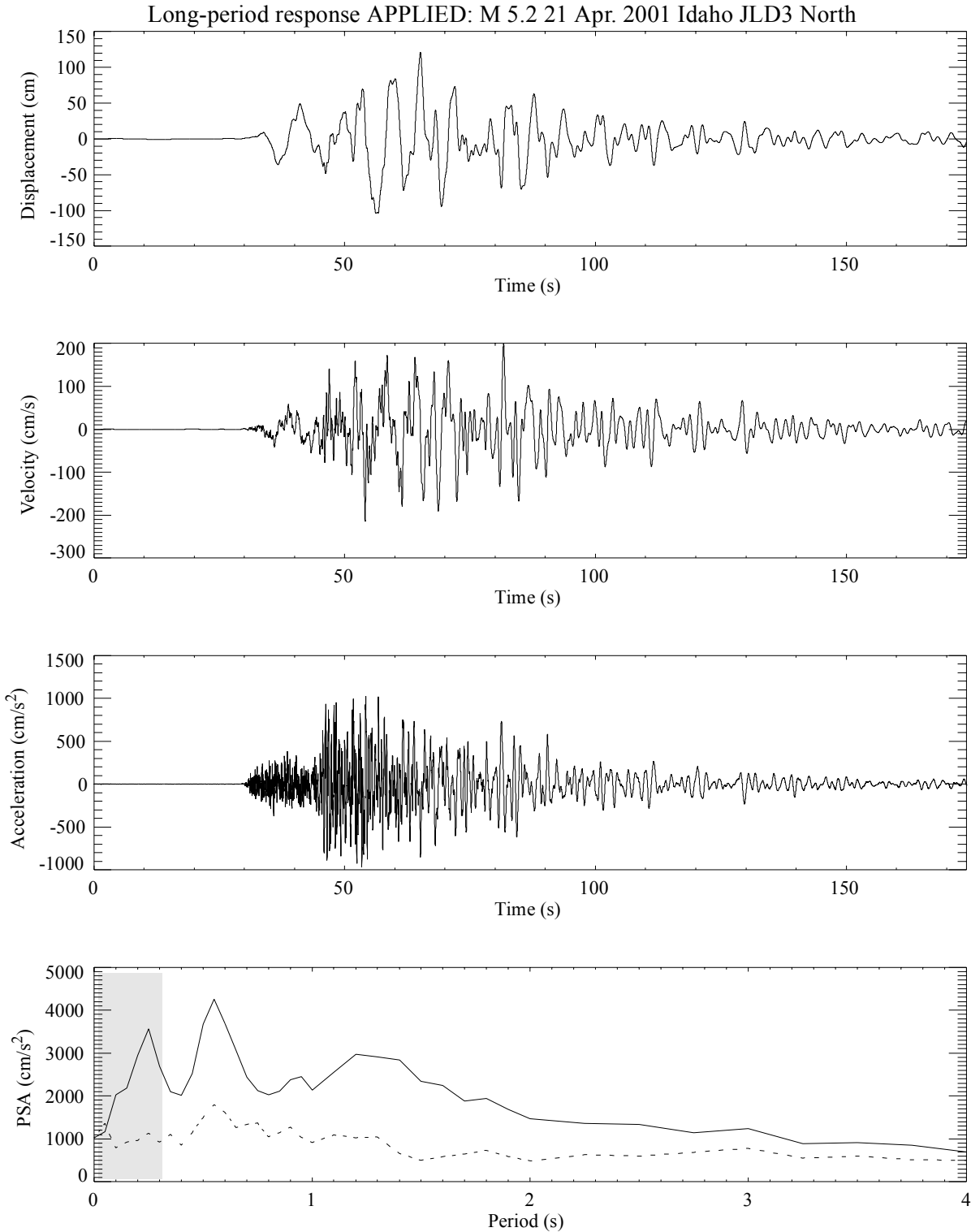


Figure 7-55: **M** 7.1 northern Teton fault earthquake simulation JLD3 north response. This is the total response obtained by combining the velocity seismograms from Figure 7-54 with (7-8). Dashed line shows the corresponding JLDW rock site PSA response. Gray region is contaminated with embankment resonant responses.

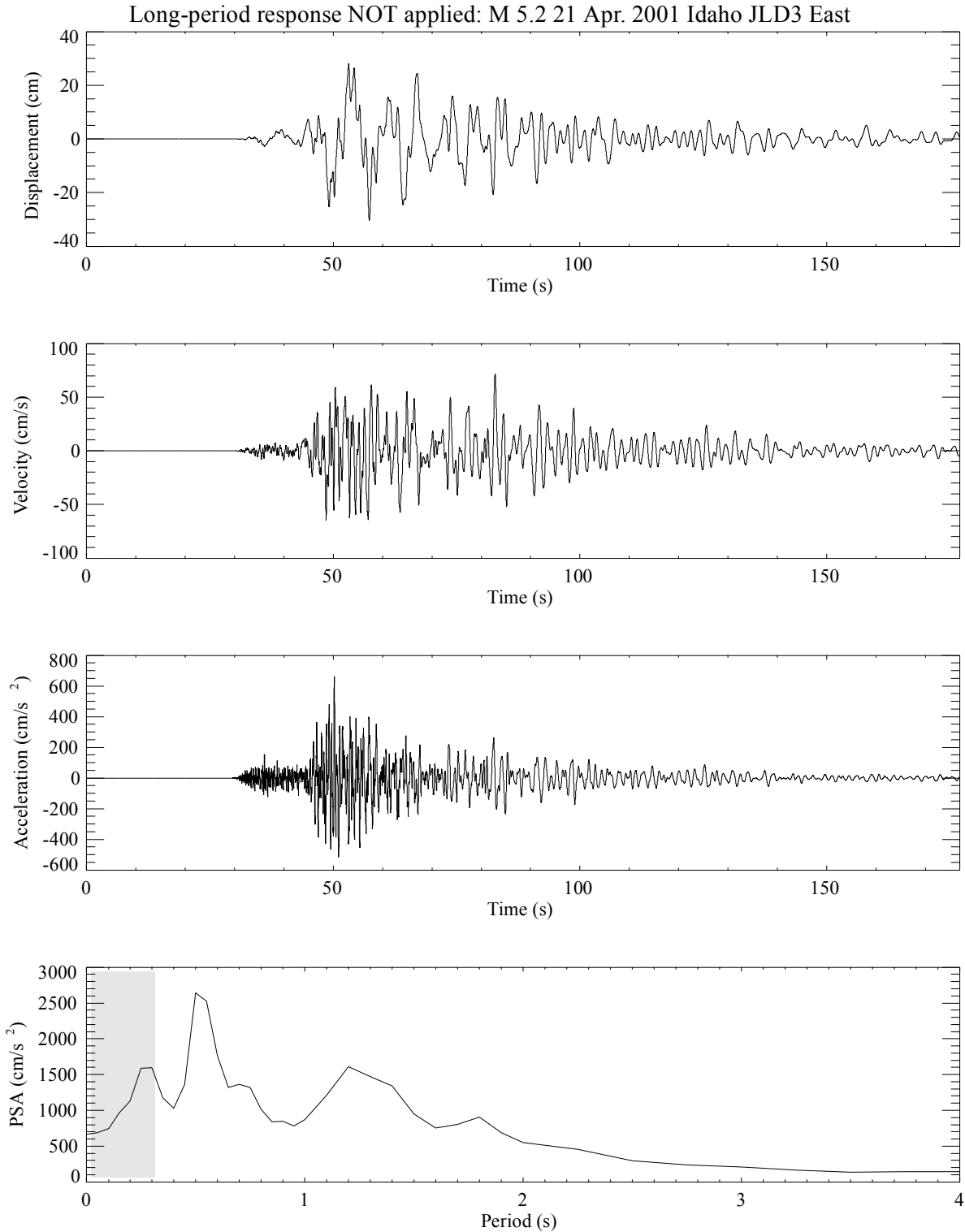


Figure 7-56: Subevent sum **M** 7.1 northern Teton fault earthquake simulation JLD3 east response before long-period correction. The **M** 5.2 JLDW seismograms from Figure 7-49 were the EGF's used in (7-7). Corresponding complete synthetic vertical responses incorporating (7-8) are shown in Figure 7-57. Gray region is contaminated with embankment resonant responses.

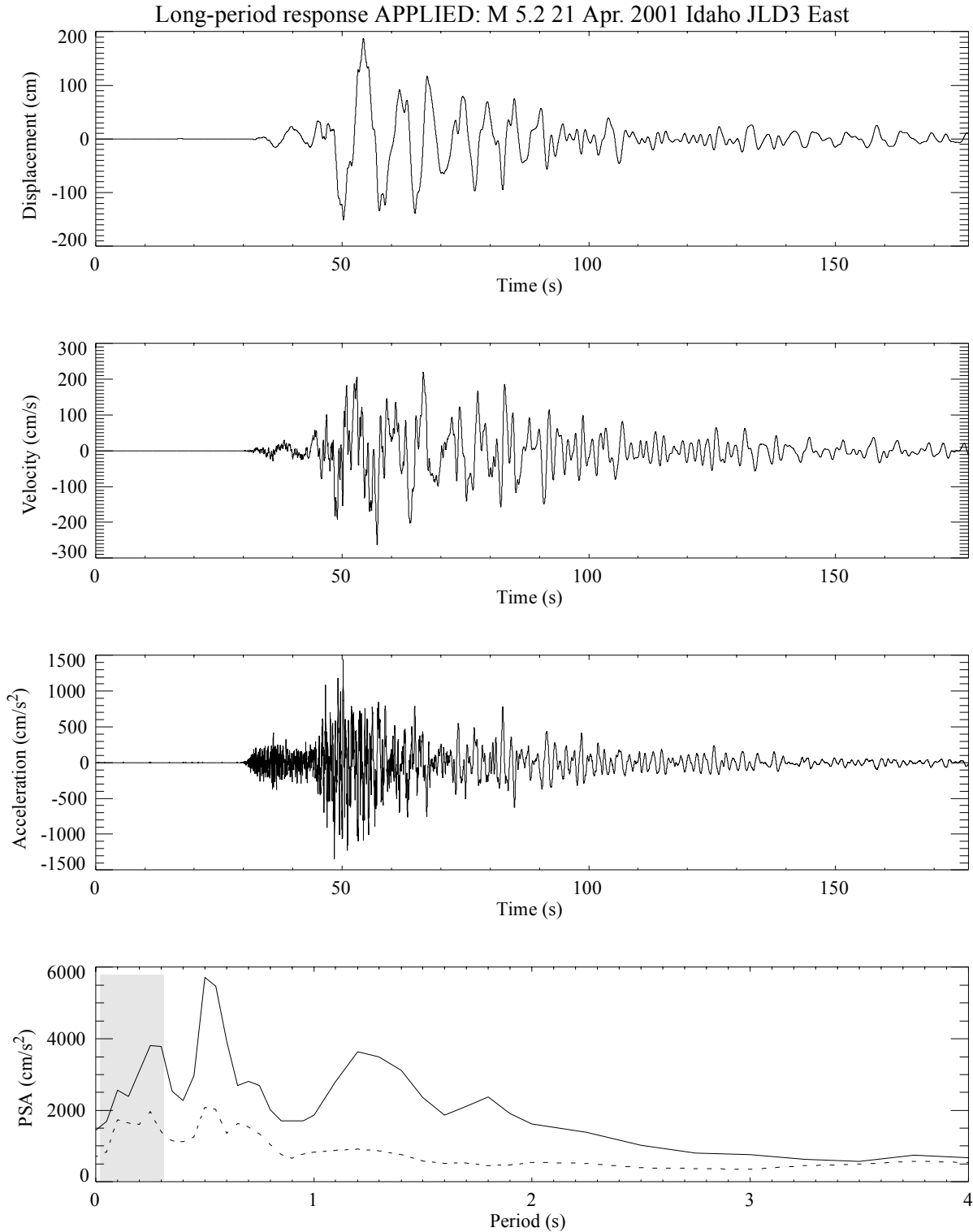


Figure 7-57: **M** 7.1 northern Teton fault earthquake simulation JLD3 east response. This is the total response obtained by combining the velocity seismograms from Figure 7-56 with (7-8). Dashed line shows the corresponding JLDW rock site PSA response. Gray region is contaminated with embankment resonant responses.

Soil site JLD3 seismograms from the **M** 4.6 Yellowstone earthquake are virtually devoid of high-frequency shear-waves (Figure 7-58) as were the rock site seismograms (Figure 7-40). The usable periods band with adequate S/N extends from about 0.5 s to 5 s (Figure 7-59). The amplified 1-2 s period soil site responses are clearly apparent in the acceleration response spectra (Figure 7-60). Synthesized vertical responses are only modestly amplified, except for periods < 1 s (Figures 7-61 and 7-62), similar to the vertical responses obtained using the **M** 5.2 Idaho JLD3 vertical EGF. North component acceleration responses are nearly uniformly amplified independent of period (Figure 7-63 and 7-64) relative to rock site JLDW responses. In contrast, east component acceleration amplification modestly decreases with increase period for periods > 2.5 s (Figures 7-65 and 7-66). The very-low-velocity soil basin deepens in the northerly direction and the increased acceleration amplifications at soil site JLD3 at periods > 2 s relative to the rock site JLDW for the Yellowstone earthquake probably reflect an effectively deeper soil basin for energy incident from the NNW relative to energy arriving from the SSW (Idaho earthquake). The Yellowstone EGF results suggest that energy arriving from the northern end of the northern Teton fault segment will more strongly amplify long-period accelerations along the embankment section of the dam than energy incident from the southern end of the northern Teton fault segment or the southern Teton fault segment. This is discussed in more detail using local earthquakes in Section 7.5 below.

7.5 Ground Motion Synthesis with Local Broadband Empirical Green's Functions

The database of site response earthquake recordings yielded two local earthquakes located near the northern Teton fault segment with sufficient S/N to use as EGF's for simulating ground motions for periods extending to 2-3 s (Table 7-4). A third local **M** 3.7 earthquake located near

Table 7-4: Local Broadband Empirical Green's Function Earthquake Information

Date (yr/mon/day)	Time (hr,min,sec)	Latitude (degrees N)	Longitude (degrees E)	Elevation (km wrt msl)	Magnitude
1998/07/11	16:10:3.152	43.91073	-110.64070	-3.72	2.9
2002/11/20	02:14:2.000	43.68424	-110.49812	-2.87	3.2

the southern Teton fault segment provides some information about the likely response

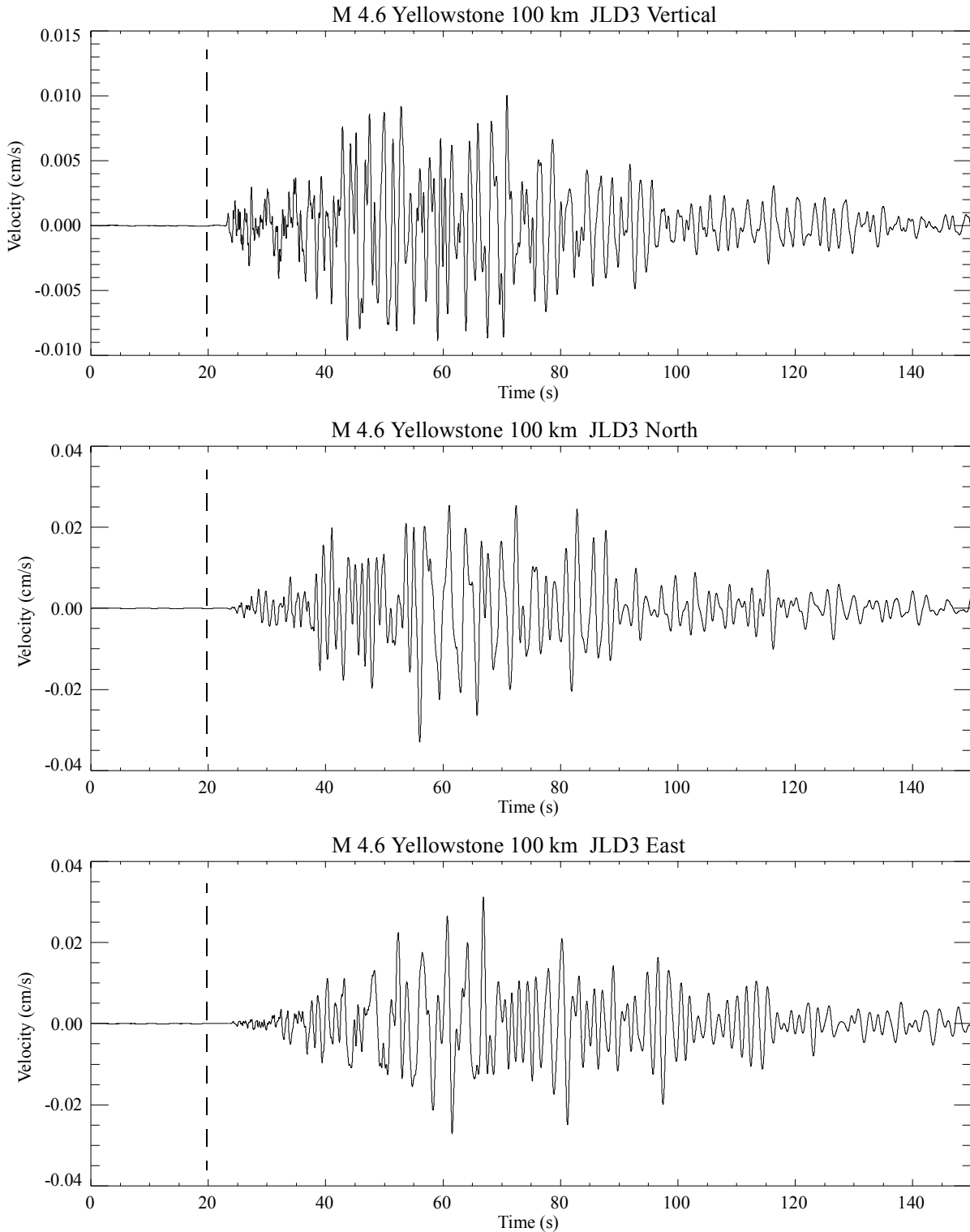


Figure 7-58: Site JLD3 velocity seismograms from the 24 Nov. 2000 M 4.6 Yellowstone earthquake. Components are as labeled. Vertical dashed lines divided the seismograms into pre-event noise and signal portions for spectra shown in Figure 7-59. Note significant amplitudes persist to the end of the record.

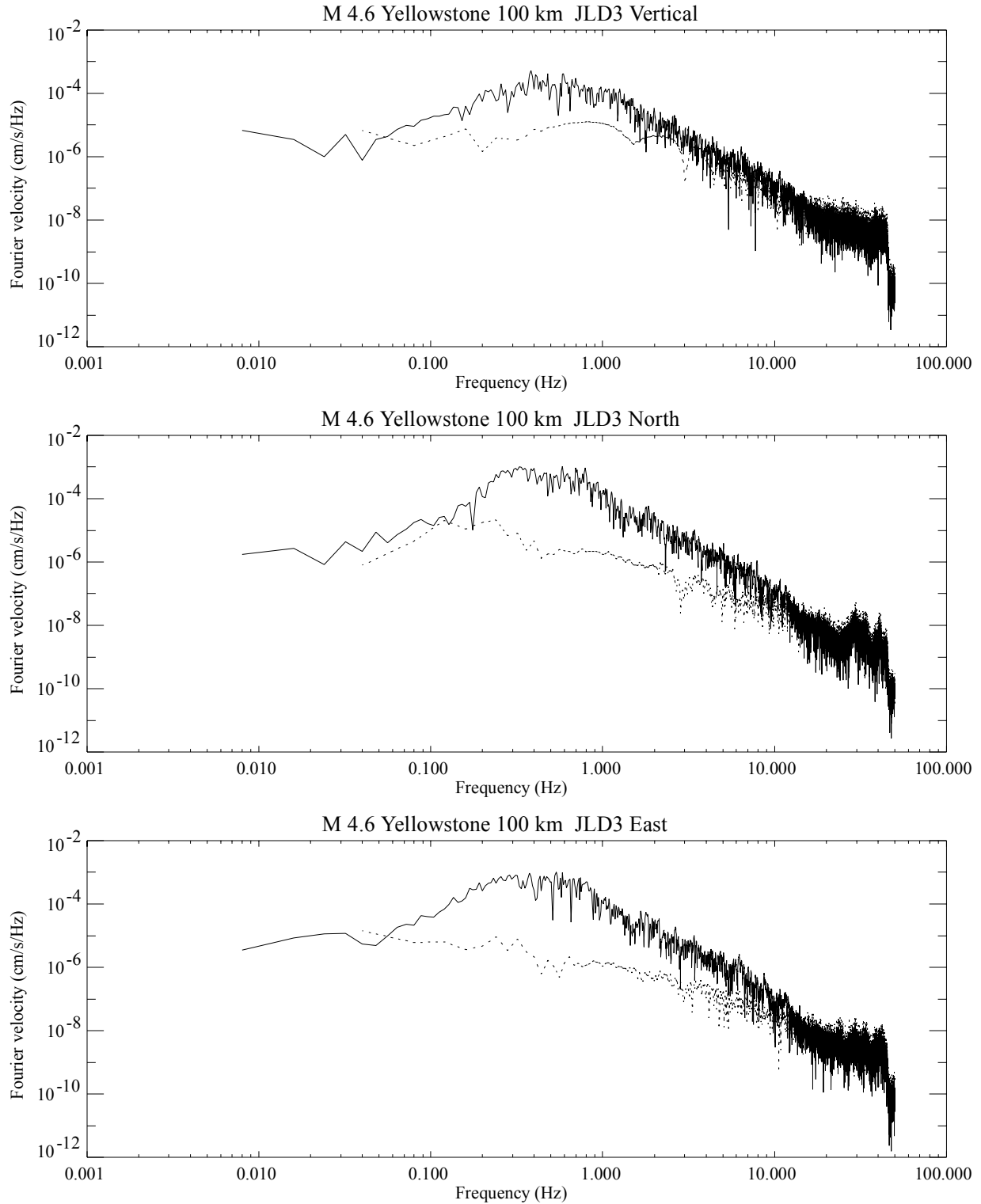


Figure 7-59: Site JLD3 Fourier velocity spectra from the 24 Nov. 2000 M 4.6 Yellowstone earthquake. Components are as labeled. Solid curves are signal spectra and dotted curves are noise spectra using the time windows indicated in Figure 7-58.

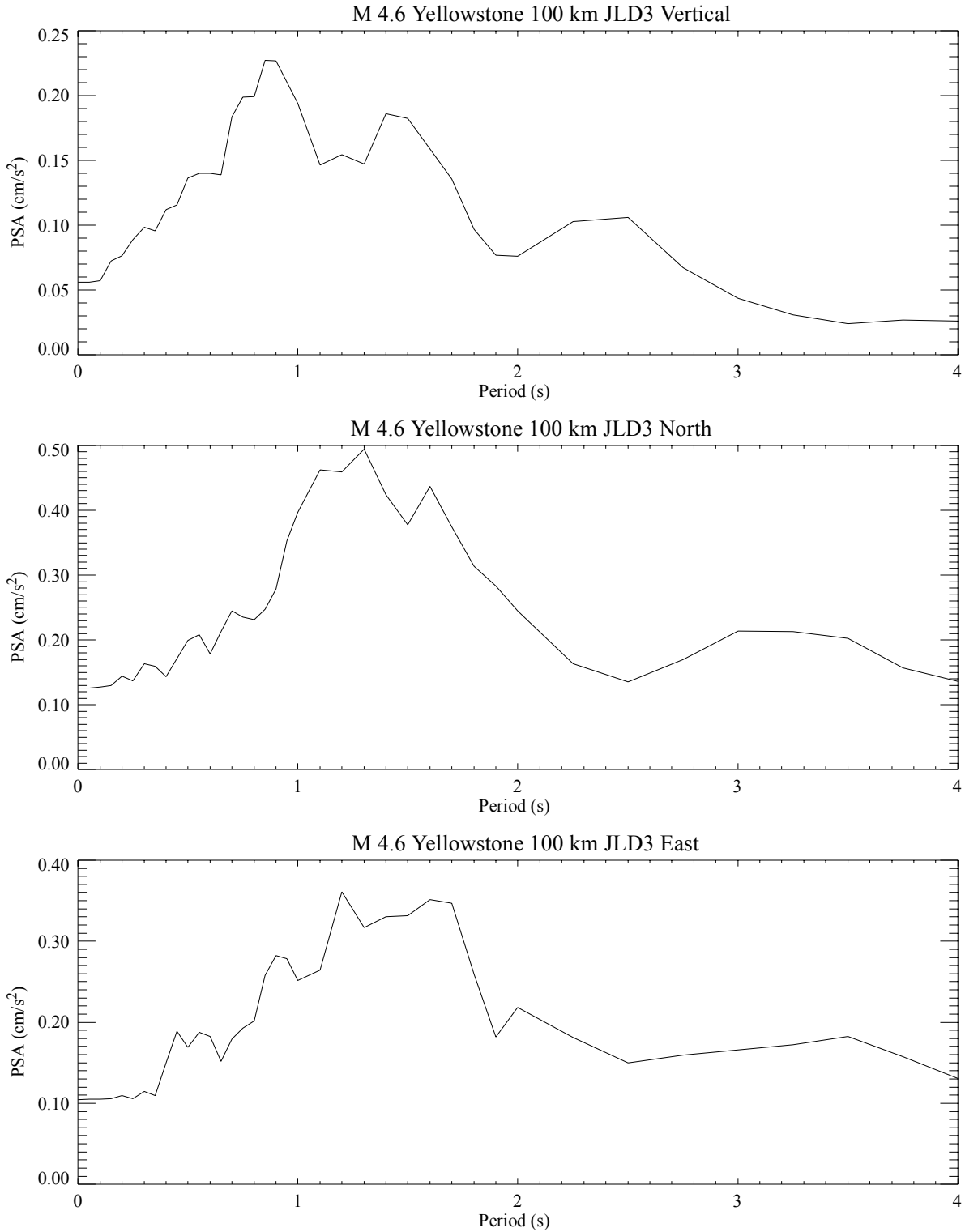


Figure 7-60: Site JLD3 acceleration response spectra from the 24 Nov. 2000 M 4.6 Yellowstone earthquake. Components are as labeled. Note the largest horizontal responses are between 1 s and 2 s.

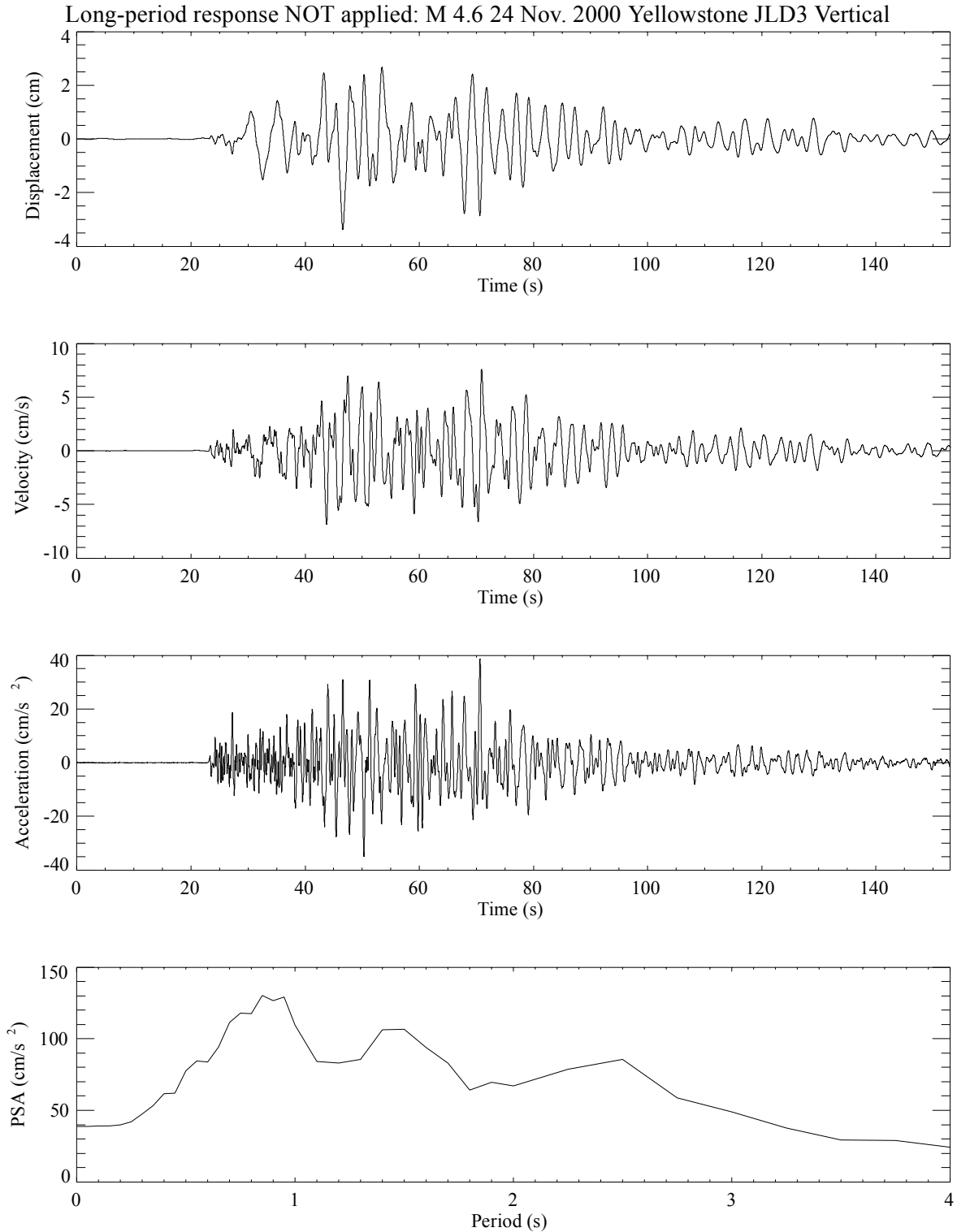


Figure 7-61: Subevent sum M 7.1 northern Teton fault earthquake simulation JLD3 vertical response before long-period correction. The M 4.6 JLDW seismograms from Figure 7-58 were the EGF's used in (7-7). Corresponding complete synthetic vertical responses incorporating (7-8) are shown in Figure 7-62.

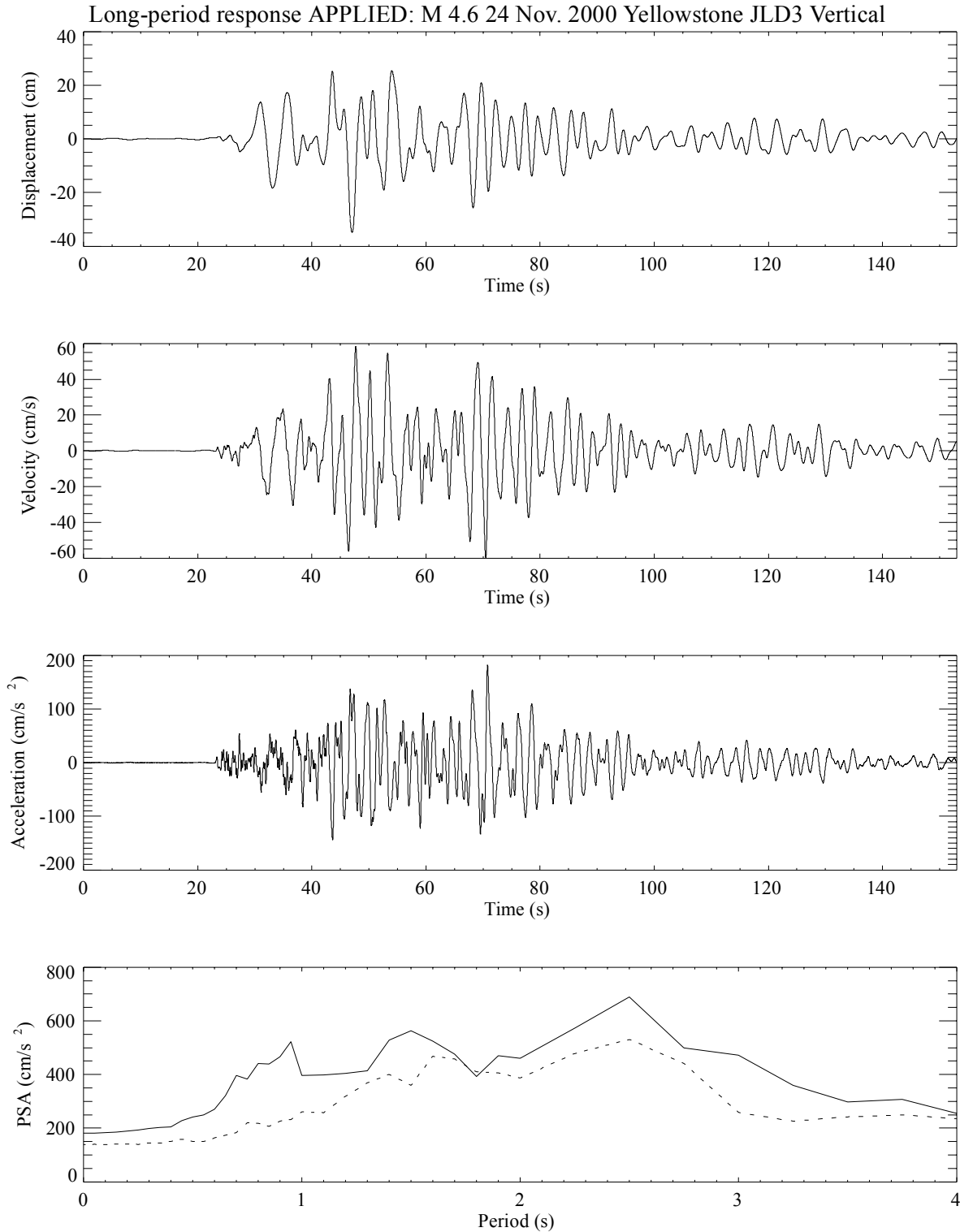


Figure 7-62: M 7.1 northern Teton fault earthquake simulation JLD3 vertical response. This is the total response obtained by combining the velocity seismograms from Figure 7-61 with (7-8).

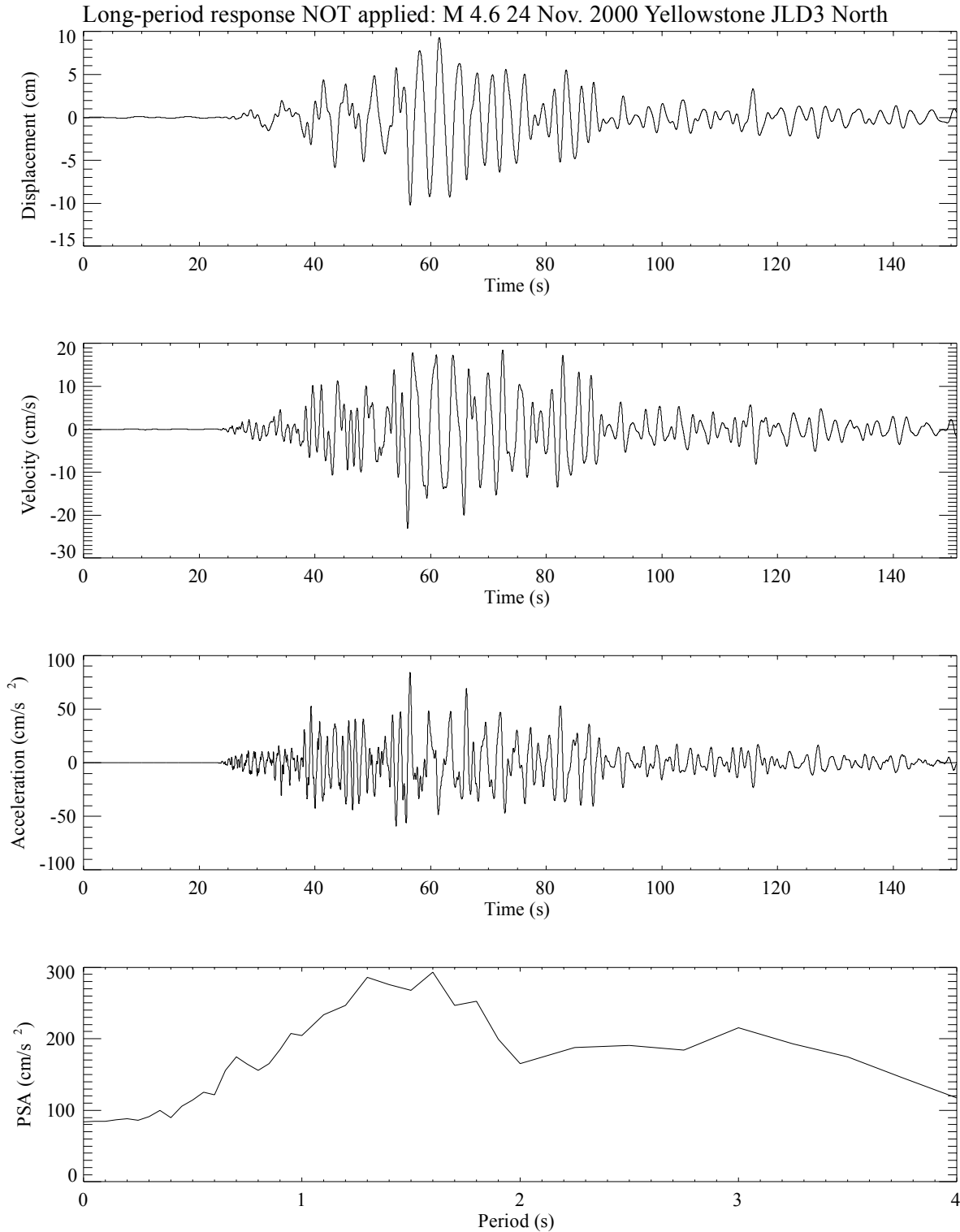


Figure 7-63: Subevent sum **M** 7.1 northern Teton fault earthquake simulation JLD3 north response before long-period correction. The **M** 4.6 JLDW seismograms from Figure 7-58 were the EGF's used in (7-7). Corresponding complete synthetic vertical responses incorporating (7-8) are shown in Figure 7-64.

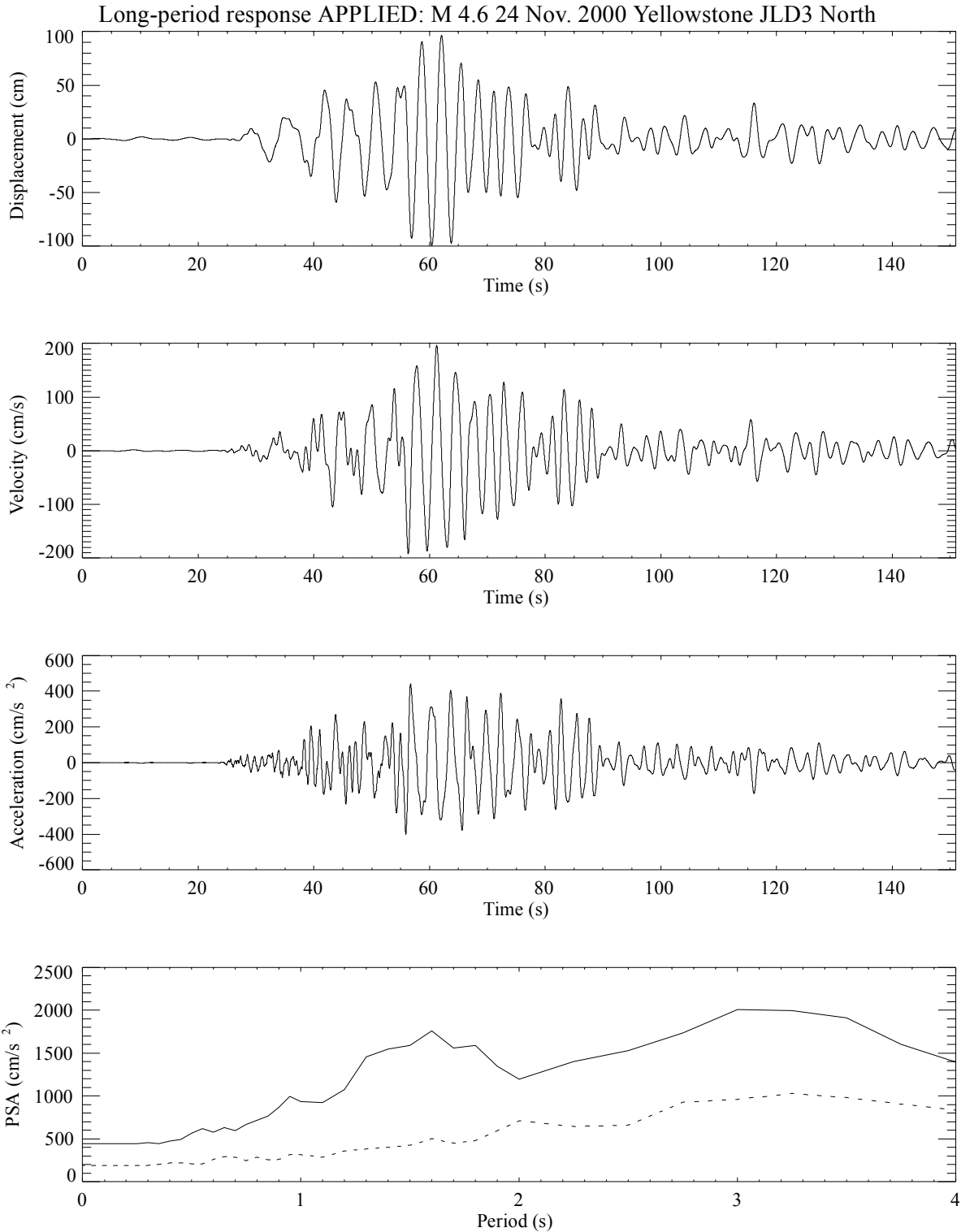


Figure 7-64: M 7.1 northern Teton fault earthquake simulation JLD3 north response. This is the total response obtained by combining the velocity seismograms from Figure 7-45 with (7-8).

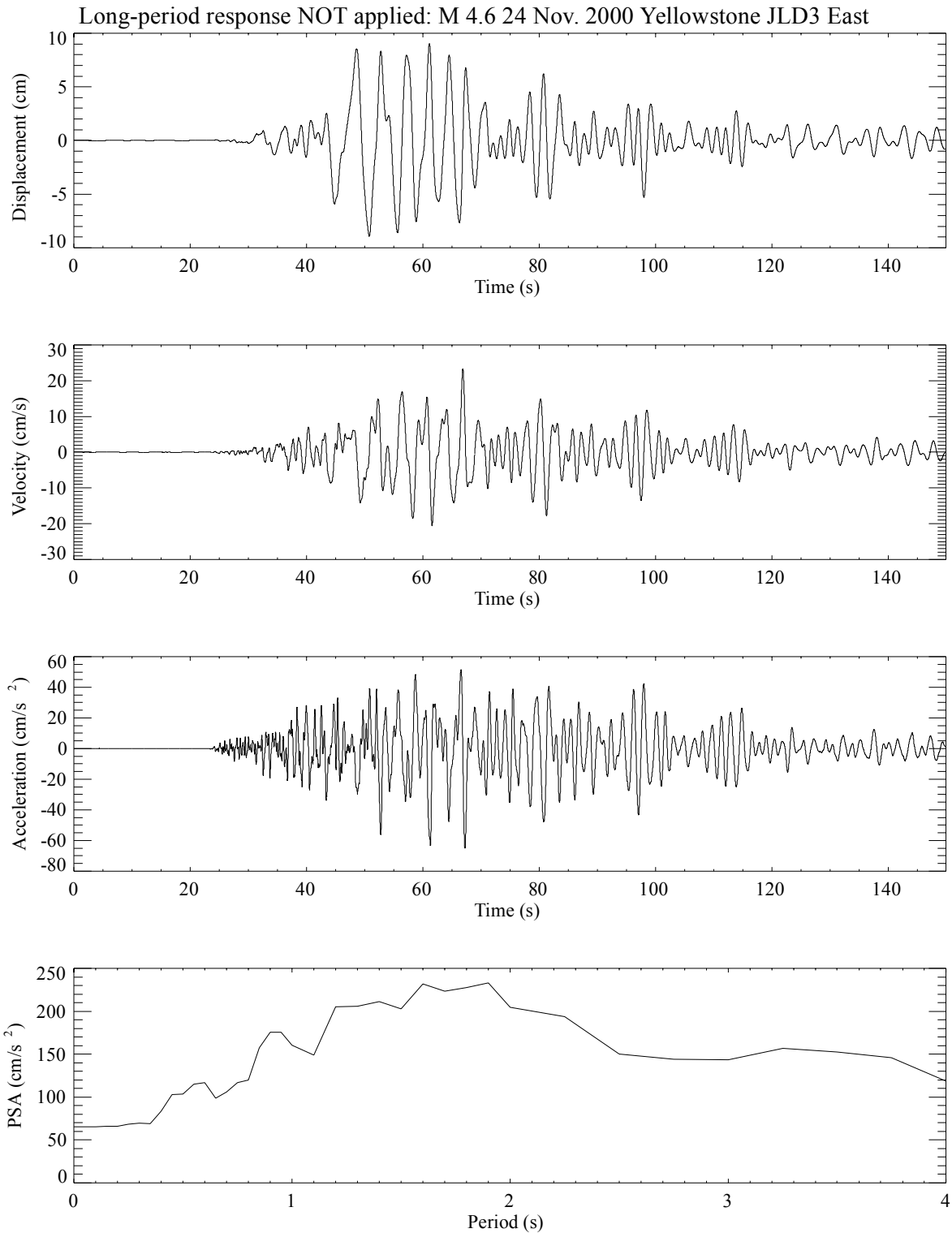


Figure 7-65: Subevent sum M 7.1 northern Teton fault earthquake simulation JLD3 east response before long-period correction. The M 4.6 JLDW seismograms from Figure 7-58 were the EGF's used in (7-7). Corresponding complete synthetic vertical responses incorporating (7-8) are shown in Figure 7-66.

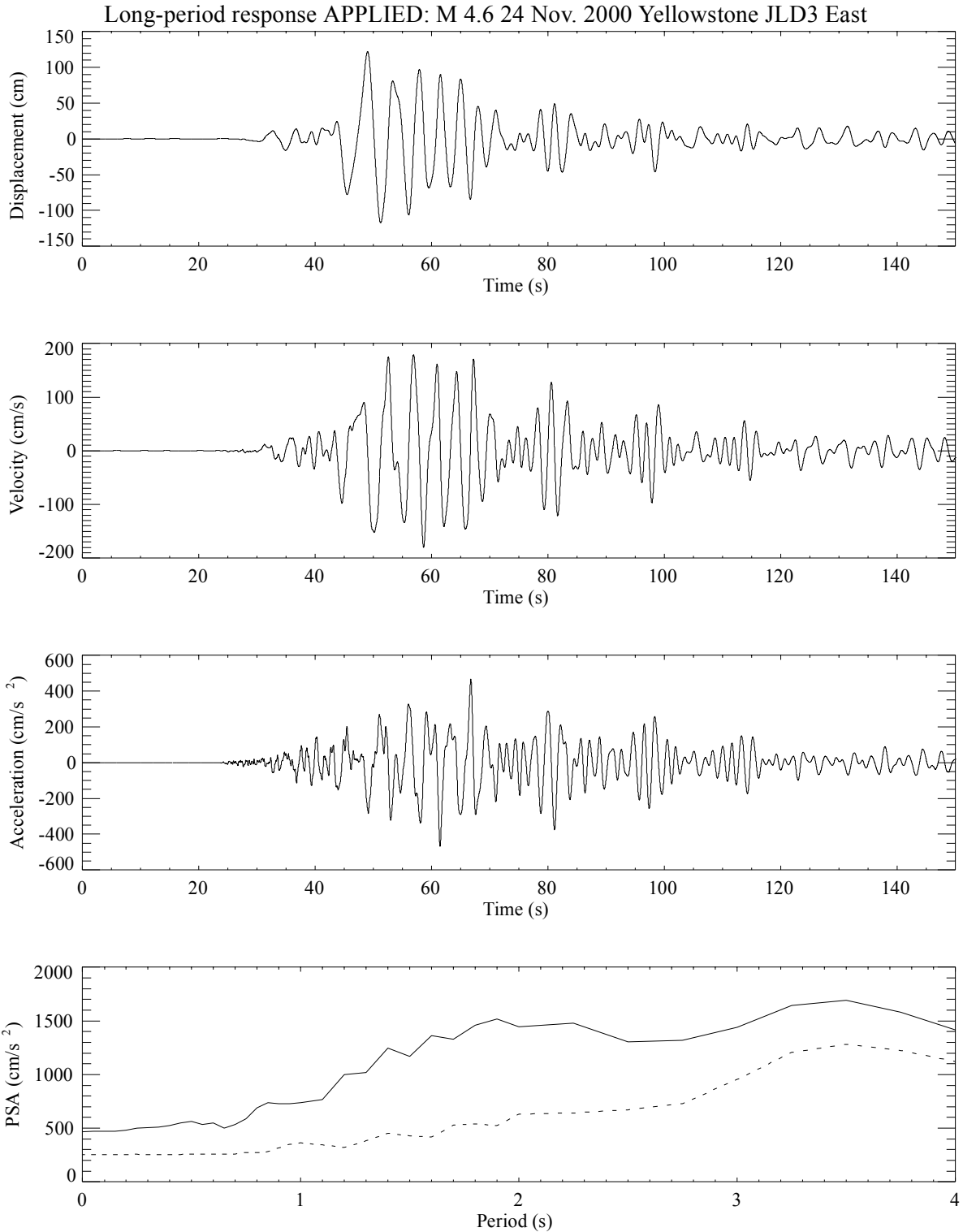


Figure 7-66: M 7.1 northern Teton fault earthquake simulation JLD3 north response. This is the total response obtained by combining the velocity seismograms from Figure 7-58 with (7-8).

characteristics for periods > 1 s to seismic waves incident from the southern Teton fault segment. The epicenters of these three earthquakes are shown in Figure 7-67. The vertical components of the EGF earthquakes in Table 7-4 have lower S/N relative to the horizontal components (Figure 7-68 and 7-69), limiting the usable period range to 0.5 s to 2 s for the vertical components, and 0.2 s to 3 s for the horizontal components. The **M** 3.7 earthquake of 29 January 2002 has higher S/N on all components (Figure 7-70), but is solely used to illustrate differential long-period responses with respect to the **M** 2.9 EGF, whose S/N limits the period band of comparison. The same rupture models used in Section 6 were used with the local earthquake EGF's to ascertain the influence of the Green's functions on estimated ground motions at site JLDW. A total of 3300 ground motion simulations were produced using each of the two local EGF's by varying hypocenter locations, asperity models, etc. in precisely the same manner as in Section 6. The EGF's for the **M** 2.9 11 July 1998 earthquake are limited in duration because the older digital recording system limited the total recording duration allowed for a single event (Figure 7-68). More complete (longer duration) recordings were obtained using the newer digital recording systems for the other two EGF earthquakes (Figures 7-69 and 7-70); record lengths for both these earthquakes exceed two minutes.

7.5.1 Simulated Ground Motions Using the 11 July 1998 M2.9 EGF's. The July 11, 1998 EGF event had an oblique normal-slip focal mechanism (Figure 7-71) and was located ~ 8 km south of site JLDW. The focal mechanism constraints on rake required including $> 30^\circ$ of strike-slip motion in the rake. This focal mechanism, azimuth, and takeoff angle produced an average *SV* radiation coefficient (0.21) at site JLDW about half of the average *SV* radiation coefficient for a northern segment Teton fault normal-slip earthquake on a 35-45°-dipping normal fault (0.44). Consequently, the EGF was scaled by a factor of two to produce an effective *SV* scaling consistent with the average radiation pattern on the northern segment of the Teton fault for site JLDW.

For the purposes of illustration, the simulated ground motion with acceleration response spectra closest to 84% quantile acceleration responses spectra (Figure 7-72) are shown in Figures 7-73 to 7-75. An L1 norm was used to find the synthetic ground motions with the smallest departure from the 84% quantile PSA in the period range of 0.5 s to 3 s. As expected the fault-normal component

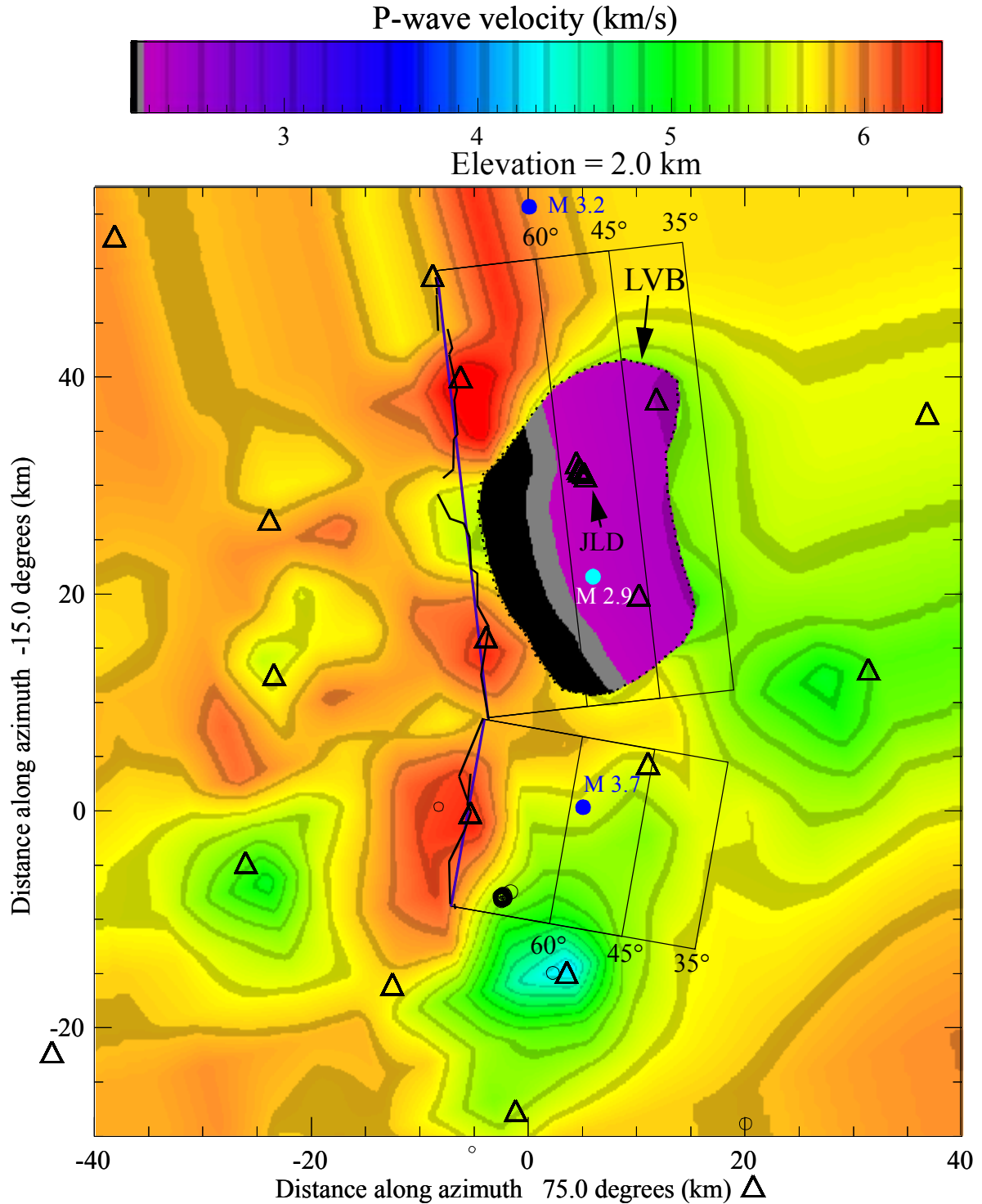


Figure 7-67: Epicenters of the three "broadband" EGF local earthquakes with P-wave 3D velocity model at elevation 2 km. Filled blue circles labeled with magnitudes are the EGF epicenters. Seismographic stations are triangles with the cluster of site-response stations at Jackson Lake Dam indicated as JLD. Solid rectangles are plan projections of the Teton fault segments for dips as labeled. Blue line segments show approximations to the surface traces of the Teton fault (irregular solid line segments). Closed dotted curve labeled LVB denotes the limits of the LVB.

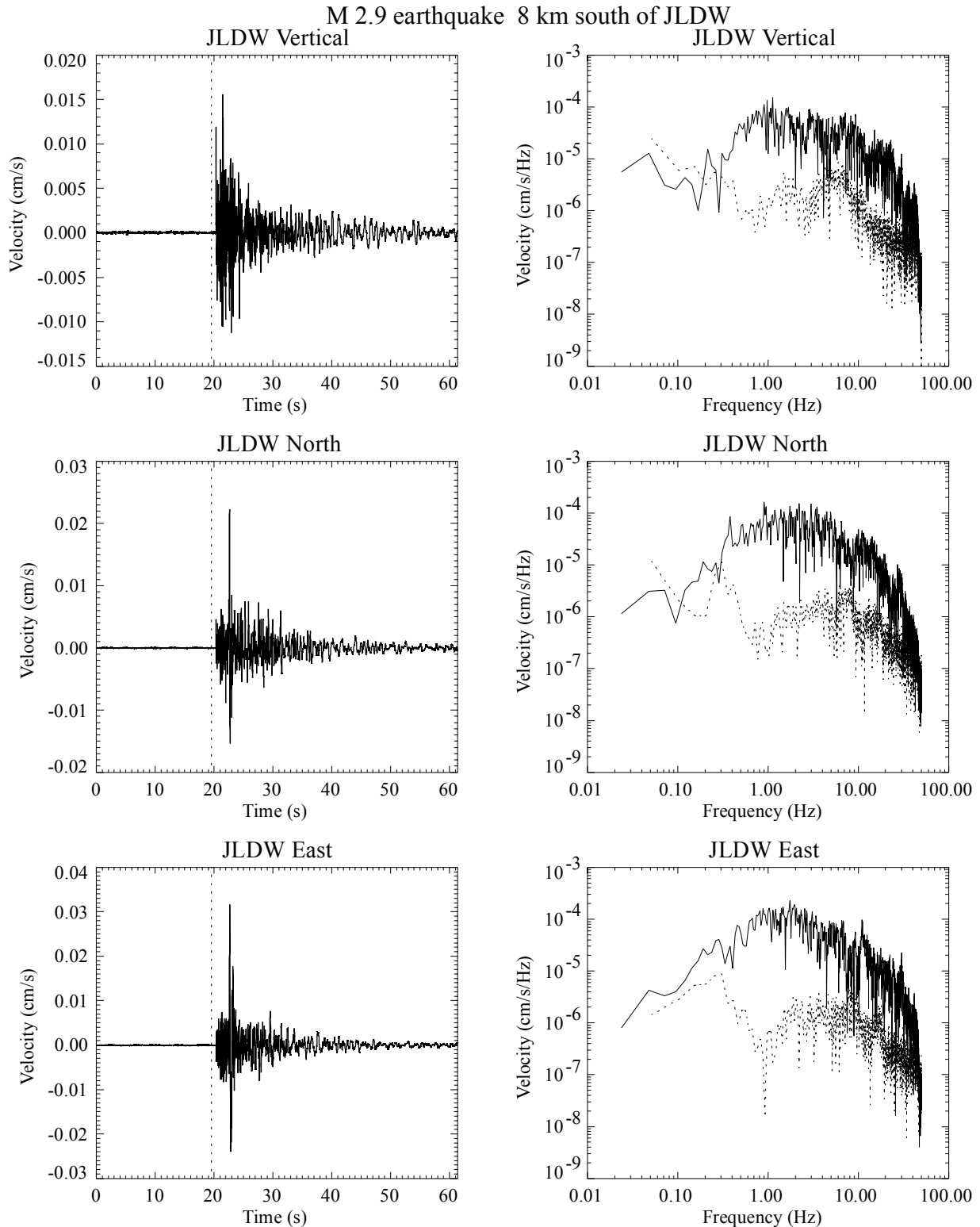


Figure 7-68: Site JLDW velocity seismograms and Fourier spectra from the M 2.9 11 July 1998 earthquake. The vertical dashed lines on the seismograms indicate the end time of the noise time windows (dashed curves in the Fourier spectra) and the signal windows (solid curves in the Fourier spectra). Epicenter is shown on Figure 7-67 and event information is in Table 7-4.

M 3.2 EGF earthquake 25 km north of JLDW

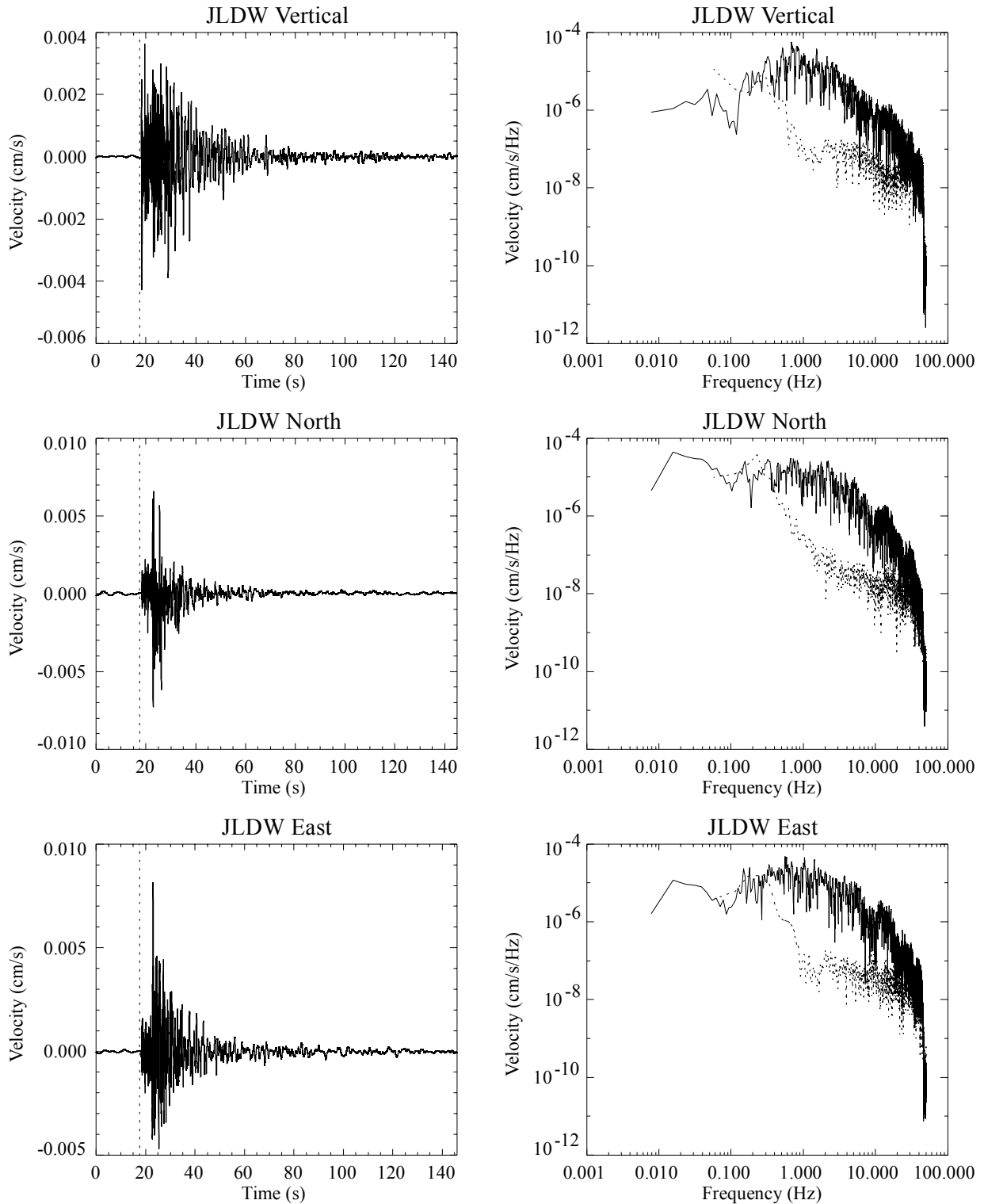


Figure 7-69: Site JLDW velocity seismograms and Fourier spectra from the **M** 3.2 20 November 2002 earthquake. The vertical dashed lines on the seismograms indicate the end time of the noise time windows (dashed curves in the Fourier spectra) and the signal windows (solid curves in the Fourier spectra). Epicenter is shown on Figure 7-67 and event information is in Table 7-4.

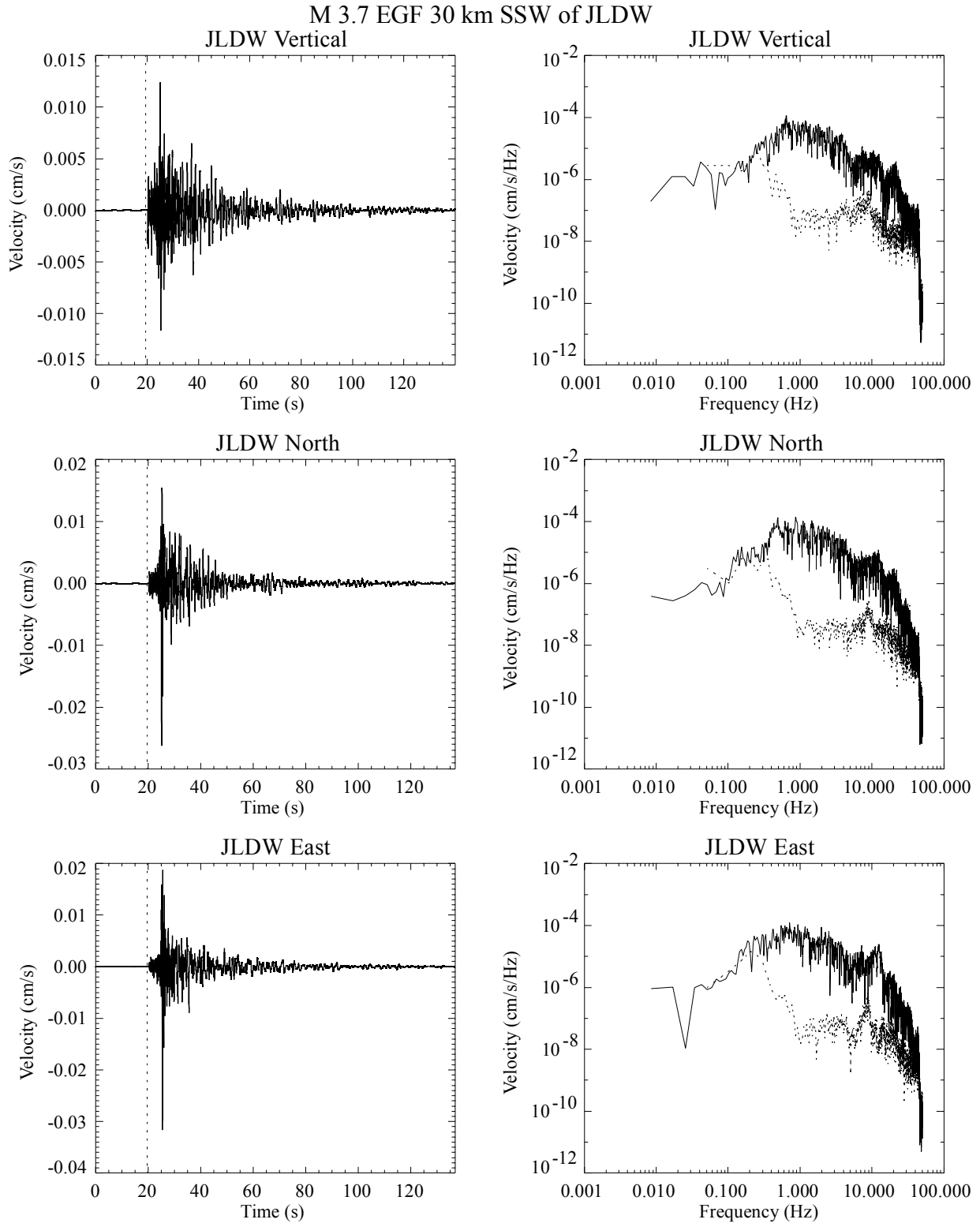


Figure 7-70: Site JLDW velocity seismograms and Fourier spectra from the M 3.7 29 January 2002 earthquake. The vertical dashed lines on the seismograms indicate the end time of the noise time windows (dashed curves in the Fourier spectra) and the signal windows (solid curves in the Fourier spectra). Epicenter is shown on Figure 7-67 and event information is in Table 7-4.

1998 0711 1610 03

Strike = 0 Dip = 45
Strike = 130 Dip = 57

43.782310 -110.58105 -5.75000

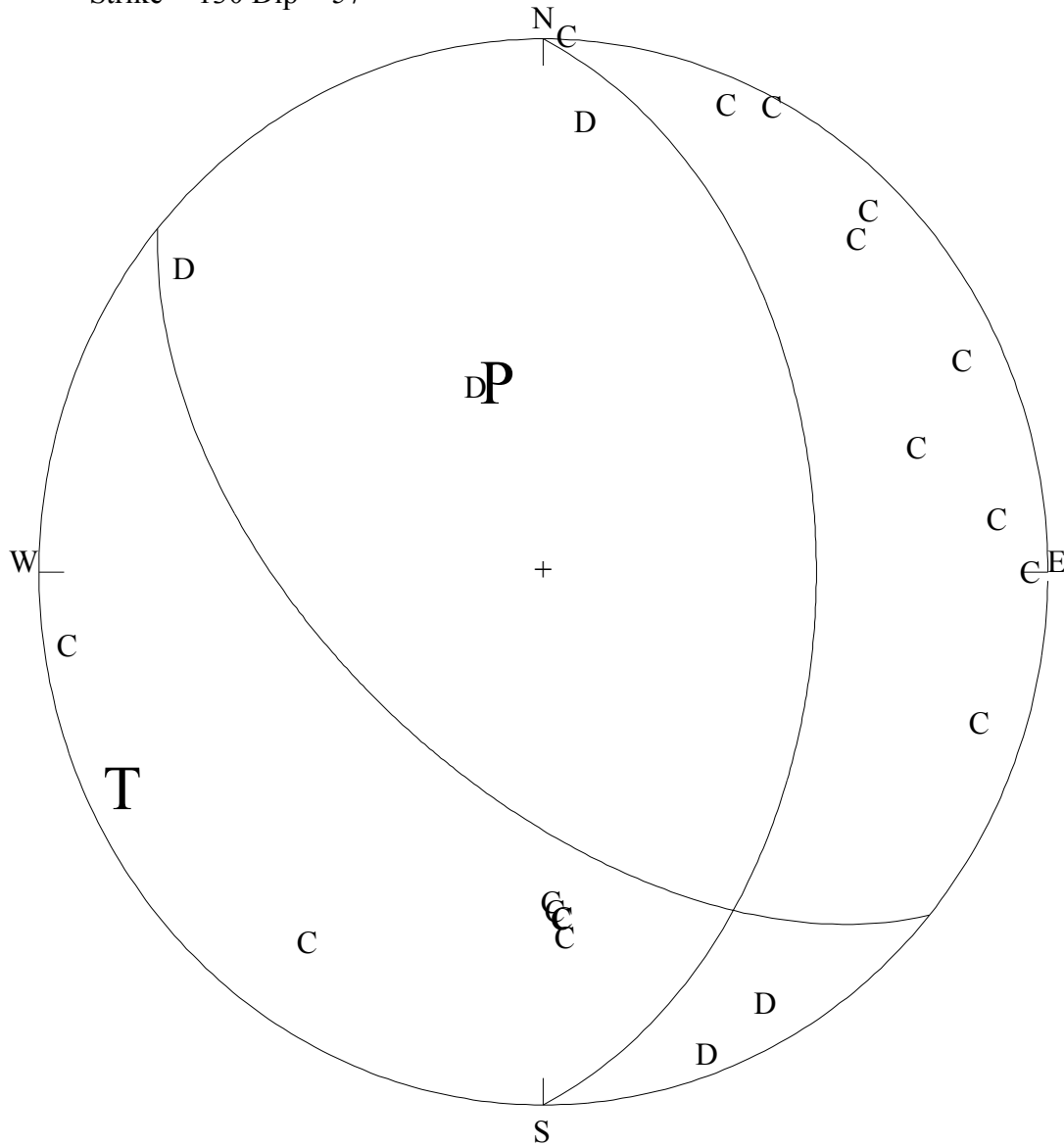


Figure 7-71: Focal mechanism for the M 2.9 EGF on 11 July 1998. Lower hemisphere projection with compressions (C) and dilatations (D), compressional (bold P) and tensile (bold T) axes, and P-wave nodal planes.

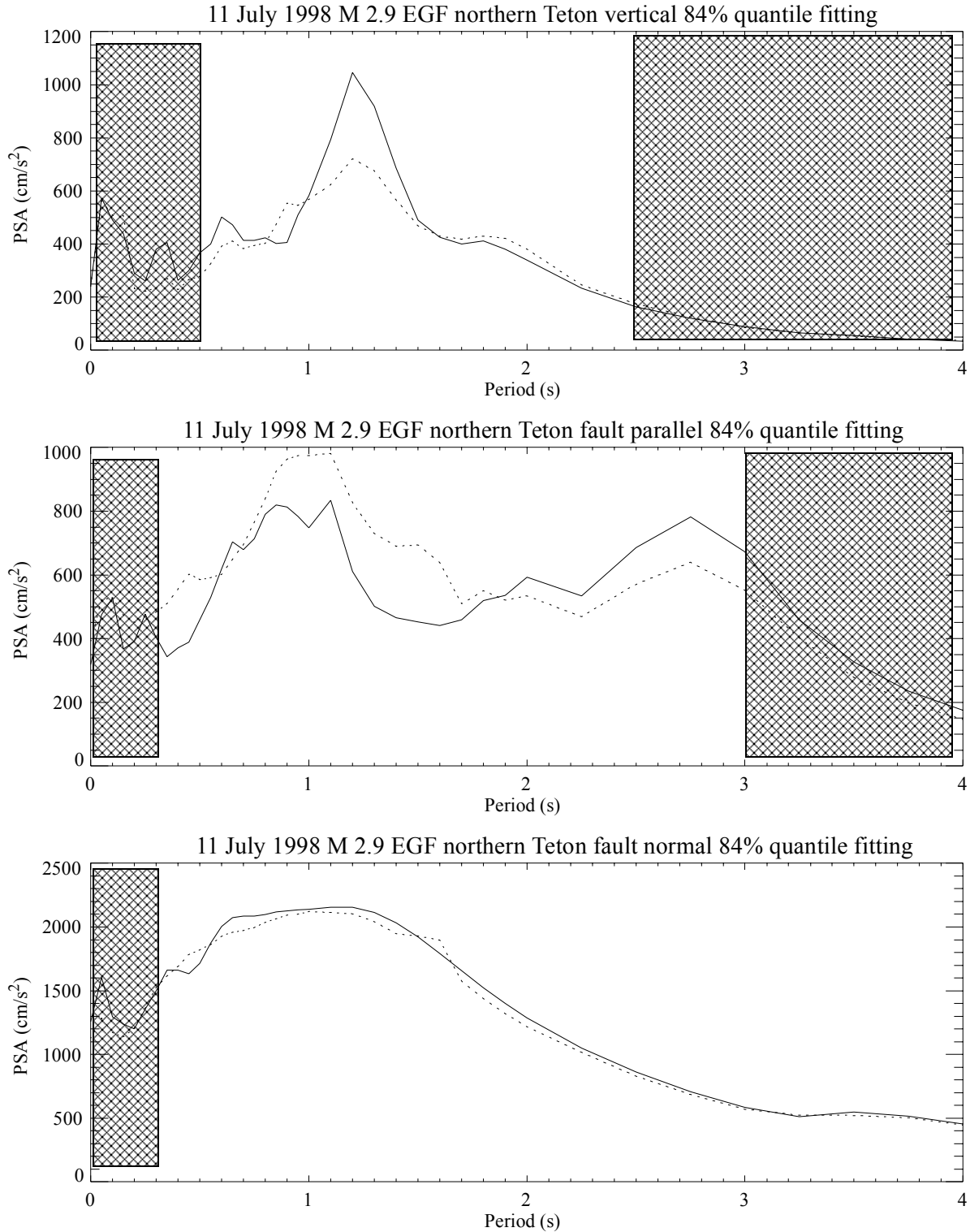


Figure 7-72: JLDW 84% quantile acceleration response spectra for the 11 July 1998 EGF. Dotted curves are 84% quantile response spectra from the 3300 northern Teton fault segment rupture simulations and solid curves are the response spectra from the best-fitting ground motion using an L1 norm for periods between 0.5 s and 3 s. Corresponding seismograms are shown in Figure 7-33 to 7-35. Hatched regions have inadequate S/N levels to interpret synthesized ground motions.

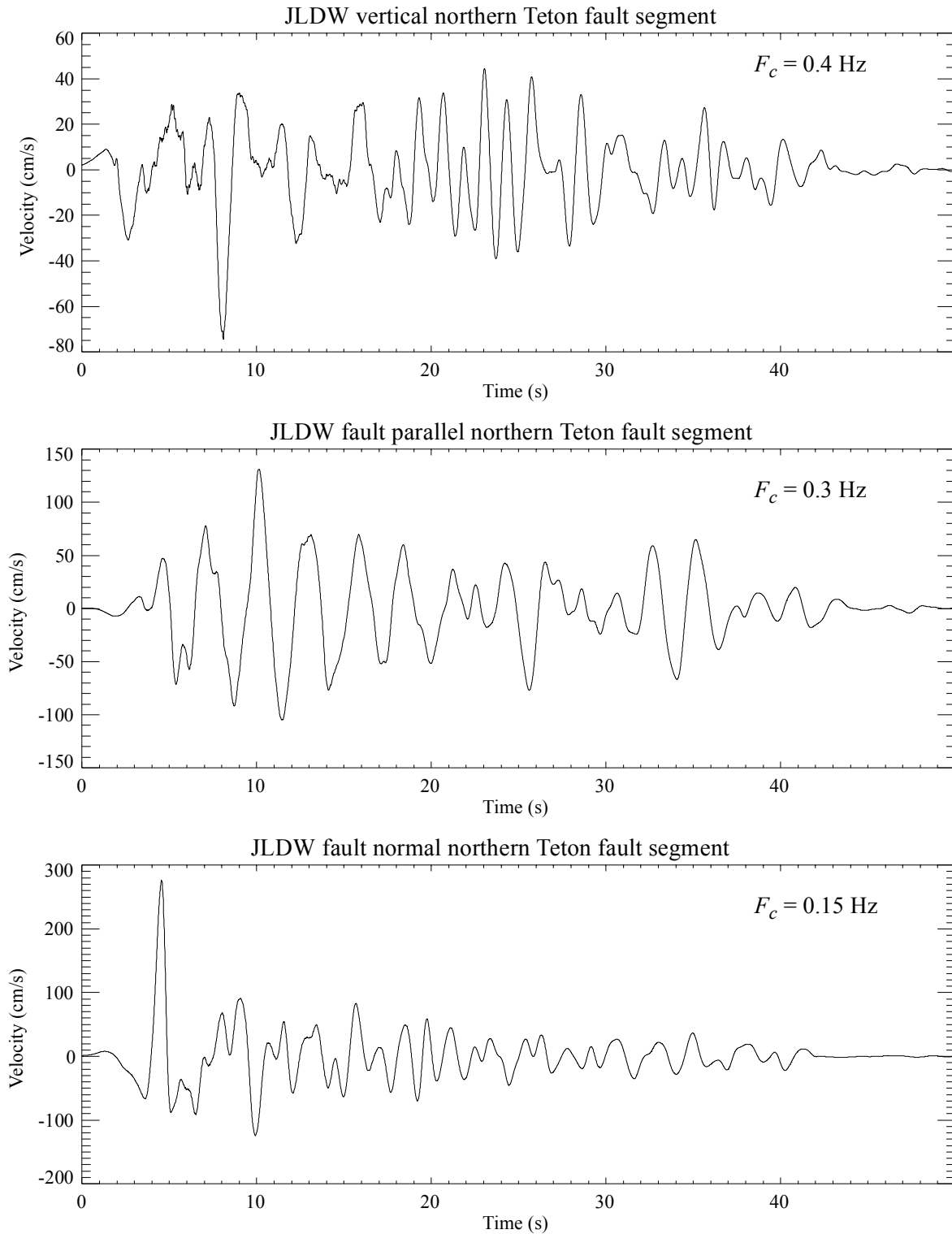


Figure 7-73: JLDW velocity seismograms for the best-fitting 84% quantile acceleration response spectra for the 11 July 1998 EGF. Note that the EGF were artificially truncated by the recording system, tapered to zero over the last 6 s of the seismograms during the simulation, and probably strongly underestimate the total duration of expected ground shaking. Also, signal-to-noise constraints dictated that the seismograms were high-pass filtered using corner frequencies as indicated on each

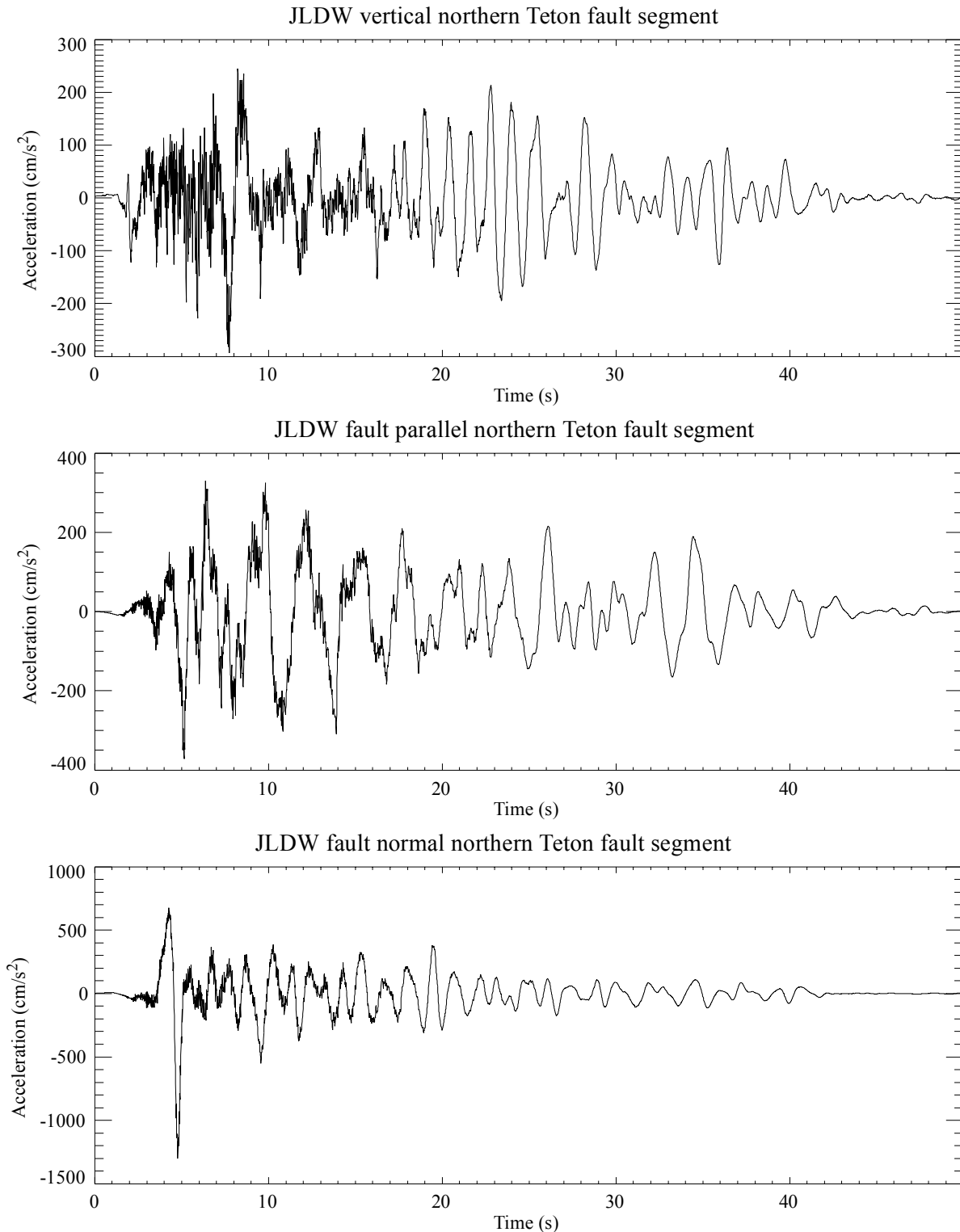


Figure 7-74: JLDW acceleration seismograms for the best-fitting 84% quantile acceleration response spectra for the 11 July 1998 EGF. Note that the EGF's were artificially truncated by the recording system, tapered to zero over the last 6 s of the seismograms during the simulation, and probably strongly underestimate the total duration of expected ground shaking.

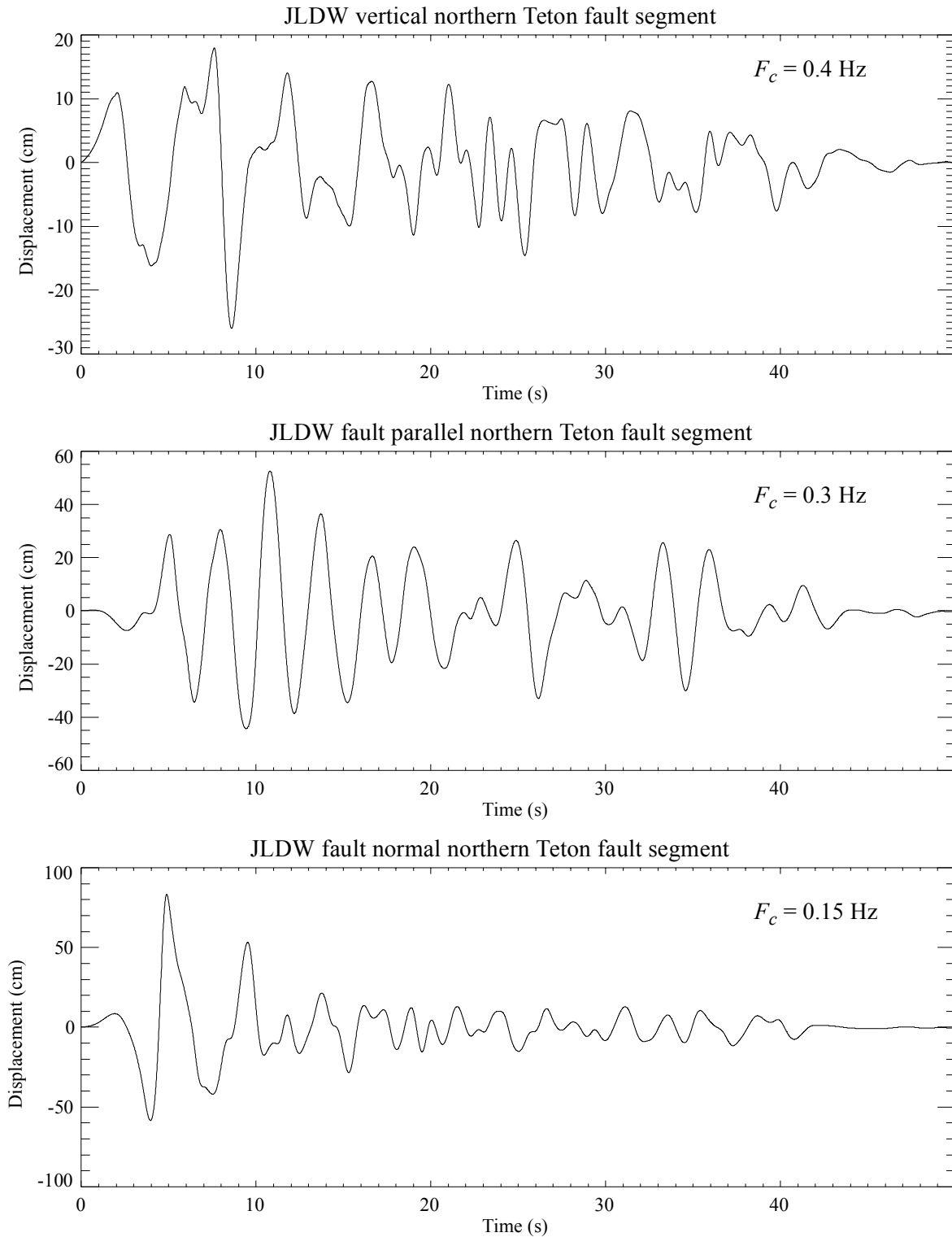


Figure 7-75: JLDW displacement seismograms for the best-fitting 84% quantile acceleration response spectra for the 11 July 1998 EGF. Static and long-period responses were eliminated by the high-pass filters. See Figure 7-73 for details.

has the largest peak velocity (Figure 7-73), but the fault-parallel and vertical components also have significant peak velocities with durations limited by the length of the EGF's. Strong accelerations associated with periods > 1 s are clearly evident throughout the acceleration seismograms, and dominate ground motions after times of about 20 s (Figure 7-74). The high-pass filtering necessitated by long-period noise limits interpretation of displacement seismograms (Figure 7-75). More detailed comparison of simulated ground motions to the hybrid ground motions of Section 6 is deferred to Section 7.5.4 below. Since the EGF's are clearly truncated, the only conclusion concerning duration is that strong ground shaking durations are likely to significantly exceed 40 s (length of the EGF's).

7.5.2 Simulated Ground Motions Using the 20 November 2002 M 3.2 EGF. This earthquake is located at the northern edge of the JLSN. Consequently, the focal mechanism is not well-constrained, but includes a normal-faulting component on planes striking roughly northeast. Constraints on focal mechanism rake are too weak to attempt to quantify shear-wave radiation, so the EGF's are used without any other scaling except simple distance corrections. Thus, it is advisable to put little credence in the absolute amplitudes, but instead limit interpretation to the general characteristics of the 0.5 s to 3 s period response range. Another significant caveat concerning this earthquake is that it is depleted of > 1 Hz shear-waves relative to all eight EGF earthquakes used in Section 6 and shown in Appendix D. Thus, the primary reason to use this earthquake's EGF's is to evaluate responses for periods > 1 s, a period range where S/N is too low to use the smaller magnitude EGF's in Appendix D.

Mean and 84% quantile acceleration responses show a strong spectral peak in the 1-2 s period range on all components (Figure 7-76) and weak acceleration responses for periods < 1 s. Shear-wave resonance within the low-velocity basin provides a possible explanation of the strong 1.3-1.8 s acceleration response in Figure 7-76. A local low-velocity basin thickness of 2-3 km and an average shear-wave velocity of 1.5 km/s could produce a quarter-wavelength resonance similar to the response in Figure 7-76, but does not explain the strong vertical component acceleration responses in the same period range. The simulated ground motions closest to the 84% acceleration response spectra (Figure 7-77) have the largest velocity responses on the north component (Figure 7-78), while vertical and fault-normal peak velocities are similar. It is possible that the fault-

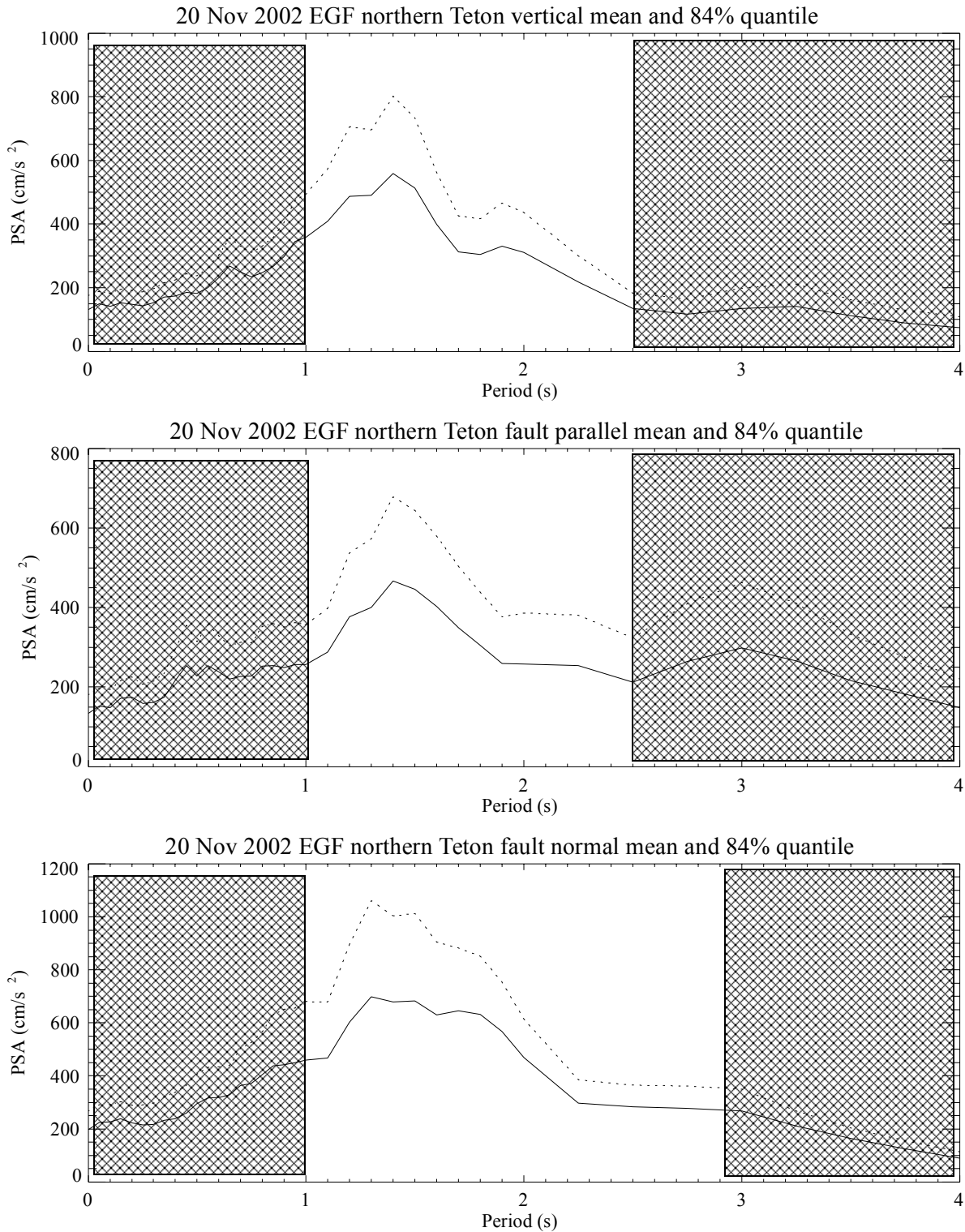


Figure 7-76: JLDW mean and 84% quantile northern Teton fault segment acceleration response spectra using the M 3.2 20 Nov. 2002 EGF. Dotted curves are 84% quantile response spectra and solid curves are corresponding means. Hatched areas are periods were noise levels are too large to warrant interpretation.

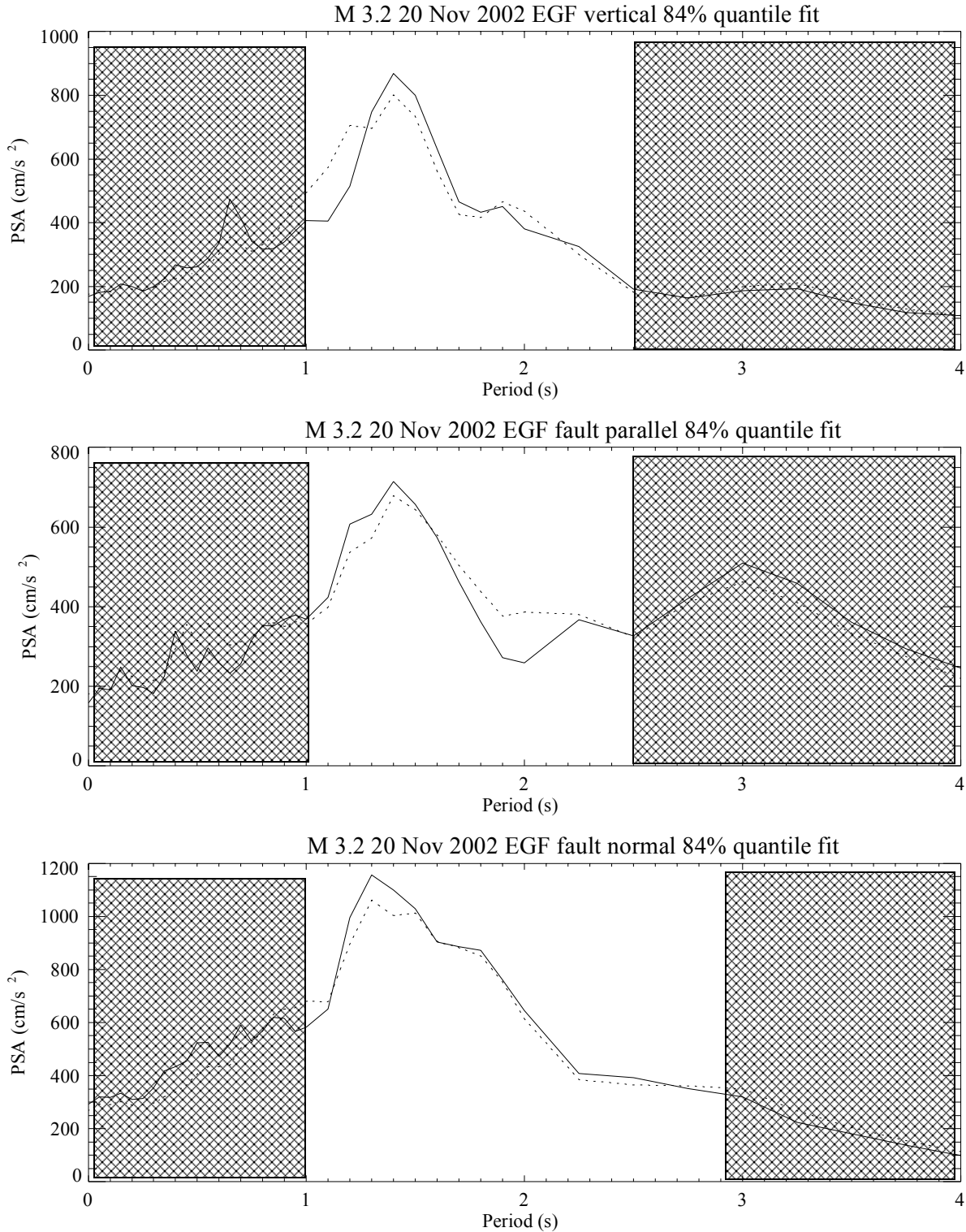


Figure 7-77: JLDW 84% quantile acceleration response spectra for the 20 Nov. 2002 EGF. Dotted curves are 84% quantile response spectra from the 3300 northern Teton fault segment rupture simulations and solid curves are the response spectra from the best-fitting ground motion using an L1 norm for periods between 0.5 s and 3 s. Corresponding seismograms are shown in Figure 7-38 to 7-40. Hatched areas are periods were noise levels are too large to warrant interpretation.

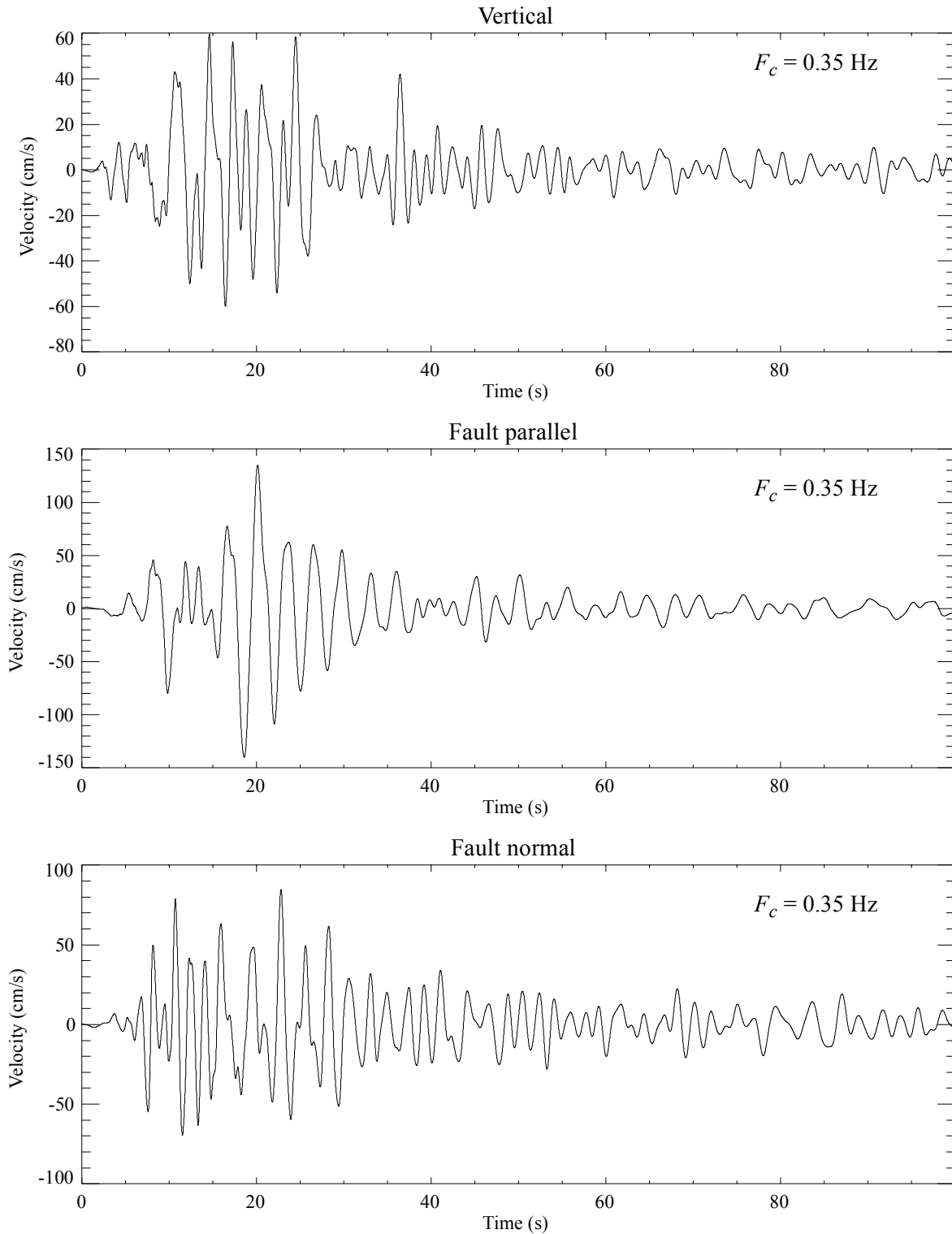


Figure 7-78: JLDW velocity seismograms for the best-fitting 84% quantile acceleration response spectra for the 20 Nov. 2002 EGF. Signal-to-noise constraints dictated that the seismograms were high-pass filtered using corner frequencies as indicated on each component.

parallel component has a significant basin-edge Love wave generated at the northwest basin boundary and that the vertical and fault-normal components are dominated by basin-edge induced Rayleigh waves. The peak acceleration responses of all the components is similar, although the fault-parallel component has a stronger response at longer periods (Figure 7-79). The ~ 3 s maximum period S/N-cutoff, limits interpretation of the displacement seismograms (Figure 7-80), although the lack of clear correlation between the vertical and fault-normal displacement seismograms argues against Rayleigh waves comprising a dominate phase on these ground motion components. The principal conclusion is that energy incident from the northern Teton fault segment north of the low-velocity basin appears to excite a very strong 1-2 s resonant response at the JLDW rock site. Given the already strong 1-2 s period acceleration responses observed at the JLD3 soil site associated with shallow soil resonances, this result suggests that energy from the northern end of the northern Teton fault segment may especially amplify ground motions in the 1-2 s period band for the embankment portion of the dam. Unfortunately, it appears that the fundamental resonant periods of basins at two entirely different spatial scales coincide, a situation that could produce unprecedented accelerations for periods > 1 s along the embankment section of the dam. Station JLD3 was no longer operating and did not record the 20 Nov. 2002 earthquake, so a direct estimate of the impact of overlapping multi-basin resonant responses on long-period acceleration responses for the embankment portion of the dam using EGF's is not possible.

7.5.3 Influence of EGF Location on Long-Period Responses. Another way to ascertain the influence of incident direction on ground motions at the dam is to ratio acceleration response spectra of the more distant EGF's from the dam (the **M** 3.2 and **M** 3.7 earthquakes 20 north and 30 km SSW, respectively, see Figure 7-67) using the **M** 2.9 earthquake EGF's as a reference. There are a number of ways to attempt to correct for differences in distances, radiation patterns, etc., but for the sake of simplicity each component EGF was normalized to a peak velocity of one prior to calculating the PSA ratios. This serves to illustrate the differences in long-period responses relative to consistent scaling of peak shear-wave amplitudes. All components of the **M** 3.2 earthquake north of JLDW are amplified for periods of 1-2 s (Figure 7-81), but the vertical component shows the strongest amplification. The uniform amplification of vertical motions relative to a nearby earthquake sources makes intuitive sense, since incident angles

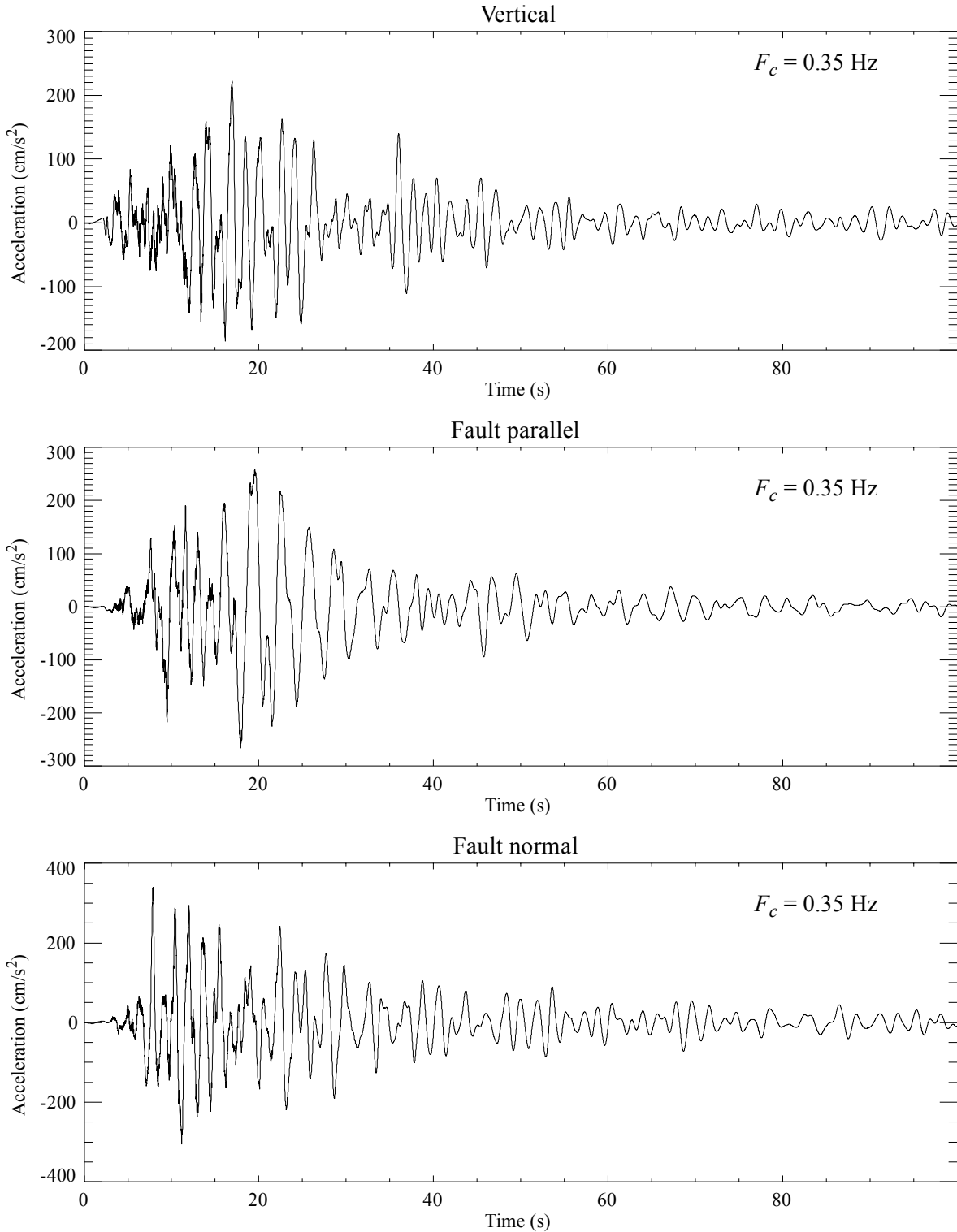


Figure 7-79: JLDW acceleration seismograms for the best-fitting 84% quantile acceleration response spectra for the 20 Nov. 2002 EGF. Signal-to-noise constraints dictated that the seismograms were high-pass filtered using corner frequencies as indicated on each component.

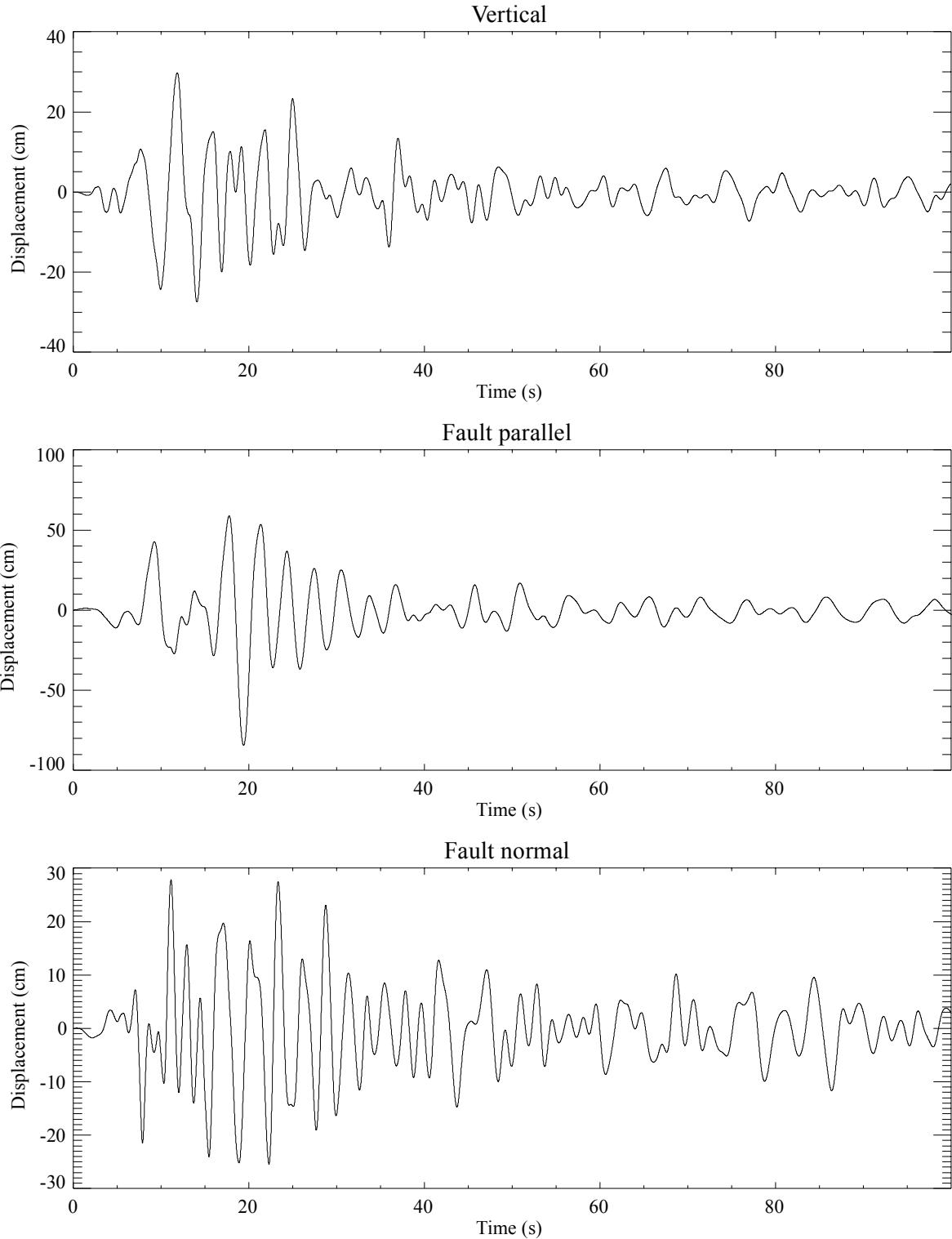


Figure 7-80: JLDW displacement seismograms for the best-fitting 84% quantile acceleration response spectra for the 20 Nov 2002 EGF. Static and long-period responses were eliminated by the high-pass filters. See Figure 7-78 for details.

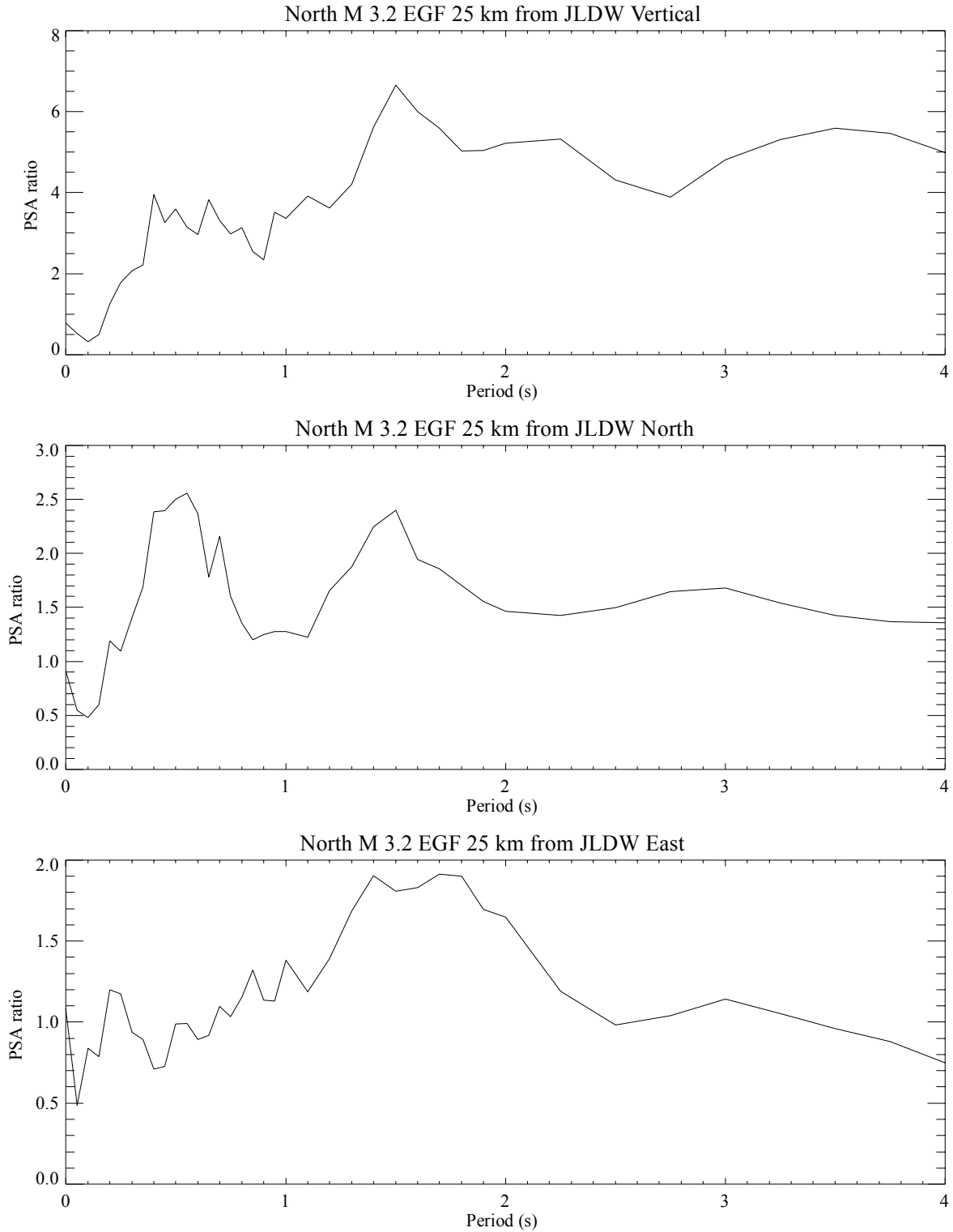


Figure 7-81: JLDW PSA ratios of the **M** 3.2 EGF ground motions to the **M** 2.9 EGF ground motions. The **M** 3.2 earthquake was located about 25 km north of site JLDW (Figure 7-67). Each component was normalized to a peak velocity of 1 cm/s prior to calculating the PSA ratios.

decrease with increasing distance and the opportunities for phase conversion between body waves and surface waves increases with distance. The north component is uniformly amplified at periods > 1 s, but the east component is only strongly amplified for periods of 1-2.4 s (Figure 7-81). In contrast, the north component from the M 3.7 earthquake to the SSW of site JLDW is only amplified for periods of 1-3 s (Figure 7-82) and the east component does not show any long-period amplification. The portion of the low-velocity basin south of the dam is postulated in Section 4 to shallow toward the south. The amplification cutoff at a period of 3 s period in Figure 7-82 is consistent with estimated basin thickness of ~ 3 km beneath the dam. The progressive shallowing of the basin to the south would reduce amplification periods which could explain the broad amplification for periods extend down to 1 s on the north component in Figure 7-82. The vertical component is amplified at all periods, consistent with expectations.

7.6 Comparison to Broadband Hybrid Ground Motions From Section 6.

For the purposes of comparison with Section 6 estimated ground motions a single dip scenario (35°) and the only broadband local earthquake EGF that could be associated with the northern Teton fault segment (the M 2.9 earthquake, 8 km south of JLDW in Table 7-4) were used to synthesize ground motions using the same 3300 rupture scenarios used in Section 6.4.3. Table 7-5 shows the differences in peak velocities between the hybrid Green's function estimates of Section 6 and the purely empirical Green's function estimates using the single earthquake EGF. The EGF

Table 7-5: JLDW Rock Ground Motion Parameters: 35° -Dipping Northern Teton Fault Segment.

Component	EGF peak velocity	Hybrid peak velocity
	(cm/s)	(cm/s)
fault-normal (E15S) mean	184	146
fault-normal (E15S) 84%	252	201
fault-parallel (N15E) mean	74	102
fault-parallel (N15E) 84%	108	135
Vertical mean	31	125
Vertical 84%	62	147

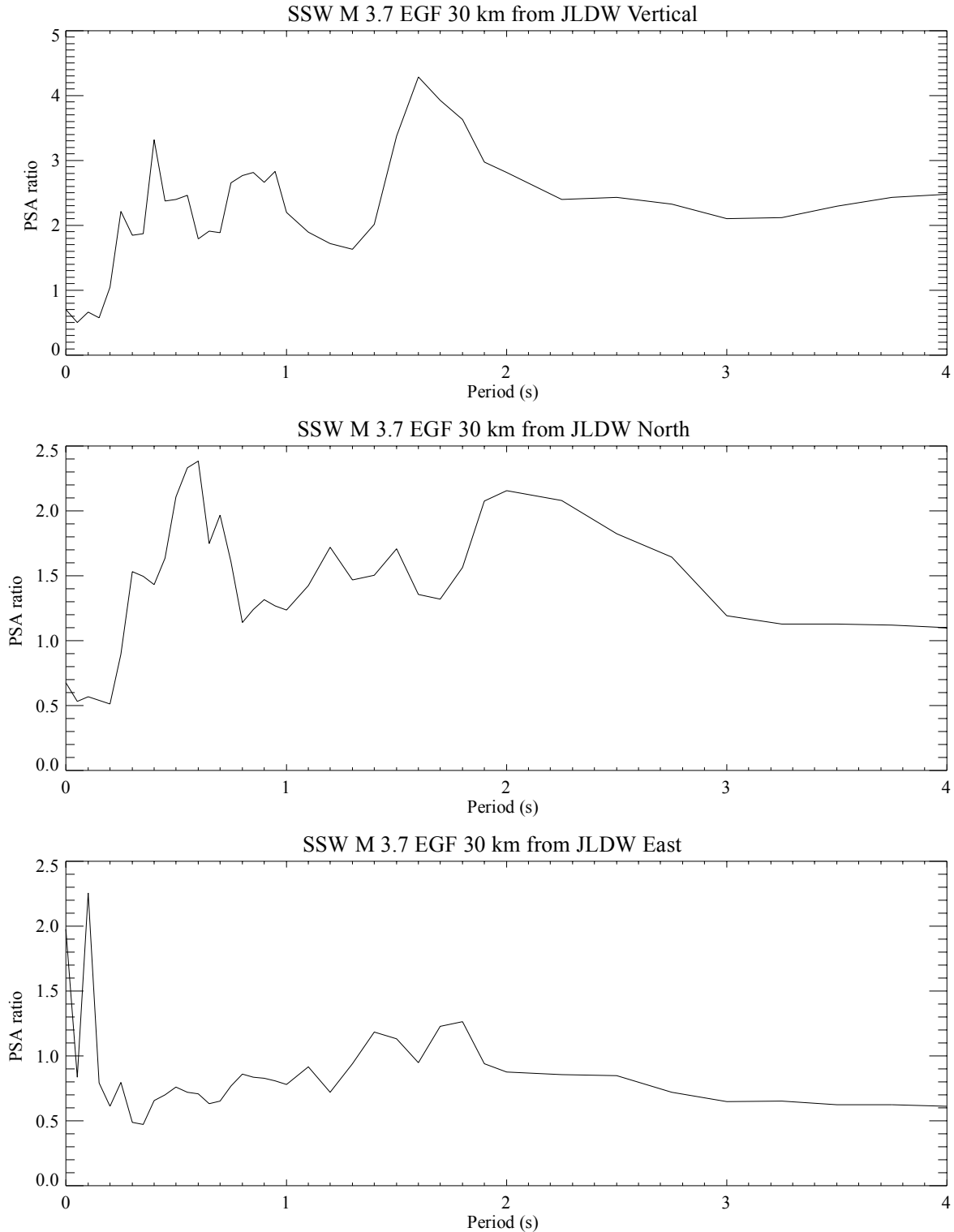


Figure 7-82: JLDW PSA ratios of the **M** 3.7 EGF ground motions to the **M** 2.9 EGF ground motions. The **M** 3.7 earthquake was located about 30 km SSW of site JLDW (Figure 7-67). Each component was normalized to a peak velocity of 1 cm/s prior to calculating the PSA ratios.

fault-normal peak velocities are somewhat larger than the hybrid fault-normal peak velocities because the EGF's indicate a stronger long-period response (Figures 7-83 and 7-84). Fault-parallel EGF peak velocities are about 30% smaller than hybrid estimates (Table 7-5). EGF vertical peak velocities are much smaller than hybrid peak velocities (Table 7-5)..

In light of the findings in Section 7.4 and 7.5 that energy from the ends of the Teton fault is likely to strongly amplify fault-parallel and vertical responses relative to energy radiated from the middle of the fault, the single-earthquake EGF estimates of fault-parallel and vertical peak velocities in Table 7-5 are probably lower bounds. Conversely, based on the results of Sections 7.4 and 7.5 it appears that the **M** 2.9 EGF will somewhat overestimate fault-normal responses for energy arriving from the ends of the northern Teton fault segment, so fault-normal single-earthquake EGF peak velocities in Table 7-5 are probably overestimated.

Even more so than the mean (Figure 7-83) and 84% (Figure 7-84) E15S Section 6 hybrid acceleration response spectra, the single-earthquake EGF spectra exhibit responses more similar to soil responses from the Spudich et al. (1999) extensional acceleration attenuation relations than rock responses. Direct comparison of the single-earthquake EGF 84% quantile spectra and the **M** 5.2 Idaho earthquake EGF spectra with the hybrid ground motion spectra from Section 6 (Figure 7-85) indicates that the hybrid ground motions probably provide realistic acceleration responses for most periods with three significant caveats. First, it appears that the hybrid ground motions overpredict vertical accelerations for periods > 2 s (Figure 7-85). Second, the hybrid horizontal acceleration responses for periods from ~ 0.8 s to 1.5-2 s may be underestimated. Third, hybrid ground motion durations are probably too short and lack prolonged periods (~ 40 s) of substantial ground shaking with sustained peak velocities > 70 cm/s and sustained peak accelerations > 0.2 g for rock site conditions and sustained peak accelerations exceeding 0.25 g along the embankment section for more than 70 s.

The very-strong acceleration responses in Figures 7-83 to 7-85 for periods of 1-3 s are consistent with trapped-wave resonances in the low-velocity basin for basin thicknesses varying between 2-4 km. Figure 7-86 provides a schematic illustration of the first-order factors influencing the how the low-velocity basins beneath Jackson Lake dam amplifies seismic energy and prolong ground-

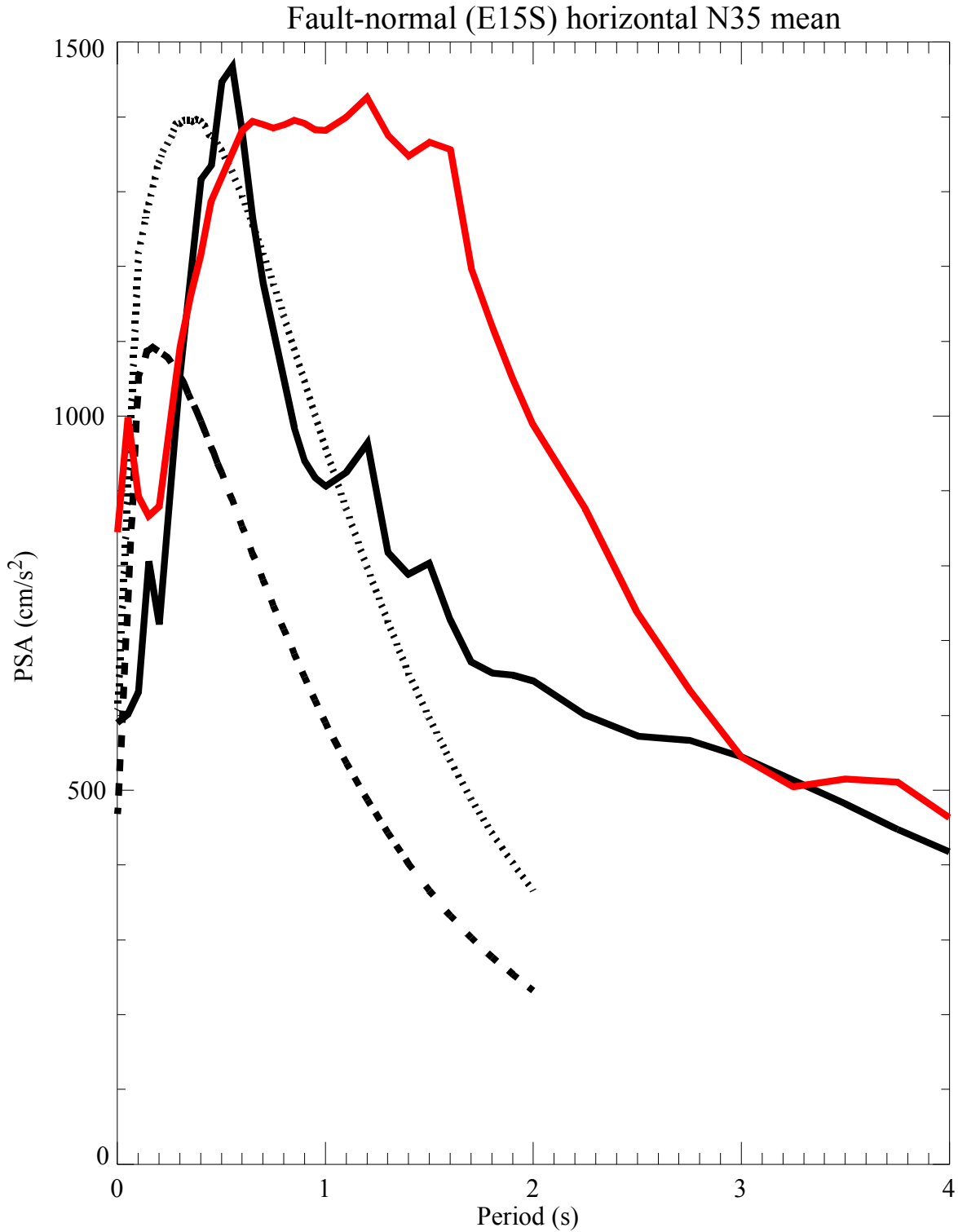


Figure 7-83: JLDW rock site mean downstream horizontal PSA response spectra for a 35°-dipping northern Teton fault segment (solid). SEA99 average horizontal component estimates for a M 7.0 normal-faulting earthquake are shown for soil (dotted) and rock (dashed) site conditions. Red curve are the mean spectra using the M 2.9 earthquake EGF.

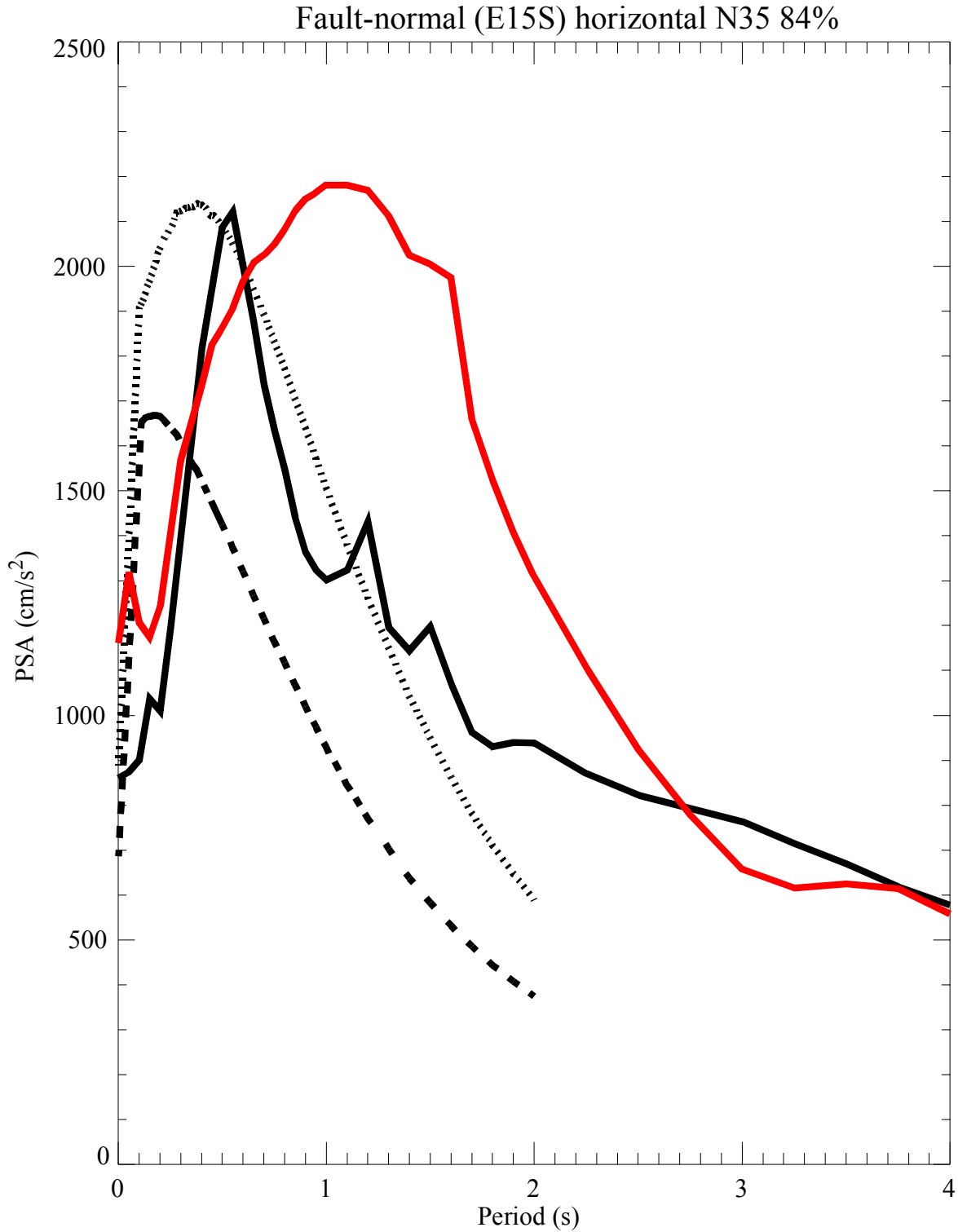


Figure 7-84: JLDW rock site hybrid Section 6 84% quantile downstream horizontal PSA response spectra for a 35°-dipping northern Teton fault segment (solid). SEA99 average horizontal component estimates for a M 7.0 normal-faulting earthquake are shown for soil (dotted) and rock (dashed) site conditions. Red curve are the 84% quantiles using the M 2.9 earthquake EGF.

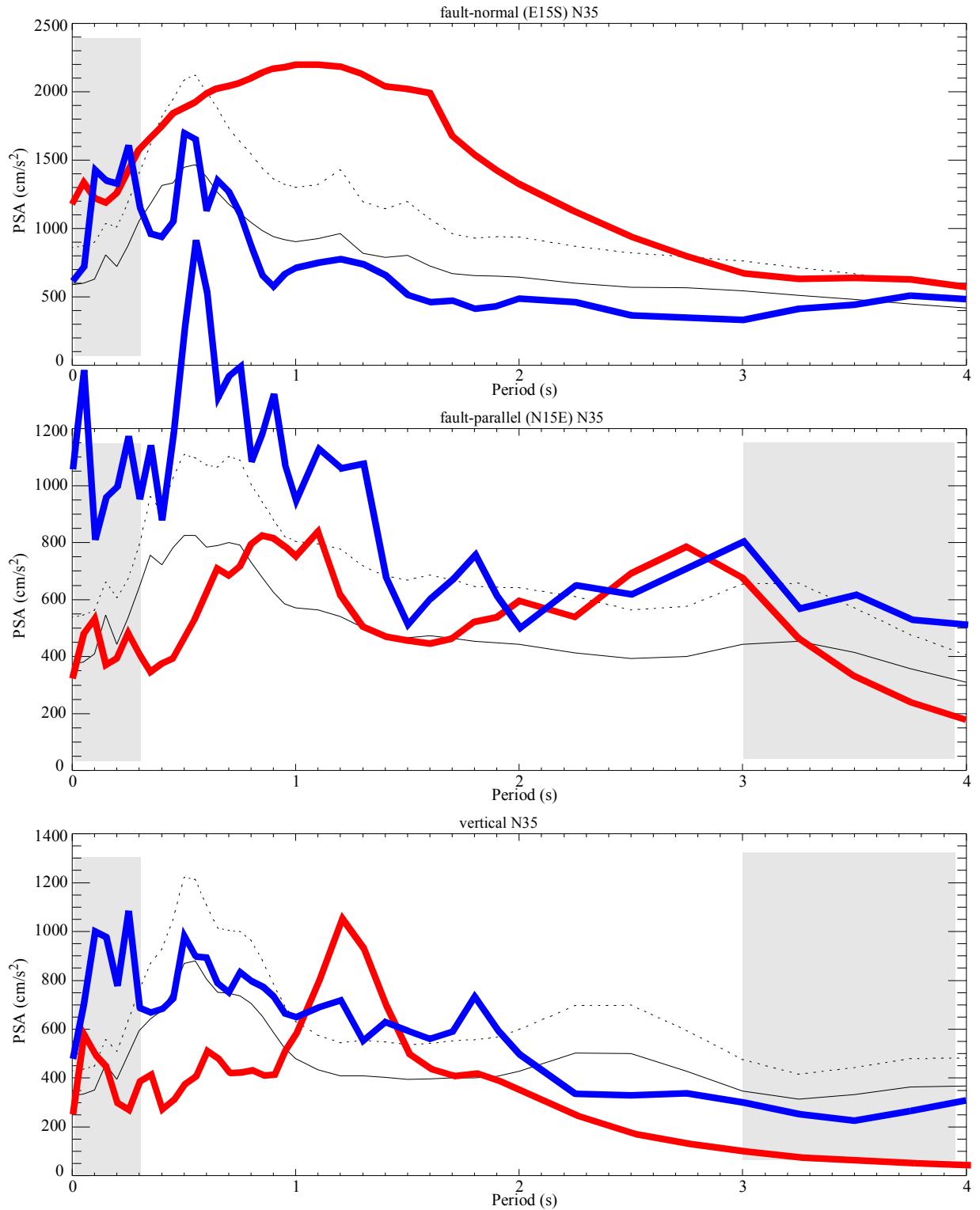


Figure 7-85: JLDW rock site hybrid Section 6 PSA response spectra for a 35°-dipping northern Teton fault segment for all hypocenters. Mean hybrid curves are solid, 84% hybrid quantile curves are dotted, local **M** 2.9 broadband EGF 84% quantile curves are red, and **M** 5.2 Idaho EGF PSA spectra are blue curves. Components are as labeled.

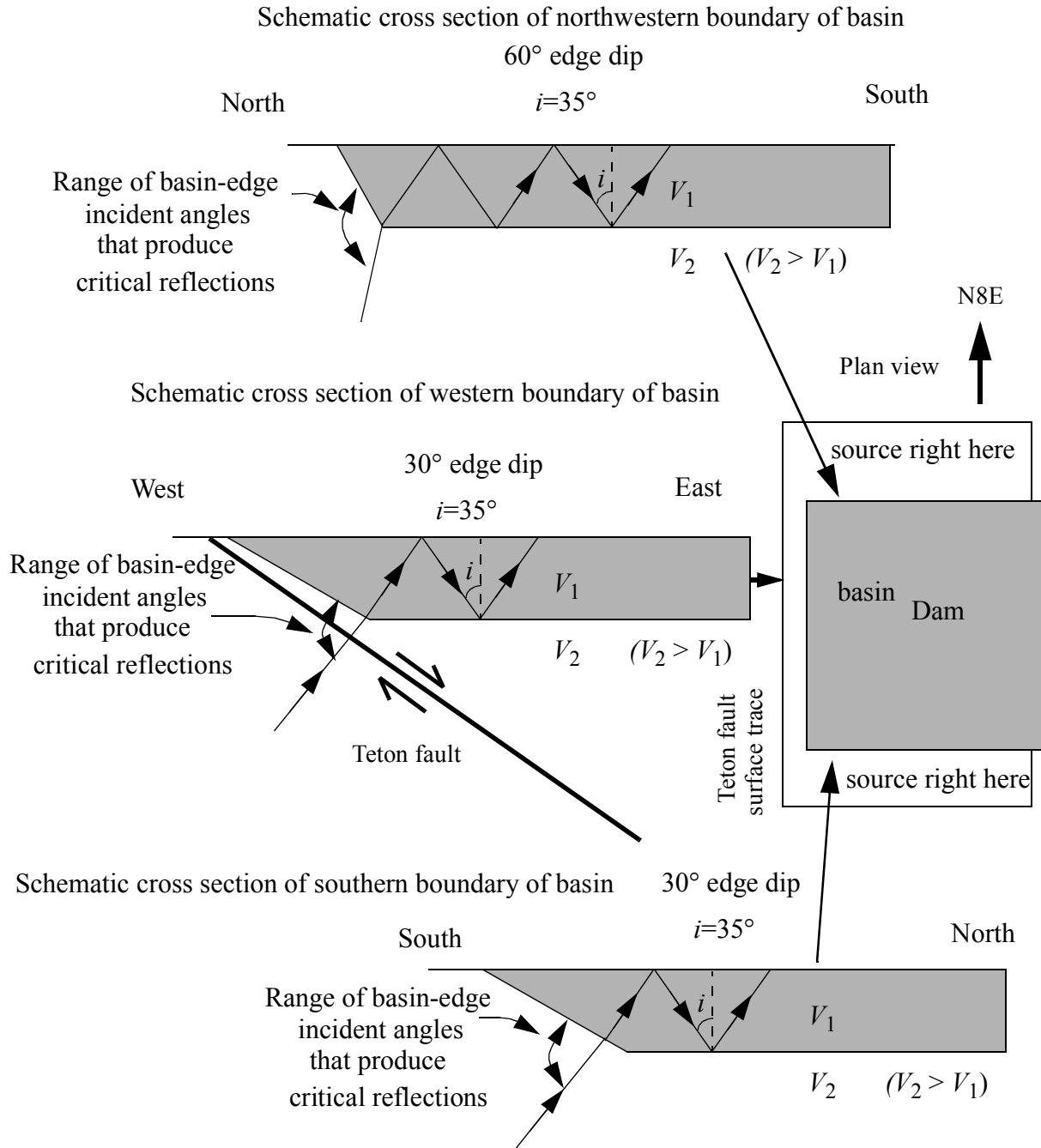


Figure 7-86: Schematic plan and cross section views of the low-velocity basin boundary configuration for Jackson Lake Dam. Basin indicated by shaded regions. Open rectangle is the outline of the northern segment of the Teton fault in the plan view. Uniform shear velocities used for illustration of $V_1 = 2$ km/s and $V_2 = 3.5$ km/s, producing a critical angle (i) of 35° . Unlike the basins considered by Somerville et al. (2003) that were generally located more than 5 km from one edge of basins, the Teton fault is in close proximity to three edges of the low-velocity basin containing Jackson Lake Dam.

shaking durations. The northwestern boundary traps nearly all the waves incident to the 60° boundary as critical reflections within the basin. This explains why the Yellowstone earthquake and **M** 3.2 earthquake 25 km north of the dam produce such strong long-period acceleration responses and long durations of strong ground shaking. The western boundary critically traps all waves incident from the nearby portion of the fault plus a portion of the fault below the basin, but does not trap steeply incident wave energy as effectively as the northwestern margin of the low-velocity basin. The southern boundary critically traps waves incident from the western portion of the Teton fault that extends south of the southern basin boundary, but does not trap steeply incident wave energy as effectively as the northwestern margin of the low-velocity basin. This partially explains why the **M** 5.2 Idaho earthquake and **M** 3.7 southern Teton fault segment earthquake produce less long-period amplification at the dam than the earthquakes north of the low-velocity basin. The situation at Jackson Lake Dam has two factors that appear to strongly influence basin amplification. The relatively high shear-wave velocity of the basement rocks (~ 3.5 km/s) at relatively shallow depths (2-3 km) produce a small critical angle of $\sim 35^\circ$ and a shorter period resonance (1-3 s) than comparatively deeper basins in California (San Fernando and Los Angeles). There are several significant departures of Figure 7-86 from the schematic of Somerville et al. (2003) that inspired it. First, the steep dip of the northwestern portion of the basin causes nearly all incident energy from the north at nearly all incident angles to be critically-reflected within the basin. Second, Teton fault is embedded in high-velocity rocks very close to the basin (only 1-2 km from the basin boundary) and parallels the basin edge for more than 10 km, a configuration not present in the basin configurations considered by Somerville et al. (2003). All these factors and results of the ground motion simulations in Sections 6 and 7 lead to the conclusion that basin amplification and durations effects are likely to be stronger in the low-velocity basin containing Jackson Lake Dam than any basin ground motion experience to date. This is a result of the combined compounding effects of unusually large amplification of ground motions by the low-velocity basin, basin-margin velocity structure, the location of the embankment portion of the dam in an extremely low-velocity-basin embedded in a larger basin with nearly identical fundamental mode resonant periods, the close proximity of the Teton fault to the basin, and the Teton fault extending to the surface through high-velocity rocks within 1-2 km of the western edge of the low-velocity basin.

7.7 Discussion.

Somerville (2003) identified two aspects of the simulated ground motions in Section 6 that warranted further investigation, the validity of the kinematic source model and verification of basin response and its significance to estimate ground motions. The kinematic source model in Section 6 was shown in Section 7.2 to reproduce near-source Northridge ground motions and their associated statistical properties. An alternative source model (Frankel, 1995) produced ground motions similar to Section 6. The estimated ground motions appear relatively insensitive to details of rupture model specifications. Ground motion amplitudes are most sensitive to assumed stress drop. A mean stress drop of 3.4 Mpa (34 bars) was used in Section 6 to produce rupture models for the northern Teton fault segment and are consistent with stress drops associated with Basin and Range earthquakes. Mayeda and Walter (1996) estimated stress drops in the western United States using regional coda envelopes with corrections for attenuation. Their mean dynamic stress drop for Basin and Range earthquakes was 3.0 Mpa (30 bars). Ichinose et al. (1997) found stress drops of ~ 6.0 MPa (60 bars) for a normal-faulting earthquake sequence near Reno, Nevada, that contained a **M** 4.5 mainshock. Doser (1986) estimated stress drops of 6-7 MPa (60-70 bars) for the three **M** > 6 normal-faulting earthquakes in the Fairview Peak-Dixie Valley, Nevada, earthquake sequence. Boatwright (1985) estimated dynamic stress drops 3.3 ± 1.6 MPa (33 ± 16 bars) and 7.7 ± 5.2 MPa (77 ± 52 bars) for aftershocks from two segment of the 1983 **M** 7.0 Borah Peak, Idaho, earthquake. Mayeda and Walter (1996) find a tendency for dynamic stress drops to increase with magnitude in the western United States and suggest that mean dynamic stress drops of 3.0 MPa (30 bars) may underestimate dynamic stress drops of **M** 6.6-7.3 earthquakes in the western United States. Thus, while the mean dynamic stress drop of 3.4 MPA (34 bars) used in Section 6 appears reasonable, the regional stress drop results of Boatwright (1985), Doser (1986), Mayeda and Walter (1996), and Ichonese et al. (1997) indicate that higher mean stress drops may warrant consideration for estimating ground motions at Jackson Lake Dam. Thus, stress drop and kinematic rupture models can be eliminated as potential biases that would overestimate ground motions at Jackson Lake Dam. Borah Peak eyewitnesses accounts require significant stress drops near the surface because surface-rupture rise times were 1-2 s. Near-surface stress drops comparable to the Borah Peak earthquake are likely to produce ground motions larger than estimated in this report because shallow stress drops were tapered to small values as the fault

approached the surface in the kinematic rupture models. The Teton fault is located within 1-2 km of the ~10-km-long basin-edge caustic region for the dam and slip-velocities of 50-100 cm/s would experience limited geometric spreading before entering the western edge of the low-velocity basin, where significant amplification would occur due to the extreme velocity contrast between basement rocks and low-velocity basin rocks.

The dip of the Teton fault is probably the largest remaining unresolved uncertainty in the seismic source specifications that strongly influences estimated ground motions at the dam. The spatial distribution of hypocenters favors a dip of 35° (Section 3). The few well-constrained focal mechanisms have widely ranging normal-faulting dips from 30° to 60°. The emergence of a relatively new normal fault several km west of the large-scale Teton fault with a steep dip of 60-70° (Section 2) suggests that the current large-scale Teton fault may be approaching unfavorably low dips for continued normal faulting. Thus, the only available information specific to the Teton fault argues for a fault dip of 35° to 40°. In lieu of any other specific information about the dip of the Teton fault at depth, a fault dip of 35° is considered the most reasonable estimate for the northern Teton fault segment. More specifically, higher dips are not considered reasonable estimates. Since the global normal-fault database allows for dips ranging from 25° to 70°, appealing to dips found on other normal faults as evidence for what the dip on the Teton fault “should be” are not compelling or informative. Obviously, if new information becomes available to show that the northern Teton fault segment has dips of 45° or greater, then seismic loadings for Jackson Lake Dam will need to be revised. For now the ground motions estimated using a Teton fault dip of 35° are recommended for dynamic analyses of Jackson Lake Dam.

Purely empirical Green’s function approaches were used in Sections 7.4 and 7.5 to produce ground motion estimates independent of the hybrid Green’s function method in Section 6. Section 7.4 and 7.5 demonstrated acceleration responses similar to those estimated in Section 6 were obtained using completely different rupture models and purely empirical Green’s function. The results of Sections 6 and 7 unequivocally demonstrate that unusually large > 1 s accelerations are likely to occur at Jackson Lake Dam in response to large earthquake on the northern Teton fault segment and that such amplitudes are likely to exceed the largest > 1 s accelerations recorded to date and durations may exceed the longest durations associated with $M \sim 7$ earthquakes. Expected

felt durations within the low-velocity basin are likely to extend to 1.5 to 3 minutes, durations normally only associated with sites relatively close to $M > 8$ subduction zone earthquakes. Ground motions from the 1979 M 6.5 Imperial Valley earthquake provide empirical precedent for the large acceleration responses estimated at Jackson Lake Dam. However, the low-velocity basin and fault configuration at Jackson Lake Dam are likely to produce more extreme long-period acceleration than observed in Imperial Valley based on first-principles analyses of wave trapping (Figure 7-86).

The production of shear-waves at the basin edges, as inferred in the analyses in Sections 4 and 5, in addition to basin-edge surface waves, significantly contributes to the broadband ground motion hazard at the dam. The findings in Sections 4 and 6 are similar to Spudich and Iada (1993). They showed that shear-waves are produced at basin-edges of Coachella Valley, California, low-velocity basin and become strong secondary arrivals in the basin at a site 8 km from the basin edge. Similarly, Frankel et al. (1991) found that shear arrivals persisted for 8 s after the initial shear-wave arrival in the Santa Clara Valley low-velocity basin. The combination of strong conversion of shear-waves and surface waves at the low-velocity basin edges and likely shear-wave and surface wave resonances in the low-velocity basin, as demonstrated by the EGF ground motions simulations, suggest that the very-broad-period large amplitude acceleration responses in Figures 7-83 and 7-84 are credible expectations at Jackson Lake Dam.

Using a reference station located outside the low-velocity basin in Mexico City, Kawase and Aki (1989) showed that the inclusion of a shallow soft basin within a much larger basin ~ 10 km long is required to explain the extraordinary durations of ground motions observed in Mexico City from the 1985 Michoacan earthquake. The long durations were a product of two distinctive phases, the first associated with the reverberations of incident body waves, and the second phases consisting of surface waves. However, at Jackson Lake Dam the JLDW rock site inside the large-scale low-velocity basin exhibit durations only modestly less than durations at the JLDW soil site within the shallow very-low-velocity basin. Thus, there must be some fundamental differences between the physical properties of the large-scale low-velocity basins at Jackson Lake and Mexico City. More importantly, there appears to be a parasitic interaction of nearly-identical-

period resonant responses between the soil basin containing the embankment portion of the dam and the large-scale low-velocity basin for periods of 1-2 s.

The Jackson Lake low-velocity basin appears to have more abrupt basin-edges (steeper dips) than Mexico City and stronger impedance contrasts, which appears to more effectively trap energy than the large-scale basin beneath Mexico City. Thus, unlike the case found by Kawase and Aki (1989) in Mexico City, where very long-durations of > 80 s were limited to sites located in low-velocity lake sediments embedded in the larger low-velocity basin, it appears that even sites located on relatively high-velocity compacted till (~ 1 km/s shear-wave velocity) in the Jackson Lake low-velocity basin are likely to experience durations exceeding 80 s. The effect of the very-low-velocity basin containing the embankment section of Jackson Lake Dam is to strongly amplify accelerations for periods > 1 s, increase dynamic strains by decreasing coherence with increasing periods, and to prolong strong motion durations to several minutes. Since strong nonlinear damping of accelerations is generally limited to periods < 1 s (Archuleta, 1998; Archuleta et al., 2000; Bonilla, 2000), strong amplification of > 1 s period accelerations by the very-low-velocity shallow sedimentary basin beneath the embankment portion of Jackson Lake Dam appears likely for $M \sim 7$ earthquakes on the Teton fault. Phase velocities of basin-edge shear-waves and surface waves within the embankment portion of the dam are likely to be much lower than assumed in Chen and Harichandran (2001) which would lead to larger embankment stresses and foundation associated with three-dimensional variations of dynamic strains than calculated by Chen and Harichandran (2001). In particular, limited coherence calculations suggest that along-axis differential displacements between the concrete and embankment sections of > 50 cm are likely to persist for 10-20 s and that differential displacements > 20 cm may persist for > 60 s.

The broadband empirical Green's function ground motions suggest that the rock ground motions in Section 6 underestimate acceleration responses for periods ranging from 0.8-2 s on the horizontal components, overestimate vertical responses for periods > 2 s, and underestimate the total duration of strong ground shaking. The local and regional broadband EGF's identified a serious ground motion characteristic that was not revealed in the analyses in Section 6. For seismic energy incident into the low-velocity basin from azimuths north of the dam, the fundamental resonant periods are virtually identical for the large-scale low-velocity basin and the

very-low-velocity soil basin containing the embankment portion of the dam. Consequently, the long-duration resonances continuously re-energize the soil resonances for several minutes at periods > 1 s. Since accelerations for periods > 1 s are likely to be amplified by nonlinear dynamic modulus degradation of soils (Archuleta et al., 2000; Bonilla, 2000) the embankment may be subjected to several minutes of strong ground shaking. It is not possible to credibly quantify expected ground motion amplitudes or durations using the regional larger magnitude earthquakes because it was not possible to install the broadband reference seismographic stations outside the low-velocity basin necessary to identify and account for the relative proportion and amplitudes of body and surface waves incident into the low velocity basin. Consequently, considerable uncertainties remain about the expected duration and intensity of ground-shaking at Jackson Lake Dam.

Appropriate specification of soil input motions for the embankment portion of the dam is a difficult issue. The investigations in Section 5 show that 1D vertically-incident propagators will not adequately represent soil responses, so use of rock site JLDW motions as input to nonlinear calculations is inappropriate. Probably the best way to specify input motions for dynamic analyses of the embankment section of the dam is to limit engineering foundation models to a maximum depth of 30 m with no significant impedance contrasts within the foundation material, and use the JLD3 motions scaled by 0.5-0.6 as input at 30 m depth in the nonlinear engineering model. This is necessary because no 2D or even 3D FEM model of the foundation will include the 3D reverberation amplitude and duration responses using the JLDW motions as inputs. The JLD3 synthetic motions produced using the **M** 5.2 Idaho earthquake EGF's provide one reasonable ground motion scenario (Figures 7-53, 7-55, 7-57). However, it is imperative to also use a ground motion scenario that includes the double resonance responses produced by energy arriving from north of the dam. The JLD3 synthetic motions from the **M** 4.6 Yellowstone EGF's are likely corrupted by significant whole-path surface wave responses and without an broadband recordings outside the basin there is no quantitative basis to adjust the synthetic motions. The **M** 3.2 20 Nov. 2002 earthquake is close enough to the Teton fault that there are surface waves are appropriately scaled. Unfortunately station JLD3 was no longer operating when this earthquake was recorded at JLDW. Consequently, there are no empirical soil records available to represent the duration of expected ground shaking and parasitic double basin 1-2 s amplified acceleration responses along

the embankment section of Jackson Lake Dam for seismic energy incident from the north. The regional earthquake EGF's ground motion results suggest that JLD3 responses are starting to approach durations of $M \sim 8-9$ subduction zone earthquakes.

In principal it would be possible to calculate coherence between rock sites JLDW and JLD2, and soil sites JLD3 and JLD5. However, in practice the stations are either very close together (< 30 m) and straddle the dam, or are located more than 200 m apart. Instead of calculating coherence, the differential displacements between rock site JLD2 located near the northern end of the concrete section of the dam and soil site JLD3 using the $M 5.2$ Idaho, EGF's are shown in Figure 7-87. These difference displacements provide a rough idea of the minimum expected differential movements between the concrete section and the embankment section located about 200 m north of site JLD2 and the duration of differential movements. Positive differential displacements for the north horizontal correspond to along-axis extension. Maximum extensional along-axis differential displacements exceed 50 cm (Figure 7-87) and extensional along-axis differential displacements exceeding 20 cm persist for at least 60 s.

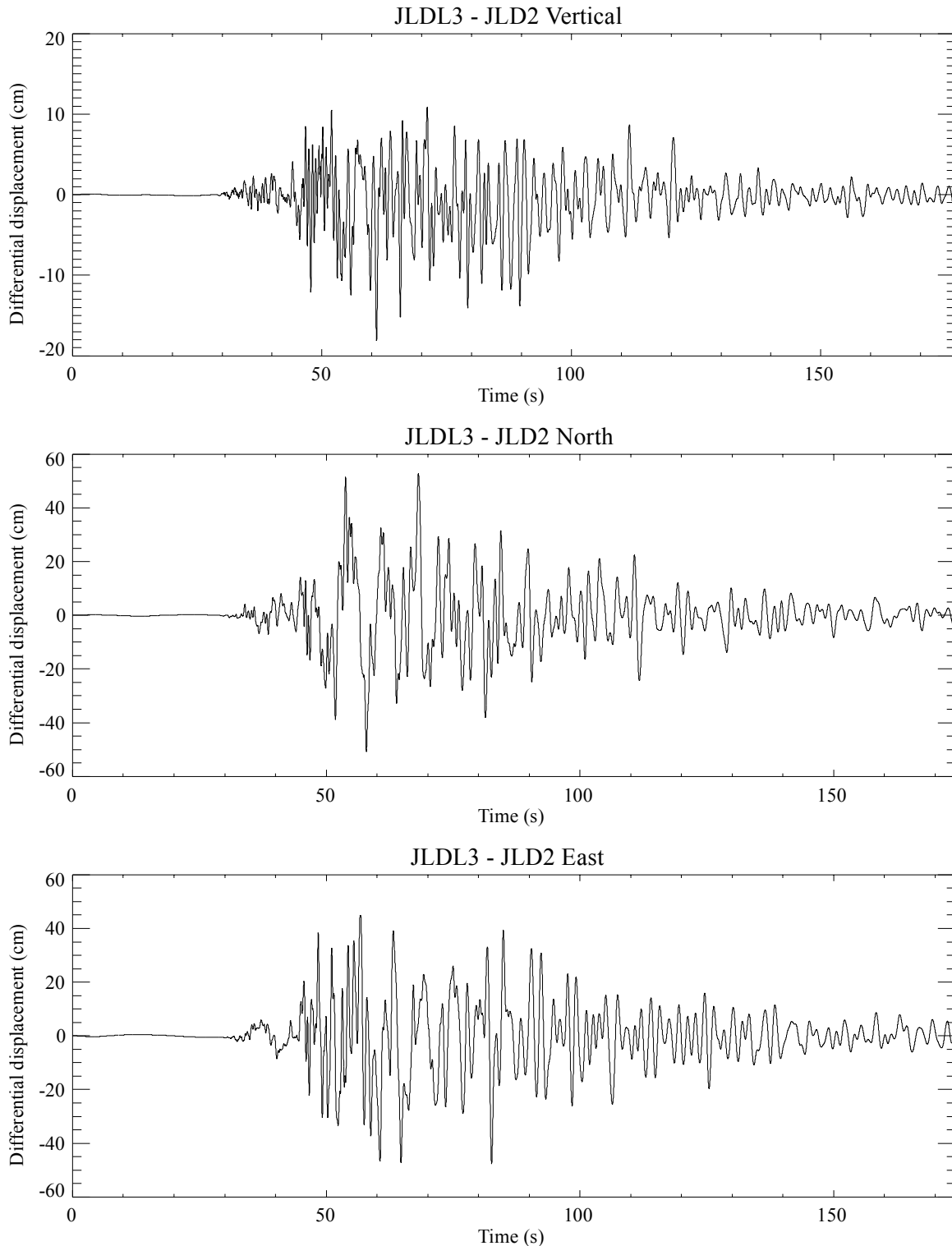


Figure 7-87: Differential displacements between sites JLD3 and JLD2 for a **M** 7.1 northern Teton fault segment earthquake. The **M** 5.2 Idaho, EGF's were used to synthesize ground motions at each site. The EGF's implicitly contain the propagation delays for the incident wavefield for azimuths near $\sim 210^\circ$. A much wider variety of incident azimuths occur during an actual large earthquakes on the Teton fault, so this scenario likely represents lower bounds on peak differential displacement.

